# Superconductivity and electronic structure of $KFe_2As_2$, $RbFe_2As_2$, and $CsFe_2As_2$ probed by thermal expansion and magnetostriction at very low temperatures

Zur Erlangung des akademischen Grades eines

DOKTORS DER NATURWISSENSCHAFTEN

von der Fakultät für Physik am

Karlsruher Institut für Technologie (KIT)

genehmigte

DISSERTATION

von

Dipl.-Phys. Felix Eilers

aus Braunschweig

Tag der mündlichen Prüfung: 4. Juli 2014

Referent: Prof. Dr. Hilbert von Löhneysen
Korreferent: Prof. Dr. Jörg Schmalian

# Contents

# 1 Introduction

Superconductivity is one of the striking emergent phenomena in condensed matter physics. Under favorable circumstances fermionic quasiparticles pair up and condense into a state with macroscopic phase coherence and a gapped quasiparticle excitation spectrum, displaying perfect diamagnetism and zero electrical resistance. The properties of one class of superconductors can be understood in terms of electron-phonon coupling as the pairing glue and an order parameter with the highest possible symmetry compatible with the symmetry of the crystal structure. This class of superconductors is called conventional, while all superconductors with a different or unknown pairing mechanism or symmetry of the order parameter lower than that of the crystal structure are classified as unconventional. Apart from natural curiosity, research on superconductors is ultimately driven by the desire to discover materials with ever higher transition temperatures, larger critical magnetic fields, and larger critical currents for the use in, for example, high-field magnets or high-current power lines. From the beginning, in 1911, this research was propelled forward by a number of serendipitous discoveries of superconductivity in new or known materials [1]. An iron-based superconductor, whose transition temperature drew attention, was first discovered in 2008 [2]. The transition temperatures and the multiband character, with all its ramifications for superconductivity and the normal state, spur the interest in iron-based superconductors [3–7].

The classification of iron-based superconductors distinguishes families based on the structural elements that separate the FeAs (or FeSe) layers that are common to all of its members. Going from simpler to more complex structures, selected parent compounds and their families are FeSe ('11'), LiFeAs ('111'), LaFeAsO ('1111'), and $BaFe_2As_2$ ('122').

Iron-based superconductors of the 122-family constitute a large number of materials for the study and tuning of unconventional superconductivity. The stoichiometric compounds $AFe_2As_2$, where $A$ can be Ca, Sr, Ba, K, Rb, Cs, or Eu, are either superconductors (K, Rb, Cs) or can be tuned to superconductivity by pressure or by substitution of $A$, Fe, or As by other elements. While the application of pressure tunes essentially the bandwidth of quasiparticles, the effects of substitution are more complex. Apart from a possible change of bandwidth due to chemical pressure, substitution may change the filling of bands and the amount of scattering. Therefore, effects of chemical pressure, doping, and disorder can be difficult to disentangle. An advantage of the stoichiometric superconductors $KFe_2As_2$, $RbFe_2As_2$, and $CsFe_2As_2$ is that no pressure or substitution is needed to study superconductivity. This group of compounds can, however, be viewed as a substitution series $AFe_2As_2$ with changing alkali atom $A$ =K, Rb, Cs. Then, substitution takes place not in the FeAs planes

but between them and no additional disorder is introduced.

In contrast to $BaFe_2As_2$, for example, the crystal structures of $KFe_2As_2$, $RbFe_2As_2$, and $CsFe_2As_2$ remain tetragonal down to lowest temperatures. Also, no magnetic order develops. While $BaFe_2As_2$, to stay with the same example, has both electron-like and hole-like bands, $KFe_2As_2$, $RbFe_2As_2$, and $CsFe_2As_2$ only have hole-like bands. Their superconducting tansition temperatures $T_c$ are relatively low ($T_c = 3.4, 2.5, 2.25\,\mathrm{K}$). Therefore, the study of superconductivity is not hampered by a large phonon background in physical quantities. In addition, the upper critical magnetic fields $\mu_0 H_{c2}$ (up to 5 T) are easily accessible without high-field facilities. All in all, hope is raised that in the stoichiometric superconductors $KFe_2As_2$, $RbFe_2As_2$, and $CsFe_2As_2$ unconventional superconductivity can be studied in its pure form, without disturbing (though interesting) effects of excess disorder or magnetic order. With a multitude of bands and gaps, a disputed symmetry of the order parameter, and an unknown pairing mechanism the puzzle is challenging enough.

In this work superconductivity and the electronic structure of the stoichiometric superconductors $KFe_2As_2$, $RbFe_2As_2$, and $CsFe_2As_2$ were probed by thermal expansion and magnetostriction measurements at very low temperatures. Single-crystal growth and characterization, with a special emphasis on structural properties, is described in chapter 2. The dilatometer and the experimental setup in a dilution refrigerator is explained in chapter 3.

It is known that $KFe_2As_2$ is a multiband superconductor with a paramagnetically limited upper critical field for the magnetic field in the *ab*-plane at low temperatures [8–10]. The question arises how superconducting properties develop in the series to $RbFe_2As_2$ and $CsFe_2As_2$. The measurements of the phase diagram, the uniaxial pressure dependence of critical tuning parameters, as well as statements about the limiting mechanism of the upper critical field presented in this work (chapter 4) will provide a solid foundation for theoretical attempts to describe multiband superconductivity in this series. In addition, the structural parameters of the iron-arsenic layers of $CsFe_2As_2$ are approximately equal to those of $Ba_{1-x}K_xFe_2As_2$, $x = 0.5$. This provides the opportunity to explore how the same structural elements give rise to superconductivity with transition temperatures of 2.25 K and 35 K, respectively.

$KFe_2As_2$, $RbFe_2As_2$, and $CsFe_2As_2$ exhibit relatively large electronic correlations compared to other iron-based superconductors. This is manifest in a cumulative measure of the density of states, the Sommerfeld coefficient of the specific heat, which increases in the series from approximately 100 to $180\,\mathrm{mJ\,mol^{-1}\,K^{-2}}$ [9, 11]. In order to improve the understanding of this effect, it is necessary to know the contribution of each of the five bands. Here, quantum oscillation studies can be useful as a bulk probe of the Fermi surface that yields effective quasiparticle masses on a per band basis. The Fermi surface of $KFe_2As_2$ and the effective masses of its bands have already been studied [12–14]. The question arises how the Fermi surfaces and the effective masses of each band of $RbFe_2As_2$ and $CsFe_2As_2$ develop. This work presents the first measurements of the Fermi surfaces of $RbFe_2As_2$ and $CsFe_2As_2$ and experimental data on effective masses of all bands (chapter 5). The origin of the electronic correlations and possible links to superconductivity are discussed.

# 2 Single crystals

## 2.1 Crystal growth parameters

The single crystals studied in this work were grown and characterized by the crystal growth team of the Institute for Solid State Physics (IFP) at the Karlsruhe Institute of Technology (KIT). Thomas Wolf grew single crystals of $KFe_2As_2$, $RbFe_2As_2$, and $CsFe_2As_2$ from arsenic-rich flux in alumina crucibles, as reported in Ref. [8] for $KFe_2As_2$. The crucibles were sealed in an iron tube filled with argon gas. All growth parameters are listed in table 2.1. One important parameter is the slow cooling rate. Also, most samples were annealed in situ, directly after the growth, to decrease defect concentrations. Figure 2.1 shows a photograph of the $RbFe_2As_2$ crystal.

## 2.2 Crystal structure

Peter Schweiss (IFP) studied the crystal structure of single crystals at room temperature with four-circle x-ray diffractometry using molybdenum radiation. Structural refinement confirmed the space group to be $I4/mmm$ and the composition to be stoichiometric within the error of the experiment (1-2 %). The conventional bodycentered-tetragonal unit cell contains two formula units and two iron-arsenic layers. The iron-arsenic layers consist of a square planar arrangement of iron atoms surrounded by arsenic atoms in a tetrahedron configuration (see figure 2.3). Figure 2.2 compares the structural parameters of $KFe_2As_2$, $RbFe_2As_2$, and $CsFe_2As_2$, called

**Table 2.1:** A list of the single crystals and their growth parameters. Alumina crucibles were sealed in iron-tubes filled with argon gas. $T_1$ is the maximum temperature, $T_2$ the minimum temperature, and $r_T$ the cooling rate. In situ annealing at lower temperatures directly after the growth was applied for most samples.

| Sample, batch no. | flux<br>$A$:Fe:As | $T_1$, $T_2$, $r_T$<br>°C, °C, °C/h | annealing<br>in situ |
|---|---|---|---|
| $KFe_2As_2$ (S1), 1119 | 0.22:0.25:0.53 | 1000, 854, 0.30 | 3 °C/h to RT |
| $KFe_2As_2$ (S2), 1049 | 0.30:0.10:0.60 | 980, 808, 0.49 | none |
| $RbFe_2As_2$, 1180 | 0.40:0.05:0.55 | 980, 691, 0.76 | 1 d at 450, 400, 350 °C |
| $CsFe_2As_2$ (S1), 1239 | 0.40:0.05:0.55 | 950, 799, 0.25 | 1 d at 450, 400, 350 °C |
| $CsFe_2As_2$ (S2), 1253 | 0.40:0.05:0.55 | 950, 797, 0.20 | 1 d at 450, 400, 350 °C |

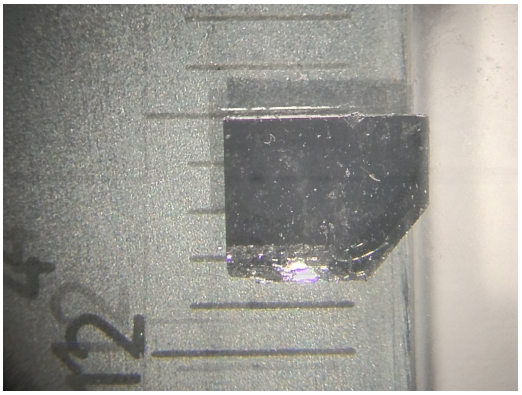

**Figure 2.1:** A photograph of the $RbFe_2As_2$ crystal. Its shorter length along the crystal $a$-direction is approximately 3.5 mm, its thickness is approximately 0.7 mm.

$A122$-series, with the parameters of $CaFe_2As_2$, $SrFe_2As_2$, and $BaFe_2As_2$, called $AE122$-series, and with $Ba_{1-x}K_xFe_2As_2$. The large $A$-As or $AE$-As bond length and the phenomenological linear dependence of $c$, $a$, and $z$ on the eight-fold coordinated ion radius $R_{I8}$ of the alkali ($A$) or alkaline earth ($AE$) atom in both the $A122$- and the $AE122$-series justify the choice of this quantity as abscissa. Values of $R_{I8}$ were taken from Ref. [15]. The unit cell volume $V$ and the $c/a$-ratio increase linearly with $R_{I8}$ in both series. In the $AE122$-series the tetrahedron of arsenic atoms surrounding the iron atoms is compressed along the $c$-direction, and in the $A122$-series it is elongated along $c$. The tetrahedron angle $\alpha$ in the $ac$-plane and the other tetrahedron angle $\beta$ (see figure 2.3) follow similar trends in both series, with $\alpha$ increasing with $R_{I8}$ and $\beta$ decreasing with $R_{I8}$. The ideal tetrahedron angle $\alpha = \beta = 109.47^\circ$ is realized in $Ba_{1-x}K_xFe_2As_2$ for $x \approx 0.4$. The height $h_{As}$ of the arsenic atoms above the iron plane decreases very little in the $AE122$-series, while the distance $d_{Fe-As}$ between the iron atoms and the arsenic atoms increases significantly. The $A122$-series exhibits the opposite behavior: $h_{As}$ decreases significantly, while $d_{Fe-As}$ changes very little. The distance between iron atoms, on the other hand, is given by $d_{Fe-Fe} = a/\sqrt{2}$ and increases linearly in both series. The ratio $h_{As}/a$ measures the anisotropy of the iron-arsenic planes, in contrast to $c/a$, which measures the anisotropy of the whole unit cell. While it is larger for the $A122$-series, $h_{As}/a$ decreases in both series. To aid in the visualization of these structural parameters, figure 2.3 gives an artist's impression of the conventional tetragonal unit cells of $KFe_2As_2$, $RbFe_2As_2$, and $CsFe_2As_2$.

Johrendt and Pöttgen [16] argued that, based on the bond lengths in $BaFe_2As_2$, the Ba-As bonds are rather ionic, the polar but covalent Fe-As bonds are the strongest bonds, and direct Fe-Fe bonds are present. Since the iron atoms are nominally in a $3d^6$ configuration in $BaFe_2As_2$, $d$-shells are more than half-filled and Fe-Fe antibonding states are at least partially occupied. Any change in the $a$-parameter changes the overlap of antibonding orbitals involved in the Fe-Fe bond. In the series

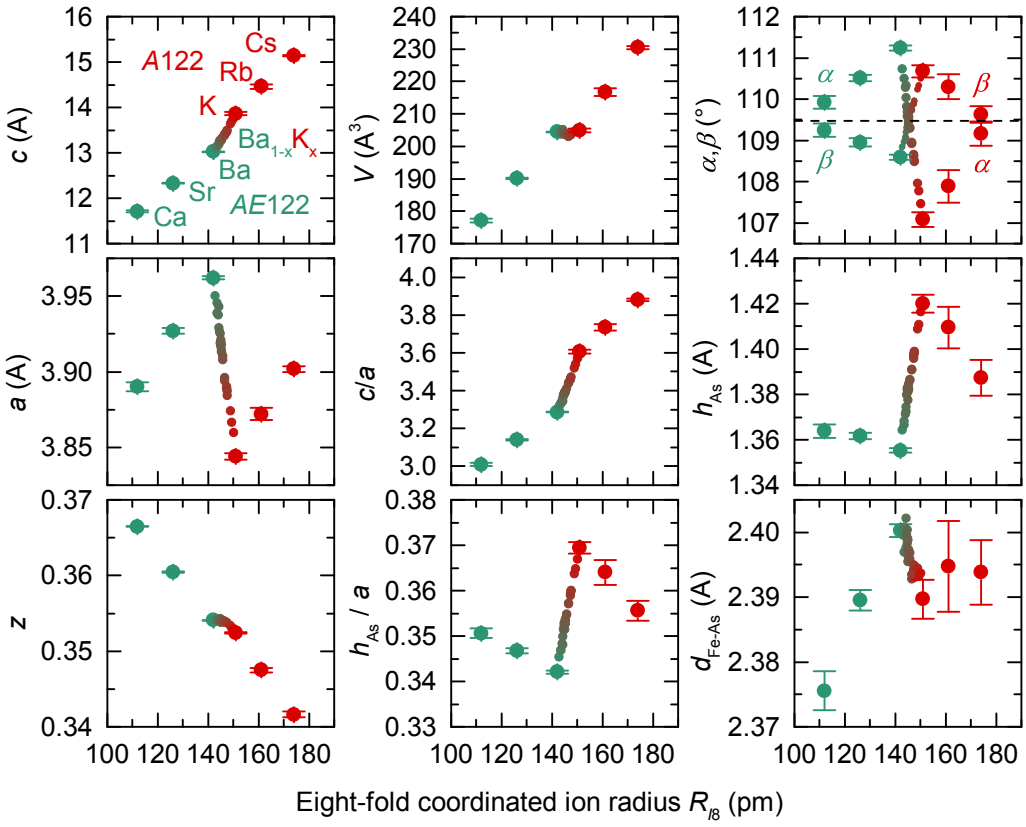


**Figure 2.2:** The structural parameters of $CaFe_2As_2$, $SrFe_2As_2$, $BaFe_2As_2$ (green), $Ba_{1-x}K_xFe_2As_2$ (green to red), $KFe_2As_2$, $RbFe_2As_2$, and $CsFe_2As_2$ (red) measured by four-circle x-ray diffraction on single crystals at room temperature, plotted against the eight-fold coordinated ion radius $R_{I8}$ of the alkali ($A$) or alkaline earth ($AE$) atom. Values of $R_{I8}$ were taken from Ref. [15]. $\alpha$ is the tetrahedron angle in the $ac$-plane and $\beta$ is the other tetrahedron angle (see figure 2.3). The ideal tetrahedron angle 109.47 ° is marked with a dashed line. $h_{As}$ is the height of the arsenic atoms above the iron plane. $h_{As}/a$ gives a measure of the anisotropy of the iron-arsenic layers. $d_{Fe-As}$ is the iron-arsenic bond length. The iron-iron distance is $d_{Fe-Fe} = a/\sqrt{2}$.

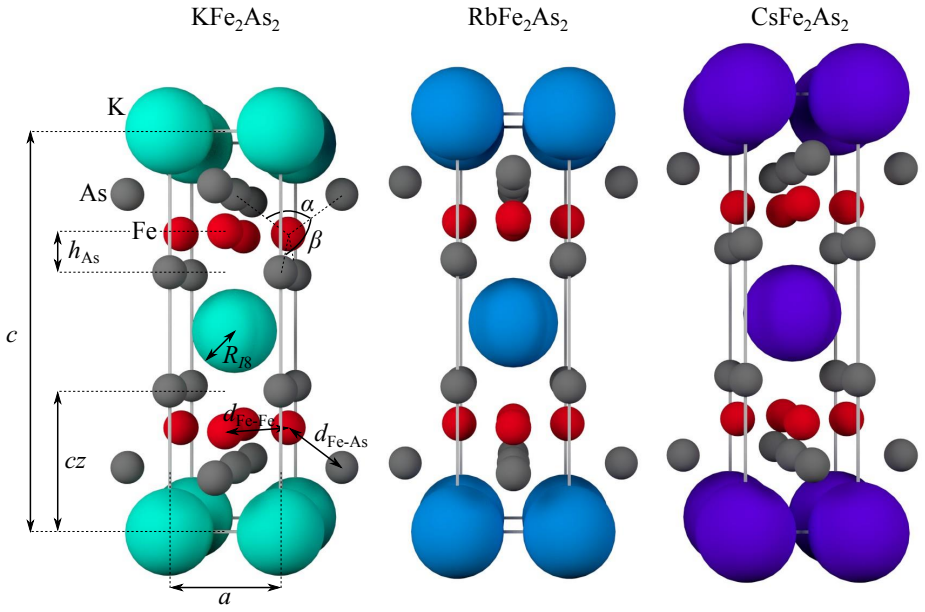


**Figure 2.3:** Sketches of the conventional tetragonal unit cells of $KFe_2As_2$, $RbFe_2As_2$, and $CsFe_2As_2$. The relative sizes of the unit cells and the atomic positions are to scale.

$Ba_{1-x}K_xFe_2As_2$ the parameters $a$ and $c$, as well as the tetrahedron angles change linearly with $x$ [17]. While $c$ increases, $a$ and $z$ decrease, leading to an elongation of the tetrahedron in the $z$-direction. The ideal tetrahedron angle is crossed at $x = 0.4$, where also the optimal superconducting transition temperature $T_c \approx 38\,\mathrm{K}$ is reached.

When hydrostatic pressure is applied to $BaFe_2As_2$ [18], both $a$ and $c$ decrease, but $z$ increases. This leads to a similar elongation of the tetrahedron as in the $Ba_{1-x}K_xFe_2As_2$ series [18]. The ideal tetrahedron angle and the optimal $T_c$ are reached for a pressure of approximately 4 GPa. Thus, substitution of Ba by K and hydrostatic pressure have a very similar and pronounced effect on the iron-arsenic planes and on superconductivity.

When K is replaced by Rb and Cs in the $A122$-series, the iron-arsenic planes change relatively little, as in the $AE122$-series. The most noticable change is in the height of the arsenic atoms above the iron plane. Remarkably, the structure of the iron-arsenic layers of $CsFe_2As_2$ is very similar to that of $Ba_{0.5}K_{0.5}Fe_2As_2$.

## 2.3 Magnetization

The volume magnetization divided by the magnetic field, $M_V/H$, of $KFe_2As_2$ as a function of temperature was measured and discussed by Hardy *et al.* [9]. It increases with decreasing temperature, exhibits a broad maximum around 100 K and

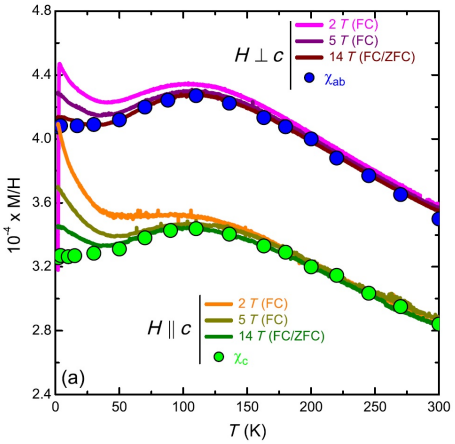


**Figure 2.4:** Volume magnetization divided by the magnetic field, $M_V/H$, of $KFe_2As_2$ measured as a function of temperature $T$. Taken from Ref. [9]. The upturn at low temperatures is caused by magnetic impurities. The broad maximum around 100 K is interpreted as a quasiparticle coherence scale [9].

an upturn at low temperatures (see figure 2.4). The position of the broad maximum is interpreted [9] as a quasiparticle coherence scale, below which heavy quasiparticles exist in a Fermi liquid and above which quasiparticles lose coherence. At lower magnetic fields the broad maximum is better visible for $H \parallel ab$ than for $H \parallel c$. The upturn at low temperatures is a sign of magnetic impurities [9]. $M_V/H$ of $RbFe_2As_2$ and $CsFe_2As_2$, albeit recorded at lower magnetic fields than the curves in figure 2.4, are similar to that of $KFe_2As_2$ (see figure 2.5). The curves also display an upturn at low temperatures, so the samples also contain magnetic impurities, either embedded in the bulk, or on the surface, or both. A broad maximum is visible for $RbFe_2As_2$ in $H \parallel ab$ but not in $H \parallel c$, where it is possibly hidden below the upturn at low temperatures. For $CsFe_2As_2$ no broad maximum is visible in the measurements shown. Possibly, the broad maximum is shifted to lower temperatures in the series $KFe_2As_2$ to $RbFe_2As_2$ to $CsFe_2As_2$, being hardly visible in magnetization measurements in low fields. This would be compatible with thermal expansion data, which display a broad maximum at roughly 100 K, 50 K, and 40 K, respectively [19].

The right-hand panel of figure 2.5 shows the superconducting transition as observed by magnetization measurements performed using a "magnetic properties measurement system" with SQUID read-out by Quantum Design. The onset of the Meissner effect is seen as a drop in the field-cooled $M_V/H$.

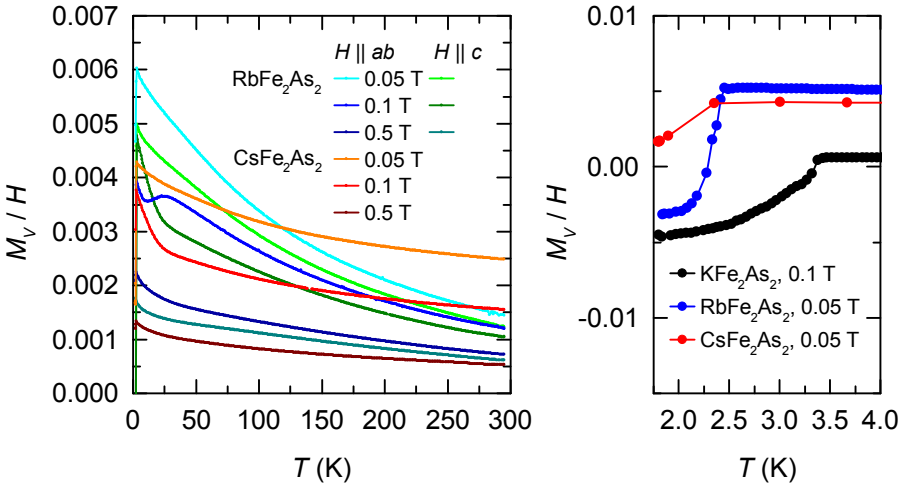


**Figure 2.5:** Left: Volume magnetization divided by the magnetic field, $M_V/H$, of $RbFe_2As_2$ ($H \parallel ab$ and $H \parallel c$) and $CsFe_2As_2$ ($H \parallel a$). The upturn at low temperatures reveals magnetic impurities. Right: $M_V/H$ (field-cooled) of $KFe_2As_2$, $RbFe_2As_2$, and $CsFe_2As_2$, showing the superconducting transition.

# 3 Capacitance Dilatometry

## 3.1 Capacitance dilatometer

A very sensitive method is required to measure changes in length of millimeter-sized crystals at low temperatures and in magnetic fields. Capacitance dilatometry offers the required sensitivity to resolve effects of the order of magnitude of $10^{-6}$ to $10^{-10}$ in the relative change in length $\Delta L/L$. The working principle of this method is as follows (see figure 3.1): A sample of length $L$, for example a single crystal, is clamped between a ground plate and one of two parallel capacitor plates by the force exerted by two parallel springs. When the length of the sample changes, the springs transmit this movement to the first capacitor plate which, in turn, moves relative to the second capacitor plate. This changes the distance $d$ of the capacitor plates and accordingly their capacitance $C$. The change in capacitance is measured and converted into the change in length of the sample $\Delta L$:

$$\Delta L = -\Delta d = -\epsilon_0 \epsilon_r A \cdot \Delta \frac{1}{C}, \tag{3.1}$$

where $\epsilon_0 \approx 8.854188 \cdot 10^{-12}\,\mathrm{AsV^{-1}}$ is the electric constant, $\epsilon_r$ is the relative electric permittivity, and $A$ is the area of the capacitor plates. For the measurements presented in this work $\epsilon_r = 1$ and $A = 0.92\,\mathrm{cm}^2$. To obtain the approximate relative change in length $\Delta L/L$, the length of the sample at room temperature $L_0$ was measured with a digital caliper with micrometer resolution.

The resolution of the relative change in length $\Delta L/L_0$ can be estimated to be

$$\Delta\left(\frac{\Delta L}{L_0}\right) = \frac{\epsilon_0 \epsilon_r A}{L_0} \cdot \frac{1}{C^2} \Delta(C), \tag{3.2}$$

where $\Delta(C)$ is the resolution of the capacitance measurement. It is desirable to measure at a small absolute distance of the capacitor plates, as this leads to a large absolute capacitance and to a large change in capacitance for a small change in sample length, which improves the resolution. For the measurements presented in this work $\Delta(C) = 10^{-6}$ to $10^{-5}\,\mathrm{pF}$ and the resolution in the relative change in length is in the range $10^{-9}$ to $10^{-10}$, or 0.1 to 1 pm for a sample that is one millimeter long.

The capacitance dilatometer used in this work was already described by Drobnik [20] and by Zaum [21]. It is made of Cu:Be alloy. At temperatures below 4 K its thermal expansion is so small that no correction of the data for thermal expansion of the dilatometer is necessary.

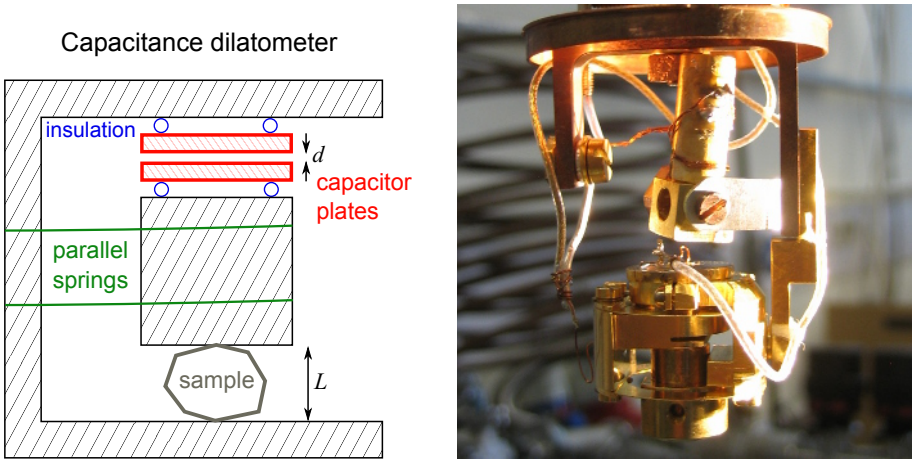


**Figure 3.1:** Left: Schematic of a parallel-plate capacitance dilatometer. A change in sample length $L$ is transmitted to the movement of one capacitor plate via two parallel springs. The change in the distance $d$ of the capacitor plates is measured as a change in capacitance $C \propto 1/d$. Right: Photograph of the dilatometer used in this work.

## 3.2 Experimental setup in a dilution refrigerator

Measurements were conducted in a dilution refrigerator, model MX400 by Oxford Instruments, equipped with a 14 T magnet. The dilatometer was thermally coupled to the mixing chamber by plates made of a silver alloy. The temperature at the sample could be ramped up from 20 mK to 3 K without evaporating the mixture in the mixing chamber. Measurements above 3 K were conducted removing part of the mixture and using only the 1 K-pot for cooling. A strain gauge was used as heating element and a ruthenium oxide chip as thermometer.

Thermal coupling to the room-temperature environment of the laboratory has to be avoided. Therefore a range of different cables are used at different temperature stages. At room temperature common copper wires transmit electrical signals between the refrigerator and the instruments for data acquisition and instrument control. The wires are twisted in pairs and well shielded to prevent the pick-up of electromagnetic noise. Outbreak boxes and filters directly on top of the cryostat prevent the intrusion of electromagnetic environment noise into the cold part. Between the room-temperature stage and the 4 K-stage Cu:Be wires with smaller thermal conductivity are used. Between the 4 K-stage and the mixing chamber of the refrigerator superconducting niobium titanium wires are used, because superconducting electrons do not transport heat. Between the mixing chamber and the dilatometer copper wires provide a good thermal connection of the capacitance plates and the thermometers to the bulk of the cold stage of the refrigerator. Coaxial cables were used for the capacitance measurement, with superconducting niobium cores between the 4 K-stage and the mixing chamber.

Capacitance was measured in a three-terminal setup with a capacitance bridge, model AH2550 by Andeen-Hagerling, using an excitation voltage of 15 V, an excitation frequency of 1 kHz, and an integration time of 9 s. The resistance of the ruthenium oxide thermometer was measured with an AC resistance bridge, model AC370 by Lake Shore Cryotronics. The effect of magnetoresistance was considered during the conversion of the resistance into a temperature value. Coefficients of a phenomenological description of the magnetoresistance proposed by Watanabe *et al.* [22] were extracted from calibration measurements by Zaum [21]. Spline interpolations of the resistance as a function of both temperature and magnetic field allowed the field-correction of all temperature values. The heating element was driven by a DC current source, model 2400 SourceMeter by Keithley Instruments, with a low-frequency pass attached to its output.

Thermal expansion and magnetostriction were measured in a continuous manner, ramping the temperature or the magnetic field continuously and taking measurements of the capacitance with a fixed averaging time of 9 s. The temperature rate depended exponentially on the temperature, so that more data points were taken at lower temperatures, where changes in length are usually smaller. The ramp rate of the magnetic field was constant, usually 0.1 T/min, or 0.02 T/min for measurements of higher-frequency quantum oscillations.

## 3.3 Thermal expansion and magnetostriction

Thermal expansion relates a second rank tensor, strain $\epsilon_{ij}$, to a scalar, temperature $T$. Since $\epsilon_{ij}$ is a symmetric tensor, also the thermal expansion tensor is symmetric.

$$\alpha_{ij} = \left(\frac{\partial \epsilon_{ij}}{\partial T}\right)_{p,H=0} \tag{3.3}$$

For uniaxial samples in zero magnetic field or with a magnetic field applied parallel to the axis

$$\alpha_{ij} = \begin{pmatrix} \alpha_{11} & 0 & 0 \\ 0 & \alpha_{11} & 0 \\ 0 & 0 & \alpha_{33} \end{pmatrix}. \tag{3.4}$$

Therefore, for the tetragonal crystals studied in this work, only two thermal expansion coefficients are relevant at zero magnetic field: $\alpha_a \equiv \alpha_{11}$ and $\alpha_c \equiv \alpha_{33}$. The volume thermal expansion coefficient is then $\alpha_V = 2\alpha_a + \alpha_c$. For magnetic fields $H_k$ or stress $\sigma_{kl}$ applied in arbitrary directions the number of coefficients rises. Magnetostriction is a third rank axial tensor, that means its coefficients change sign under reflections or inversions:

$$\lambda_{ijk} = \left(\frac{\partial \epsilon_{ij}}{\partial(\mu_0 H_k)}\right)_{T,p}. \tag{3.5}$$

In this work changes in length were measured along crystal $a$- and $c$-axes while applying the magnetic field either along the $a$-, $b$-, or $c$-direction. Thus five magnetostriction coefficients appear in this work: $\lambda_a^{H\|a} \equiv \lambda_{111}$, $\lambda_a^{H\|b} \equiv \lambda_{112}$, $\lambda_a^{H\|c} \equiv \lambda_{113}$, $\lambda_c^{H\|a} \equiv \lambda_{331}$, and $\lambda_c^{H\|c} \equiv \lambda_{333}$.

Since the absolute length $L$ of the sample cannot be measured continuously, the temperature derivative of the linear strain $\epsilon$ was approximated by the temperature derivative of the dilation $(L-L_0)/L_0$ with respect to the length at room temperature $L_0 = L_{RT}$.

$$\epsilon = \int_{L_0}^{L} \frac{\mathrm{d}L'}{L'} = \ln\left(\frac{L}{L_0}\right) = \ln\left(1 + \frac{L - L_0}{L_0}\right) \tag{3.6}$$

$$\frac{\partial \epsilon}{\partial T} = \frac{1}{L}\frac{\partial L}{\partial T} \approx \frac{1}{L_0}\frac{\partial L}{\partial T} + O\left(\frac{\partial}{\partial T}\left(\frac{L - L_0}{L_0}\right)^2\right) \tag{3.7}$$

This introduces only a very small error, because the change in length is very small compared to the absolute length (by a factor of $10^{-8}$ to $10^{-6}$). The same approximation is made for the magnetic-field derivative.

The uniaxial stress exerted on the sample by clamping it in the dilatometer is so small, typically several bar, that it can be neglected. This is shown by the experimental fact that anomalies in $\alpha_a$ and $\alpha_c$ yield the same transition temperature $T_c$ despite different signs of the uniaxial stress-dependence of the transition temperature $\mathrm{d}T_c/\mathrm{d}\sigma_a$ and $\mathrm{d}T_c/\mathrm{d}\sigma_c$.

## 3.4 Uniaxial pressure dependence of entropy and magnetization

Thermal expansion and magnetostriction are related to other thermodynamic quantities by means of the total differential of the Gibbs free energy

$$\mathrm{d}G(T, p, \boldsymbol{H}) = -S\mathrm{d}T + V\mathrm{d}p - \sum_i M_i \mathrm{d}(\mu_0 H_i), \tag{3.8}$$

where $S$ is the entropy, $V$ the volume, and $\boldsymbol{M}$ the magnetic moment, or

$$\mathrm{d}G(T, \sigma_{ij}, H_k) = -S\mathrm{d}T - \int \mathrm{d}V \left(\sum_{i,j} \epsilon_{ij}\mathrm{d}\sigma_{ij}\right) - \sum_k M_k \mathrm{d}(\mu_0 H_k), \tag{3.9}$$

where stress $\sigma_{ij}$ replaces hydrostatic pressure $p$. Since $G$ is a thermodynamic potential, the order of partial differentiation of $G$ with respect to two of its variables can be interchanged arbitrarily. From this a set of equations, called Maxwell relations, follows that relate several thermodynamic quantities. Specifically, the Maxwell relations state the equivalence of thermal expansion and the pressure dependence of the

entropy, as well as the equivalence of magnetostriction and the pressure dependence of the magnetic moment:

$$\alpha_V = \frac{1}{V}\left(\frac{\partial V}{\partial T}\right)_{p,H} = -\frac{1}{V}\left(\frac{\partial S}{\partial p}\right)_{T,H}, \tag{3.10}$$

$$\lambda_V = \frac{1}{V}\left(\frac{\partial V}{\partial(\mu_0 H)}\right)_{T,p} = -\frac{1}{V}\left(\frac{\partial M}{\partial p}\right)_{T,H}. \tag{3.11}$$

In the corresponding expressions for $\alpha_i$ and $\lambda_i$, $i = a, c$ (or 1,3) for tetragonal systems the hydrostatic pressure can be replaced by the uniaxial pressure $p_i \equiv -\sigma_{ii}$.

$$\alpha_i = \frac{1}{L_i}\left(\frac{\partial L_i}{\partial T}\right)_{\sigma,H} = -\frac{1}{V}\left(\frac{\partial S}{\partial p_i}\right)_{T,H} \tag{3.12}$$

$$\lambda_i = \frac{1}{L_i}\left(\frac{\partial L_i}{\partial(\mu_0 H)}\right)_{T,\sigma} = -\frac{1}{V}\left(\frac{\partial M}{\partial p_i}\right)_{T,H} \tag{3.13}$$

One should not get confused by the fact that the pressure dependence of the entropy or the magnetic moment is given as a function of temperature or magnetic field at a constant pressure (zero in this work) and not as a function of pressure.

The temperature derivative of the thermal expansion coefficient, which is the curvature of the change in length as a function of temperature, is related to the pressure dependence of the specific heat $C$, because $\partial S/\partial T = C/T$.

$$\left(\frac{\partial \alpha_i}{\partial T}\right)_{p,H} = -\frac{1}{VT}\left(\frac{\partial C}{\partial p_i}\right)_{T,H} \overset{*}{=} -\frac{1}{V}\left(\frac{\partial \gamma}{\partial p_i}\right)_{T,H}, \tag{3.14}$$

where the last identity, marked with an asterisk, holds for a Fermi liquid at low temperatures, when $C = \gamma T$ with the Sommerfeld coefficient $\gamma$. The Sommerfeld coefficient, in turn, is proportional to the density of states.

The magnetic-field derivative of the magnetostriction coefficient, which is the curvature of the change in length as a function of magnetic field, is related to the pressure dependence of the magnetic susceptibility $\chi = \partial M/\partial(\mu_0 H)$.

$$\left(\frac{\partial \lambda_i}{\partial(\mu_0 H)}\right)_{T,p} = -\frac{1}{V}\left(\frac{\partial \chi}{\partial p_i}\right)_{T,H} \tag{3.15}$$

For a Fermi liquid at low temperatures, the magnetic susceptibility is proportional to the density of states and the $g$-factor of the quasiparticles.

## 3.5 Phase transitions

The equivalence of the thermal expansion coefficient $\alpha$ and the pressure dependence of the entropy (eqs. 3.10, 3.12) is the explanation for the appearance of anomalies

in $\alpha$ at phase transitions. All phase transitions, at which $\partial S/\partial p$ or its temperature derivative change as a function of $T$, can be observed in $\alpha$, not only structural phase transitions, but also magnetic and superconducting transitions. Similar, all phase transitions, at which $\partial M/\partial p$ or its field derivative change as a function of $\mu_0 H$, can be observed in the magnetostriction coefficient $\lambda$. At continuous phase transitions the Gibbs free energy $G$ is continuous as a function of the tuning parameter, and there is a slope change of the extensive quantities $S, V$, and $M$ and a step in $C$, $\chi$, $\alpha$, and $\lambda$. The uniaxial pressure dependence of the transition temperature and the critical magnetic field can be obtained from the Ehrenfest relations:

$$\frac{\mathrm{d}T_c}{\mathrm{d}p_i} = V_m T_c \frac{\Delta\alpha_i}{\Delta C_m}, \tag{3.16}$$

$$\frac{\mathrm{d}(\mu_0 H_c)}{\mathrm{d}p_i} = V_m \frac{\Delta\lambda_i}{\Delta\chi_m}, \tag{3.17}$$

where the index $m$ refers to molar quantities. At discontinuous phase transitions $G$ exhibits a discontinuity as a function of the tuning parameter, and there is a step in $S, V$, and $M$ and a sharp peak in $\alpha$ and $\lambda$. In this case, the uniaxial pressure dependence of the transition temperature and the critical magnetic field can be obtained from the Clausius-Clapeyron relations:

$$\frac{\mathrm{d}T_c}{\mathrm{d}p_i} = V_m \frac{\Delta L_i/L_i}{\Delta S_m}, \tag{3.18}$$

$$\frac{\mathrm{d}(\mu_0 H_c)}{\mathrm{d}p_i} = V_m \frac{\Delta L_i/L_i}{\Delta M_m}. \tag{3.19}$$

The uniaxial pressure dependence is evaluated at a fixed $p_i$ (approximately zero in this work), not as a function of uniaxial pressure.

# 4 Superconductivity in $KFe_2As_2$, $RbFe_2As_2$, and $CsFe_2As_2$

## 4.1 Superconductivity in iron-based materials

Superconductivity in iron-based materials [3–7, 23] is connected with their common structural element, iron-arsenic layers or, in the case of FeSe, iron-selenium layers. A generalized phase diagram, the dependence of the superconducting transition temperature $T_c$ on a tuning parameter like pressure $p$ or chemical substitution $x$, bears similarities to the generalized phase diagrams of the heavy-fermion superconductors and the cuprate superconductors. Superconductivity arises when a magnetic order is suppressed, and $T_c(p)$ or $T_c(x)$ often exhibit a broad maximum ("dome"). It seems to be established that electron-phonon coupling is too weak to explain the $T_c$ of iron-based superconductors on its own [24], although the electron-phonon interaction can be underestimated by calculations, especially in the presence of electronic correlations [25]. So-called spin-fluctuation exchange is a candidate for the pairing glue [7]. In many cases the symmetry of the superconducting gap [6, 7] is established to be symmetric with respect to rotation about the main symmetry axis and even with respect to inversion ($A_{1g}$ or "$s$-wave"). There are four to five bands that cross the Fermi energy and, accordingly, four to five gaps. Each gap can have a different magnitude that varies with direction. Nodes in the gap function are not a unique signature of a particular symmetry of the order parameter. So-called "accidental" nodes may appear for $s$-wave symmetry. There may be a nodeless "$d$-wave" state [7] ($B_{1g}$ or $B_{2g}$, antisymmetric with respect to rotations about the main symmetry axis). Small gaps may be mistaken for nodes in certain experiments. The symmetry may change with doping or with an external perturbation. In the $Ba_{1-x}K_xFe_2As_2$ series the symmetry above $x = 0.6$ is discussed controversially while it is established to be $s$-wave with a sign-change of the order parameter between electron- and hole-parts of the Fermi surface ($s^{+-}$) below $x = 0.6$ [26]. Thus, there is also no agreement on the symmetry of the gaps in $KFe_2As_2$, $RbFe_2As_2$, and $CsFe_2As_2$.

The multiband or multigap character of superconductivity in iron-based materials leaves its fingerprint in many physical quantities [27]. Apart from its phenomenological manifestations, intriguing aspects of multiband superconductivity are how the interactions between bands affect the pairing strength and the symmetry. No general answer can be given to these questions [6, 7], due to the large number of relevant material parameters. Different bands can have different density of states, impurity scattering rates, Fermi velocities, anisotropies, coupling strength, energy gaps, gap symmetries, etc [27]. Interband coupling gives rise to a single transition temperature

$T_c$ and a single upper critical field $H_{c2}$. The interaction of multiple bands can lead to surprisingly high $T_c$, as is the case for $MgB_2$ [27], where a description with two bands and their anisotropy explains a $T_c$ of 39 K even with electron-phonon interaction as the pairing glue. Considering this contribution in $MgB_2$, it should be studied how multiband properties affect the pairing in the iron-based superconductors, which display similar $T_c$ values, and how multiband interactions could be tuned to boost the transition temperatures further.

## 4.2 The critical temperature measured by thermal expansion

The observation of the Meissner effect is the hallmark sign of superconductivity. Not only is it the effect that defines a superconductor, it is also a bulk probe, compared to resistivity measurements, where a drop in resistivity can also be due to percolating paths of superconducting impurity phases or interfaces. Thermal expansion and magnetostriction are also bulk probes. That an anomaly in these quantities is connected with a superconducting transition, and not, for example, with a magnetic transition, must be verified by studying its dependence on a second tuning parameter or by other methods. The anomalies in thermal expansion and magnetostriction are usually sharp and provide a very good way to map out a phase diagram. As a bonus, they contain information on the uniaxial pressure dependence of the critical quantities $T_c$ and $H_{c2}$, respectively.

Thermal expansion $\Delta a/a_0$ and $\Delta c/c_0$ of $KFe_2As_2$ [10], $RbFe_2As_2$, and $CsFe_2As_2$ single crystals was measured at temperatures between 50 mK and 4 K and in magnetic fields $H \parallel a, b$ and $H \parallel c$ up to 14 T. While for $RbFe_2As_2$ both $\Delta a/a_0$ and $\Delta c/c_0$ could be measured on the same sample, for $KFe_2As_2$, and partly for $CsFe_2As_2$, $\Delta a/a_0$ and $\Delta c/c_0$ had to be measured on different samples, called samples S1 and S2 respectively, because S1 was too thin for measurements of $\Delta c/c_0$. This provides the opportunity to compare different samples of nominally the same compound made in different batches.

Figure 4.1 shows the relative changes in length $\Delta a/a_0$ and $\Delta c/c_0$ of $RbFe_2As_2$ at $H = 0$. The superconducting transition is observed as a change in slope of $\Delta L/L_0$ at $T_c = 2.5$ K, the signature of a continuous phase transition. Above the transition $\Delta L/L_0 \propto T^2$ and $a$ grows with temperature while $c$ shrinks. Below the superconducting transition $a$ shrinks with temperature while $c$ grows.

The derivatives of $\Delta a/a_0$ and $\Delta c/c_0$ yield $\alpha_a$ and $\alpha_c$, respectively, shown in figure 4.2 for $KFe_2As_2$, $RbFe_2As_2$, and $CsFe_2As_2$ for $H = 0$. The superconducting transition is observed as a step in $\alpha_i$. The position of the transition temperature $T_c$ is taken as the midpoint of this step. This criterion is consistent with the criterion usually applied for the extraction of the transition temperature from specific heat curves. There, the transition temperature is determined under the premise that equal amounts of entropy connected with the transition should lie below and above $T_c$. Compared to the specific heat, which is always positive, the thermal expansion

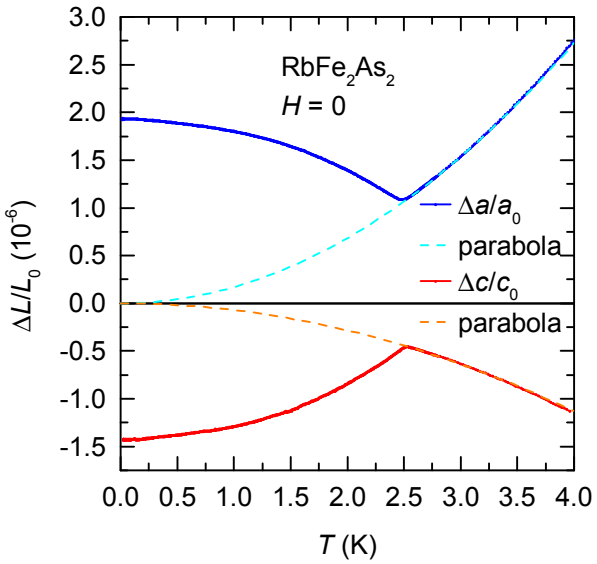


**Figure 4.1:** Relative changes in length $\Delta a/a_0$ and $\Delta c/c_0$ of $RbFe_2As_2$ at $H = 0$. The superconducting transition is observed as a change in slope of $\Delta L/L_0$. Above the transition $\Delta L/L_0 \propto T^2$ and $a$ grows with temperature while $c$ shrinks. Below the superconducting transition $a$ shrinks with increasing temperature while $c$ grows.

and its anomalies can have different signs. When there is a sign change of $\alpha_i$ in addition to a step, this is a particularly clear sign of a transition. Above the transition $\alpha_i$ has a linear dependence on the temperature. This is expected for a Fermi liquid at low temperatures with a linear dependence of the specific heat on temperature and a constant Grüneisen ratio $\alpha_V/C$. Below $T_c$ the thermal expansion coefficient tends towards zero, as expected for any material.

The right-hand part of figure 4.2 shows $\alpha_i/T$. A constant $\alpha_i/T$ above $T_c$ is expected for a Fermi liquid at low temperatures. In this case the constant value gives the uniaxial pressure dependence of the density of states at zero pressure (see eq. 3.14). Below $T_c$ the shape of the curves is relatively complicated, not directly tending to zero but exhibiting a hump at low temperatures. In general, this is a sign of either one gap on an anisotropic band, or multiple gaps on isotropic bands, or multiple gaps on anisotropic bands [27]. It is similar to the effects seen in the specific heat divided by temperature $C/T$ of $MgB_2$ (see figure 4.3) [28, 29], which is established to be a conventional multiband superconductor [27]. There is a fast rise of $C/T$ at very low temperatures, a shoulder at low temperatures, and a relatively small jump at the transition, all not compatible with expectations for the case of a single, isotropic band [27]. Similar characteristics were observed in $C/T$ of $KFe_2As_2$, which was described with four bands by Hardy *et al.* [30] (see the left-hand panel of figure 4.3). The necessity to invoke a multiband description in addition to anisotropy is evident from ARPES measurements [26].

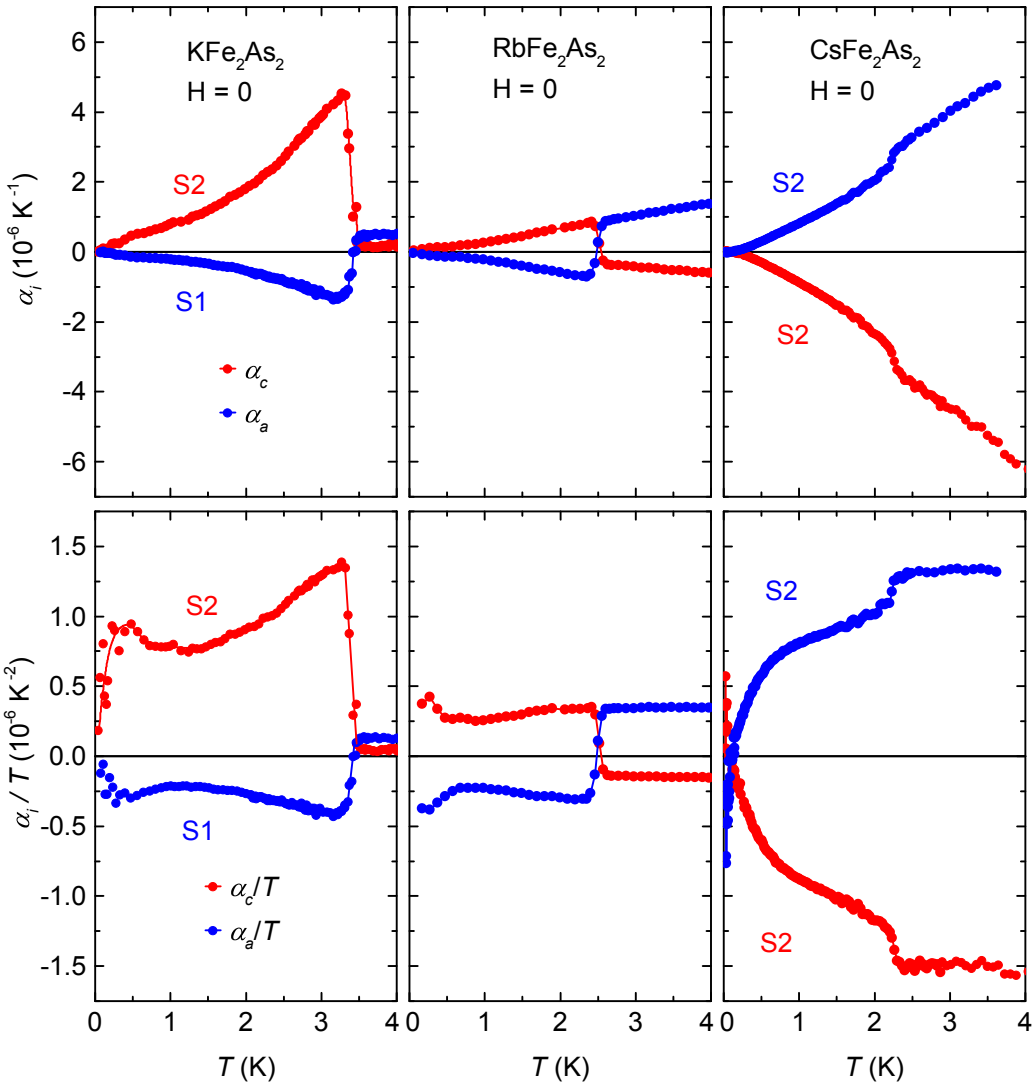


**Figure 4.2:** Top panels: The thermal expansion coefficients $\alpha_c$ and $\alpha_a$ of (from left to right) $KFe_2As_2$ (Samples S2 and S1), $RbFe_2As_2$, and $CsFe_2As_2$ (S2) at $H = 0$. The continuous superconducting transition is visible as a step in $\alpha_i$ at $T = 3.4, 2.5, 2.25\,\mathrm{K}$, respectively. Bottom panels: The complicated shape of the curve resulting from multiple superconducting gaps shows up more clearly in $\alpha_c/T$ and $\alpha_a/T$. The constant $\alpha_c/T$ and $\alpha_a/T$ above $T_c$ is expected for a Fermi liquid at low temperatures.

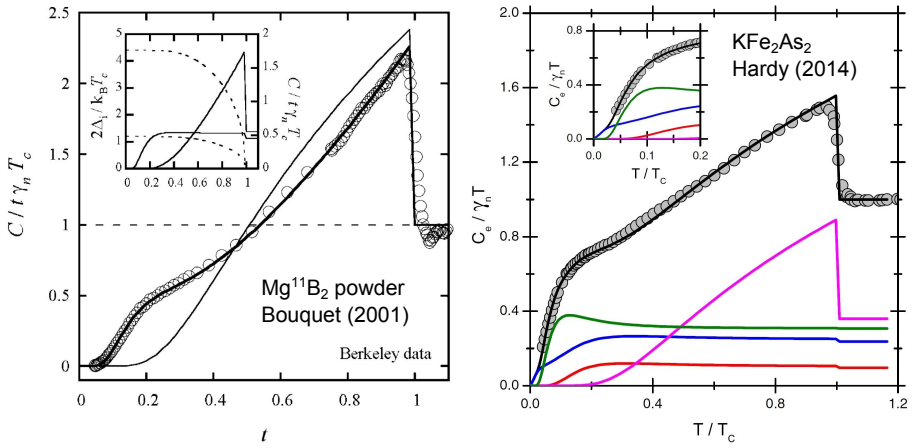


**Figure 4.3:** The electronic specific heat $C_e$ divided by $T$ and by the normal-state Sommerfeld coefficient $\gamma_n$ of $Mg^{11}B_2$ [28] (left) and $KFe_2As_2$ [30] (right), plotted against the normalized temperature $t = T/T_c$. In the case of $MgB_2$ the shape of the specific heat curve can be explained by two superconducting gaps [27]. Hardy *et al.* [30] use four gaps to describe the specific heat of $KFe_2As_2$.

The comparison of $\alpha_c$ for $KFe_2As_2$ with curves published by Burger *et al.* [8] and Bud'ko *et al.* [31] reveals a discrepancy in the absolute values (see figure 4.4). This difference is not due to the instruments used for the measurements but due to the shape of the samples and is a common problem with plate-like samples of iron-based superconductors [32]. A thin, plate-like sample clamped into a dilatometer along the $c$-axis will have contact with the dilatometer at several points. During thermal expansion measurements, not only the length along the $c$-axis changes, but also the length in the $ab$-plane. This leads to friction at the contact points and possibly to a bending of the sample or to a sideways movement of one of the capacitor plates, which may affect the signal.

Thermal expansion $\Delta a/a_0$ and $\Delta c/c_0$ was measured also in finite magnetic fields $H \parallel a, b$ and $H \parallel c$ up to 14 T. As an example, figure 4.5 shows $\alpha_a$ of $RbFe_2As_2$ in several magnetic fields $H \parallel c$ and figure 4.6 shows $\alpha_a$ in $H \parallel a$. The superconducting transition can be determined from $\alpha_i$ for several magnetic fields. As the phase transition line is crossed more and more tangentially at higher fields, the step in $\alpha_i$ becomes smoother. At these fields and temperatures magnetostriction curves cross the phase transition line more perpendicularly, resulting in sharper anomalies (see section 4.4).

## 4.3 Vortex matter

Magnetostriction $\Delta a/a_0$ and $\Delta c/c_0$ of $KFe_2As_2$ [10], $RbFe_2As_2$, and $CsFe_2As_2$ single crystals was measured in magnetic fields $H \parallel a$ and $H \parallel c$ up to 14 T, at temperatures between 50 mK and 4 K. As an example, figure 4.7 shows the relative changes in

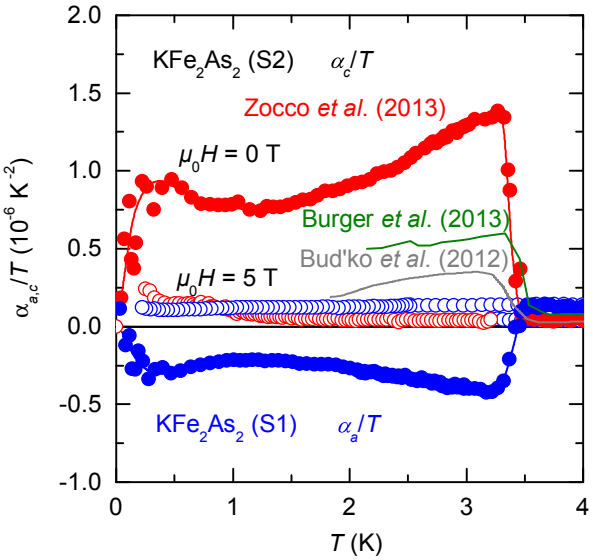


**Figure 4.4:** The thermal expansion coefficients $\alpha_c/T$ and $\alpha_a/T$ of $KFe_2As_2$ for $\mu_0 H = 0\,\mathrm{T}$ and $5\,\mathrm{T}$. The measurement of $\alpha_c/T$ for $\mu_0 H = 0\,\mathrm{T}$ by Zocco *et al.* [10] is compared to data by Burger *et al.* [8] and Bud'ko *et al.* [31]. The absolute values of $\alpha_c/T$ vary, a common problem with plate-like samples of iron-based superconductors [32].

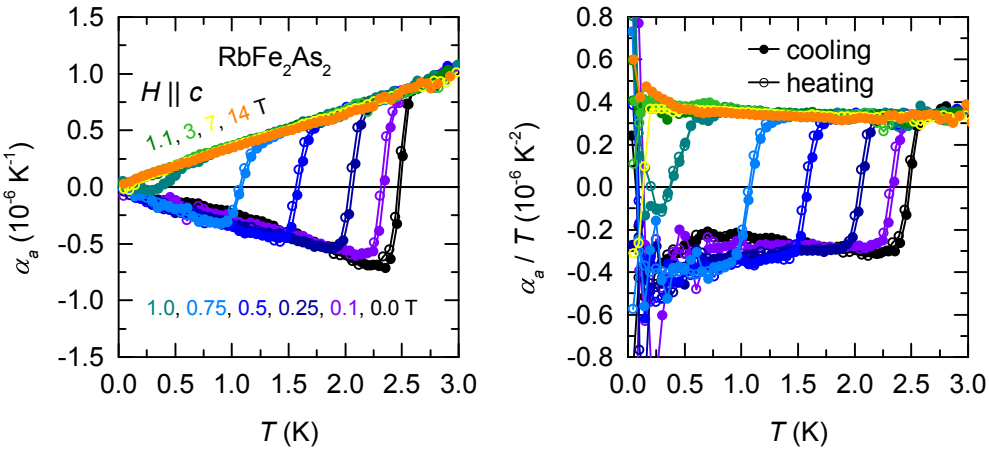


**Figure 4.5:** Left: The thermal expansion coefficient $\alpha_a$ of $RbFe_2As_2$ for $H \parallel c$, $H = 0$, 0.1, 0.25, 0.5, 0.75, 1, 1.1, 3, 7, 14 T, recorded during cooling (closed symbols) and heating (open symbols). Right: $\alpha_a/T$. The superconducting transition is seen as a step, which becomes smoother at higher fields, because the phase transition line is crossed more tangentially.

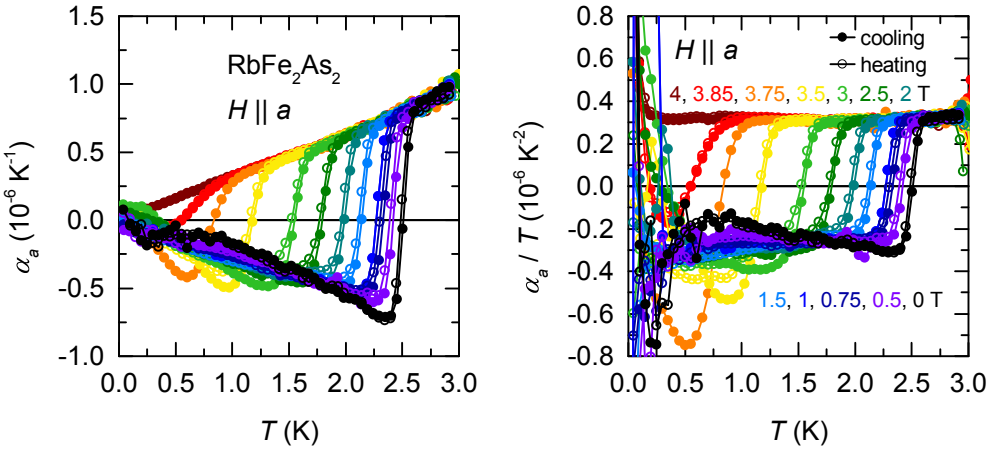


**Figure 4.6:** Left: The thermal expansion coefficient $\alpha_a$ of $RbFe_2As_2$ for $H \parallel a, H = 0, 0.5, 0.75, 1, 1.5, 2, 2.5, 3, 3.5, 3.75, 3.85, 4\,\mathrm{T}$, recorded during cooling (closed symbols) and heating (open symbols). Right: $\alpha_a/T$.

length $\Delta a/a_0$ and $\Delta c/c_0$ of $RbFe_2As_2$ at $T = 50\,\mathrm{mK}$ for different directions of the magnetic field. For $H \parallel c$ the superconducting transition is observed as a change in the slope, a sign of a continuous phase transition. For $H \parallel a$ the transition is observed as a step-like anomaly, a sign of a transition that is discontinuous. The magnetostriction curves in the superconducting state are different for increasing and decreasing magnetic field, the magnetostriction is irreversible. Also, it displays some peculiar anomalies.

The magnetostriction of superconductors results from several effects [33]. The first effect is the reversible part that is governed by thermodynamics. It is observed as a linear dependence of $\Delta L/L$ on the magnetic field or, equivalently, as a constant magnetostriction coefficient $\lambda_i$. A second effect is due to the demagnetizing field, which causes a deformation of the sample in order to minimize its energy. In type-II superconductors with an upper critical field $H_{c2} \gg H_{c1}$, the magnetic moment far above $H_{c1}$ is small due to the penetration of magnetic flux. Accordingly, demagnetization effects can usually be neglected. A third effect is due to supercurrents at the surface of the sample [33]. A fourth effect can be explained by the behavior of vortices, regions of normal-conducting material that penetrate a type-II superconductor in the mixed state, at magnetic fields between the lower critical field $H_{c1}$ and the upper critical field $H_{c2}$.

The interface between superconducting and normal-conducting regions can have a positive or a negative surface energy $\sigma_{sn}$ [34]. When $\sigma_{sn} > 0$ it costs energy to create interfaces, while for $\sigma_{sn} < 0$ it is favorable to create a certain amount of interfaces, because the loss in superconducting condensation energy $U_c$ can be compensated by the gain in $\sigma_{sn}$. The sign of $\sigma_{sn}$ is determined by the Ginzburg-Landau parameter $\kappa = \lambda_\mathrm{L}/\xi_\mathrm{GL}$. Here, $\lambda_\mathrm{L}$ is the London penetration depth, the length scale on which magnetic fields and shielding currents penetrate a superconductor. Disturbances of

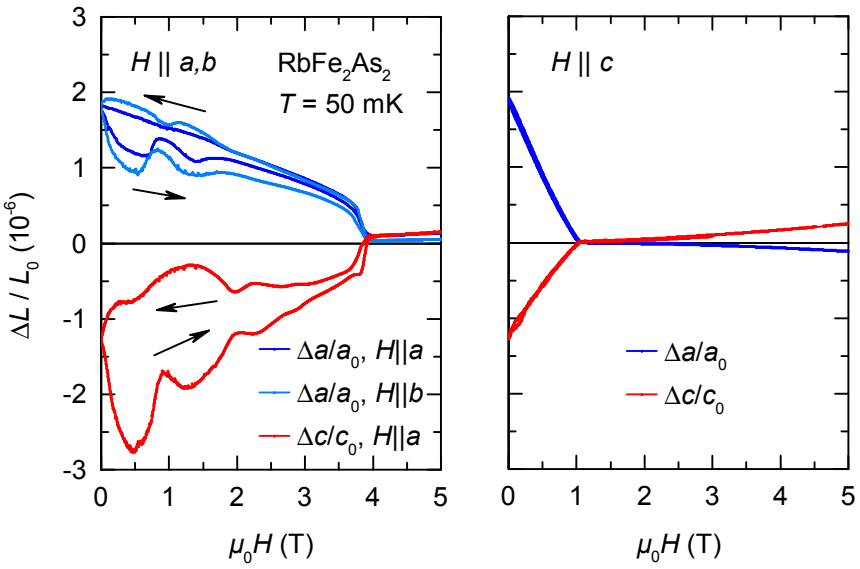


**Figure 4.7:** Relative changes in length $\Delta a/a_0$ and $\Delta c/c_0$ of $RbFe_2As_2$ at $T = 50\,\mathrm{mK}$ for $H \parallel ab$ (left) and $H \parallel c$ (right). For $H \parallel ab$ the magnetostriction is irreversible in the superconducting state. The transition is observed as a step-like anomaly. For $H \parallel c$ the dilation is a linear function of the magnetic field in the superconducting state. The transition is seen as a change in slope.

the superconducting order parameter decay exponentially on a length scale $\xi_{\mathrm{GL}}$, the Ginzburg-Landau coherence length. When $\kappa < 1/\sqrt{2}$, the surface energy is positive and the behavior of superconductivity in a magnetic field $H$ is of type I. The interior of the superconductor is perfectly shielded from the magnetic field by currents close to the surface until the thermodynamic critical field $H_c$ is reached. At $H_c$ there is an abrupt destruction of superconductivity. Depending on the demagnetization factor, there is an intermediate state of a type-I superconductor below $H_c$, in which macroscopic domains of superconductivity and the normal state exist next to each other. When $\kappa > 1/\sqrt{2}$, the surface energy is negative and the behavior of superconductivity in a magnetic field $H$ is of type II. Below a lower critical field $H_{c1}$ there is perfect shielding, but above $H_{c1}$, in the mixed state, magnetic field penetrates into the bulk of the superconductor until superconductivity is destroyed completely at the upper critical field $H_{c2}$. The penetration of magnetic field in the mixed state happens in the form of normal-conducting tubes, containing one flux quantum $\Phi_0 = h/2e$ each and the currents necessary to shield it. These entities are called vortices. With increasing field, the number of vortices increases, but not the magnetic flux per vortex. This way, the size of the interface between superconducting and normal-conducting regions is maximized, and with it the gain in surface energy $\sigma_{sn}$ compared to the loss in $U_c$. Under the influence of a demagnetization factor, there is an intermediate state of a type-II superconductor below $H_{c1}$, in which macroscopic domains of perfectly shielded superconductivity and of the mixed state exist next to each other.

Interactions between vortices and impurities and between vortices themselves can lead to a range of phenomena. Repulsive interactions between vortices are the reason for the formation of regular vortex lattices. The position of a vortex can be fixed, or "pinned", at an impurity [35]. When different parts of a vortex are pinned at different impurities, the vortex line can bend, acting against the stiffness of the vortex. This multitude of counteracting interactions can create several more or less ordered vortex states, with transitions tuned by the magnetic field, which changes the density of the vortices, or by the temperature, which changes their thermal energy. Apart from transitions, also avalanche effects may be observed. When one vortex is unpinned and retains sufficient kinetic energy to unpin other vortices in collisions, an avalanche of vortex movement is created, a time-dependent phenomenon, which might be observed as an anomaly in macroscopic quantities and is then referred to as "flux jump". A common effect is the appearance of a peak and a hysteresis in thermodynamic quantities just below the upper critical field. This effect is called "peak effect". Its origin, as proposed by Pippard [36], is a decrease in the rigidity of the vortex lattice close to the upper critical field, which leads to a sudden increase in vortex pinning.

The melting transition of a vortex lattice was observed in $Ba_{0.5}K_{0.5}Fe_2As_2$ in specific heat, thermal expansion, and magnetization measurements [37, 38]. In the thermal expansion coefficient this transition appears as a peak in the heating curve, a few Kelvin below the superconducting transition, at around 30 K [37, 38]. No such transition is seen in the thermal expansion of $KFe_2As_2$, $RbFe_2As_2$, or $CsFe_2As_2$. For these compounds the upper critical field and the transition temperature are much lower than for $Ba_{0.5}K_{0.5}Fe_2As_2$. Therefore, thermal fluctuations are not sufficient to melt the vortex lattice before superconductivity is destroyed.

Irreversibilities caused by vortices are observed in the magnetostriction of $KFe_2As_2$, $RbFe_2As_2$, or $CsFe_2As_2$ for $H \parallel ab$. Figure 4.8 shows the relative change in length $\Delta c/c_0$ of $CsFe_2As_2$ (sample 2) at several temperatures. Several peaks are observed at lowest temperatures, with similar distance in the magnetic field. A peak effect is visible close to the upper critical field. Also the magnetostriction of sample 1 shows a peak effect (see figure 4.9). But it does not show large equidistant peaks like the measurements on sample 2. Differences in impurity concentrations can lead to different vortex behavior. Also a dependence of the effect on the exact field direction could be an explanation for this difference.

## 4.4 The upper critical magnetic field measured by magnetostriction

The upper critical magnetic field of $KFe_2As_2$, $RbFe_2As_2$, and $CsFe_2As_2$ can easily be determined from the magnetostriction for $H \parallel c$. For this field direction, the magnetostriction $\Delta L/L$ in the superconducting state is mostly reversible, with a linear field dependence (see figure 4.7). The superconducting transition is observed as a change in slope of $\Delta L/L$ and as a step in the magnetostriction coefficient $\lambda_i$

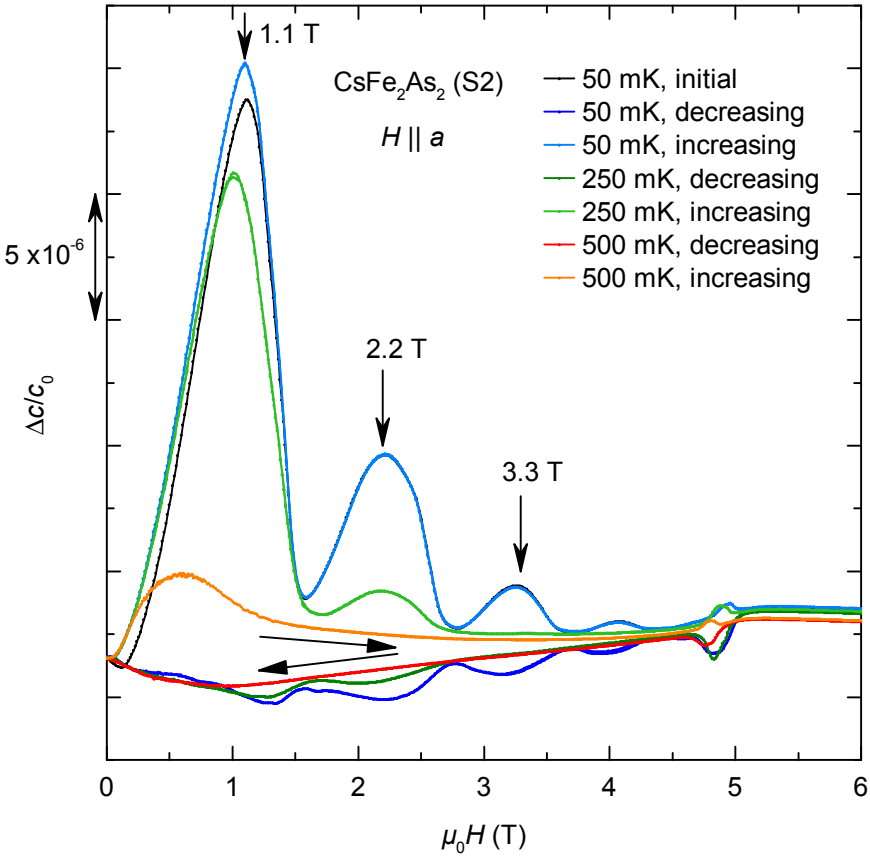


**Figure 4.8:** Relative change in length $\Delta c/c_0$ of $CsFe_2As_2$ (Sample 2) at $T = 50, 250, 500\,\mathrm{mK}$ for $H \parallel a$. The curves shown were recorded during a full field loop: the magnetic field was ramped $14 - (-7) - 14\,\mathrm{T}$. Therefore, two pairs of curves for decreasing and increasing magnetic field are shown for each temperature. The two curves for decreasing field and the two curves for increasing field fall on top of each other, as expected for the change in length, and are plotted using the same color and not listed separately in the legend. For 50 mK also an initial curve is shown. Several peaks are observed at lowest temperatures, with similar distance in the magnetic field (1.1 T). A peak effect is visible close to the upper critical field.

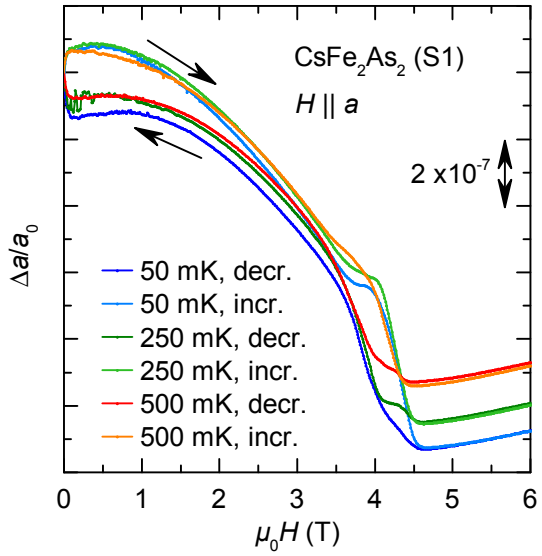


**Figure 4.9:** Relative change in length $\Delta a/a_0$ of $CsFe_2As_2$ (Sample 1) at $T = 50, 250, 500\,\mathrm{mK}$ for $H \parallel a$. A peak effect is visible close to the upper critical field.

for all temperatures (see figures 4.12, 4.13). When the position of the transition is taken as the midpoint of the step in $\lambda_i$, the resulting upper critical field $H_{c2}$ is consistent with the transition temperature $T_c$ deduced from the thermal expansion in the respective magnetic field.

For $H \parallel ab$ the situation is similar at temperatures $0.5T_c < T < T_c$. In this region the magnetostriction $\Delta L/L$ is linear in the superconducting state and the transition is visible as a step in the magnetostriction coefficient, accompanied by a small peak effect (see figures 4.7, 4.11, 4.9, 4.8). The upper critical field can be extracted from the position of the midpoint of the step. The character of the transition changes at temperatures $T \lesssim 0.5T_c$, when the anomaly at the transition develops from a step to a peak, signaling a discontinuous phase transition. Also, the irreversibilities increase at lower temperatures, including the peak effect. The proximity of the peak effect to the upper critical field makes it more difficult to extract $H_{c2}$ from the magnetostriction coefficient $\lambda_i$ (see figures 4.12, 4.13). When the position of $H_{c2}$ is taken as the midpoint of the first flank encountered coming from higher fields towards the transition, the resulting $H_{c2}$ is consistent with the position of the transition observed in thermal expansion. Therefore, this criterion is chosen for the determination of the upper critical field.

The upper critical field of $KFe_2As_2$ was studied by Zocco *et al.* [10]. Figure 4.10 shows $\Delta c/c_0$ of $KFe_2As_2$ for both $H \parallel c$ and $H \parallel a$ as well as $\lambda_c$ for $H \parallel a$ at different temperatures.

Figure 4.11 shows how the superconducting transition of $RbFe_2As_2$ develops from a change in slope of $\Delta a/a_0$ at higher temperatures to a step-like anomaly at lower

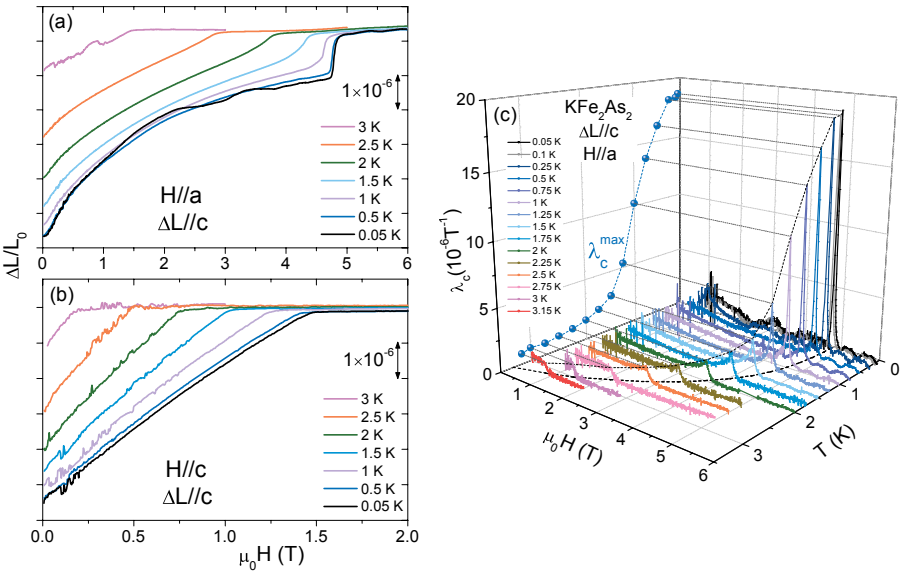


**Figure 4.10:** Left: change in length $\Delta c/c_0$ of $KFe_2As_2$ at different temperatures for $H \parallel a$ (a) and $H \parallel c$ (b). Right: magnetostriction coefficient $\lambda_c$ for $H \parallel a$. Taken from [10].

temperatures for $H \parallel ab$. In the magnetostriction coefficient this is observed as a development of the transition from a step to a peak (see figure 4.12). Thus, for all three compounds, $KFe_2As_2$, $RbFe_2As_2$, and $CsFe_2As_2$, the upper critical field shows very similar behavior. For $H \parallel c$ the superconducting transition is continuous at all temperatures. For $H \parallel ab$ the superconducting transition is continuous at higher temperatures, but becomes discontinuous at lower temperatures.

## 4.5 Phase diagrams

Tracking the anomalies in thermal expansion and magnetostriction, $H$-$T$ phase diagrams were mapped out. The left-hand panel of figure 4.14 shows the phase diagrams of $KFe_2As_2$, $RbFe_2As_2$, and $CsFe_2As_2$. The superconducting transition temperature $T_c$ decreases monotonically in the series, from 3.4 K, to 2.5 K, to 2.25 K. The behavior of the upper critical field is more complicated. For $H \parallel c$ the upper critical field $\mu_0 H_{c2}^{\parallel c}$ is 1.5 T, 1.0 T, and 1.8 T, respectively. Thus, there is no monotonic trend in the series. For $H \parallel a$ the upper critical field $\mu_0 H_{c2}^{\parallel a}$ is 4.8 T, 4.0 T, and 4.5 T, respectively. Again, there is no monotonic trend. The right-hand panel of figure 4.14 shows the normalized phase diagrams. The curves of $H_{c2}^{\parallel c}/H_{c2}^{\parallel c}(T = 0)$ as a function of $T/T_c$ fall on top of each other, while the curves of $H_{c2}^{\parallel a}/H_{c2}^{\parallel a}(T = 0)$ fan out towards larger values. The anisotropy $H_{c2}^{\parallel a}/H_{c2}^{\parallel c}$ is shown in figure 4.15. It increases with temperature. From $KFe_2As_2$ to $RbFe_2As_2$ the anisotropy increases, but it decreases again from $RbFe_2As_2$ to $CsFe_2As_2$ below the values for $KFe_2As_2$. This

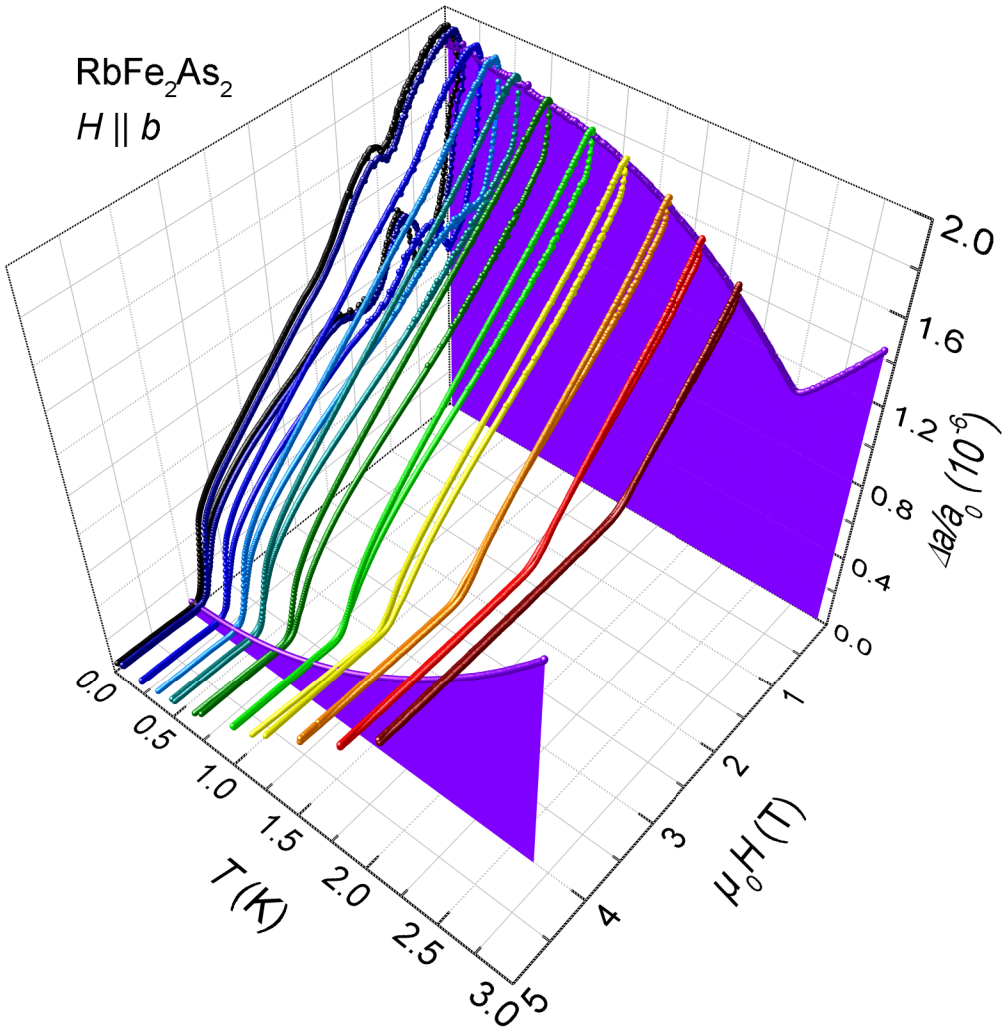


**Figure 4.11:** Relative change in length $\Delta a/a_0$ of $RbFe_2As_2$ at different temperatures between 50 mK and 2 K for decreasing and increasing magnetic field $H \parallel b$. The superconducting transition develops from a change in slope at higher temperatures to a step-like anomaly at lower temperatures. Irreversibilities increase at lower temperatures (the upper curve at each temperature was recorded in a decreasing field). The two violet curves are thermal expansion curves at 0 T and at 4 T.

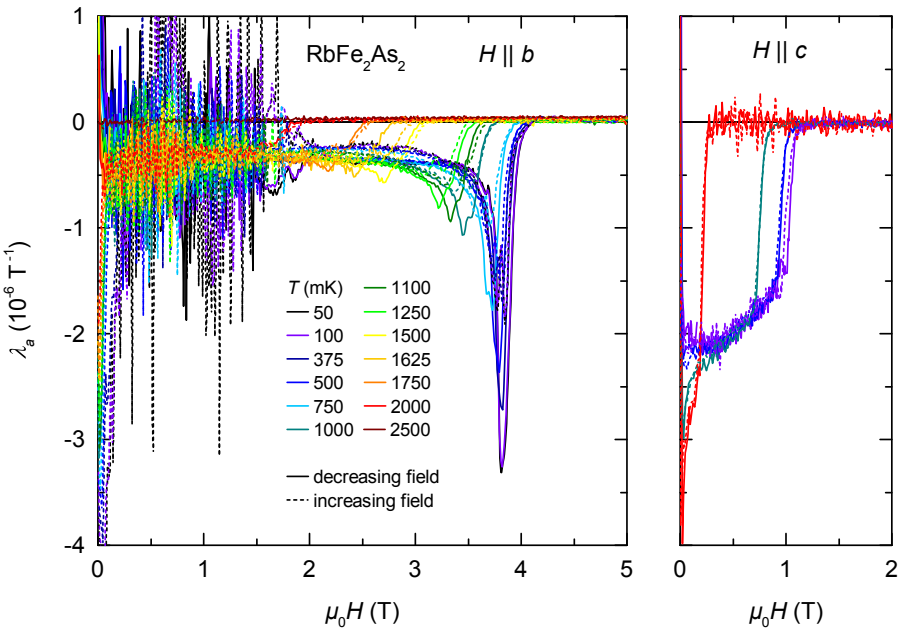


**Figure 4.12:** Magnetostriction coefficient $\lambda_a$ of $RbFe_2As_2$ at different temperatures for $H \parallel b$ (left) and $H \parallel c$ (right), for decreasing (solid line) and increasing (dashed line) field. For $H \parallel b$ the magnetostriction coefficient $\lambda_a$ develops a negative peak at low temperatures. It displays irreversibilities in the superconducting state, with a peak effect close to the upper critical field. For $H \parallel c$ it retains a step-like anomaly down to lowest temperatures. Small irreversibilities close to $H_{c2}$ only show up at low temperatures.

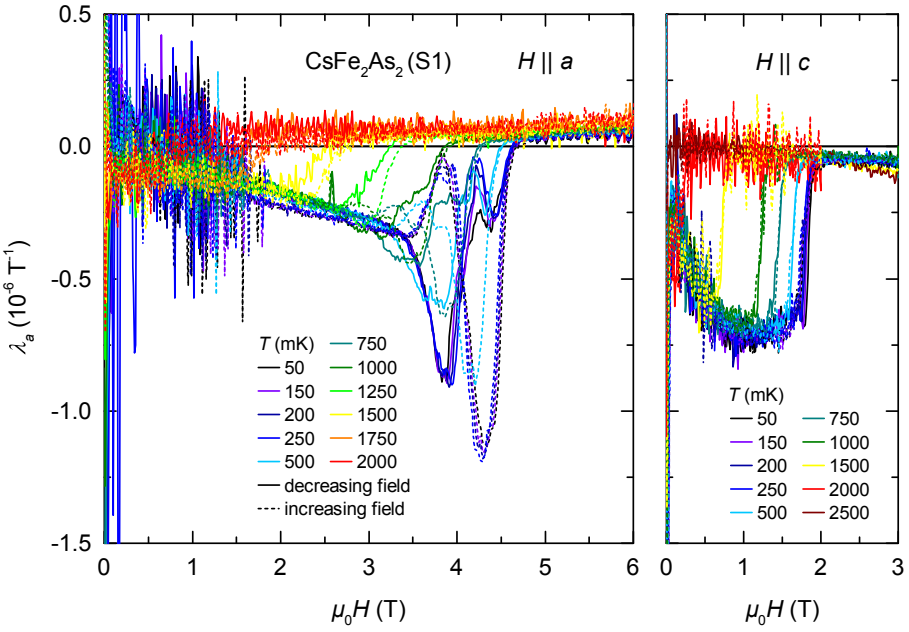


**Figure 4.13:** Magnetostriction coefficient $\lambda_a$ of $CsFe_2As_2$ at different temperatures for $H \parallel a$ (left) and $H \parallel c$ (right), for decreasing (solid line) and increasing (dashed line) field. For $H \parallel a$ the magnetostriction coefficient $\lambda_a$ develops a negative peak at low temperatures. It displays irreversibilities in the superconducting state, with a peak effect close to the upper critical field. For $H \parallel c$ it retains a step-like anomaly down to lowest temperatures. Small irreversibilities close to $H_{c2}$ only show up at low temperatures.

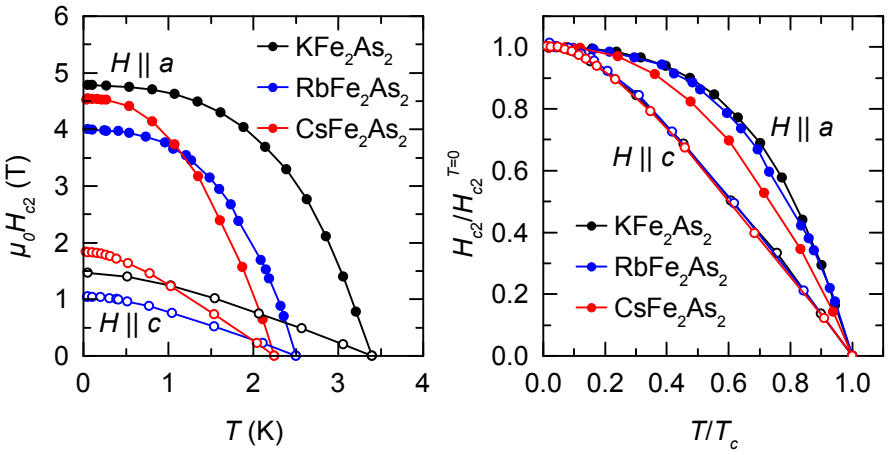


**Figure 4.14:** Left: Phase diagrams of $KFe_2As_2$, $RbFe_2As_2$, and $CsFe_2As_2$ for $H \parallel a$ (closed symbols) and $H \parallel c$ (open symbols). Right: Normalized phase diagrams.

behavior is not simply related to structural measures of anisotropy like $c/a$ or $h_{As}/a$ (see figure 2.2). Also the distance between FeAs layers, $c(1-2z)$, or the distance between FeAs layers divided by the thickness of a FeAs layer, $(0.5-z)/(z-0.25)$, do not correlate directly with the anisotropy of the upper critical field.

## 4.6 Limiting mechanisms of the upper critical field

A magnetic field destroys superconductivity in type-II superconductors by means of two mechanisms [34, 39]. The first mechanism is the orbital limiting. When the kinetic energy of the collective cyclotron motion of the Cooper pairs surpasses the superconducting condensation energy, superconductivity is destroyed [40]. In an increasing magnetic field the distance between vortices, regions of normal-conducting material, decreases until vortices overlap and superconductivity is destroyed. This is a continuous transition [39]. The second mechanism is the Pauli or paramagnetic limiting, present only in spin-singlet superconductors. When the energy gained by aligning all spins parallel to the magnetic field surpasses the superconducting condensation energy, Cooper pairs are destroyed. This is a discontinuous transition [39]. There are always both mechanisms at work. In many cases the effect of paramagnetic limiting is small, so that $H_{c2} \approx H_{orb}$ [34]. But in cases when the Pauli susceptibility is large, the free energy of the normal state in a magnetic field equals the free energy of a superconductor in the mixed state well below $H_{orb}$ and a discontinuous transition at $H_{c2}$ is observed (see figure 4.16).

Other effects that may affect the upper critical field, apart from the gap symmetry and anisotropy, are scattering by non-magnetic or magnetic impurities, the coupling strength, spin-orbit coupling, and, in the case of multiband superconductors, inter-

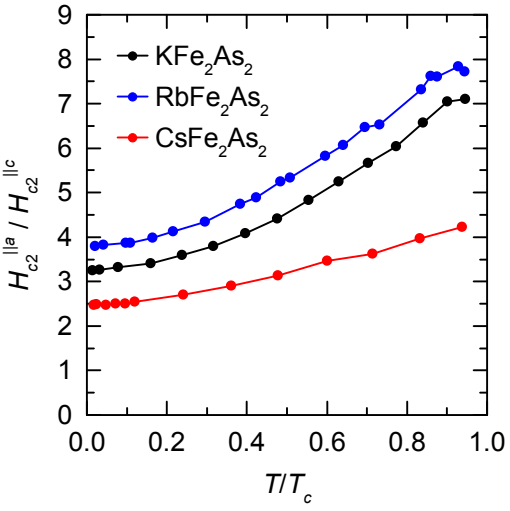


**Figure 4.15:** Anisotropy of the upper critical fields of $KFe_2As_2$, $RbFe_2As_2$, and $CsFe_2As_2$.

band scattering [27, 34].

Limiting effects of the upper critical field can be analyzed and related to theoretical predictions using a plot of $H_{c2}/T_c \left|\frac{\partial H_{c2}}{\partial T}\right|_{T=T_c}$ as a function of $T/T_c$ [39, 41]. Figure 4.17 compares these plots for $KFe_2As_2$, $RbFe_2As_2$, and $CsFe_2As_2$. For $H \parallel c$ all curves fall on top of each other and terminate at approximately 0.73 for $T = 0$, which is very close to the expected value for a purely orbitally limited upper critical field in the clean limit, for an isotropic, single band (0.727) [41]. Despite these restrictions, for which the prediction holds, similar values have not only been found for nearly isotropic conventional superconductors, but often also for anisotropic and multiband superconductors, when the magnetic field was applied along a uniaxial direction like the $c$-axis [27]. For $H \parallel a$ the curves terminate at different, lower values for $T = 0$ due to the effect of paramagnetic limiting. This lowering of the upper critical field may explain the decrease of the anisotropy $H_{c2}^{\parallel a}/H_{c2}^{\parallel c}$ with lower temperatures (see figure 4.15).

To find out at which temperature the upper critical field becomes paramagnetically limited, the maximum value of the peak-like anomaly in the magnetostriction coefficient, $\lambda_{max}$, is taken as a measure of how discontinuous the transition is. This might be problematic for the case of $CsFe_2As_2$, where the peak effect affects the magnetostriction coefficient very close to the transition (see figure 4.13). Figure 4.18 shows the normalized $\lambda_{max}/\lambda_{max}(T = 0)$ at $H_{c2}$ as a function of $T/T_c$ for $KFe_2As_2$, $RbFe_2As_2$, and $CsFe_2As_2$. By the criterion displayed in figure 4.18, an approximate tricritical temperature, below which the transition becomes discontinuous, can be obtained. This temperature is roughly the same fraction of $T_c$ for all three compounds, about $0.5\,T_c$.

The anisotropy of the orbitally limited upper critical field $H_{orb}$ is related to the

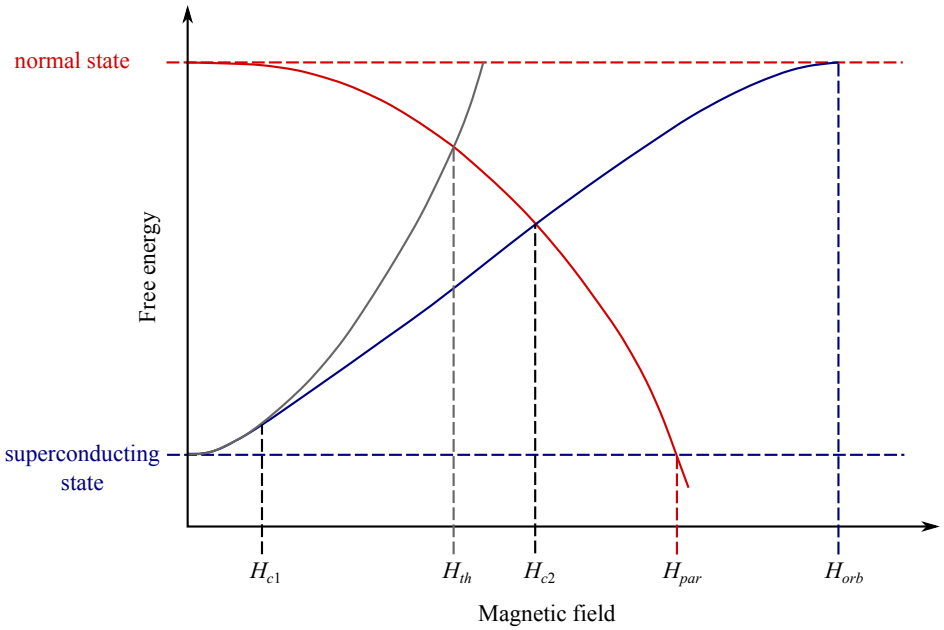


**Figure 4.16:** Schematic plot of the free energy at $T = 0$ as a function of an applied magnetic field for the normal state and for the superconducting state (after [39]). The free energy of the normal state ($\propto -\chi_s H^2$, solid, red line) decreases with the magnetic field due to the Pauli spin susceptibility $\chi_s$. In the limit of exclusively paramagnetic limiting, it crosses the free energy of the superconducting state (horizontal, blue, dashed line) at $H_{par}$. During the transition from the superconducting state to the normal state, the free energy would change its slope. Therefore, the transition at $H_{par}$ would be discontinuous. The free energy of a type-I superconductor follows the grey line, with a discontinuous transition at the thermodynamic critical field $H_{th}$, which is lowered by spin paramagnetism compared to the case without spin paramagnetism. A type-II superconductor has a mixed state above the lower critical field $H_{c1}$. Its free energy (solid, blue line), in the limit of absent spin paramagnetism in the normal state, would approach the free energy of the normal state tangentially at $H_{orb}$. During the transition, the free energy would change its curvature, but not its slope. Therefore, the transition at $H_{orb}$ would be continuous. When spin paramagnetism in the normal state is not negligible, the free energy of the superconducting state crosses the free energy of the normal state at $H_{c2}$. It changes its slope in the transition that is thus discontinuous.

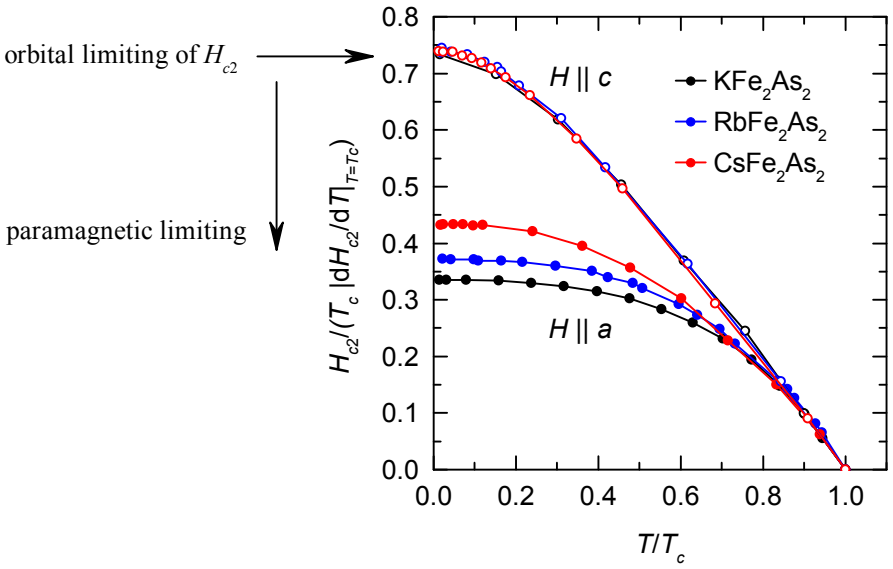


**Figure 4.17:** Upper critical field $H_{c2}$ of $KFe_2As_2$, $RbFe_2As_2$, and $CsFe_2As_2$ for $H \parallel a$ (closed symbols) and $H \parallel c$ (open symbols), normalized by $T_c \cdot |\partial H_{c2}/\partial T_c|_{T=T_c}$. For $H \parallel c$ all curves fall on top of each other and terminate at approximately 0.73 for $T = 0$, which is the expected value for an orbitally limited $H_{c2}$ in the clean limit with $g = 0$ [41]. For $H \parallel a$ the curves terminate at different, lower values for $T = 0$ due to the effect of paramagnetic limiting [39].

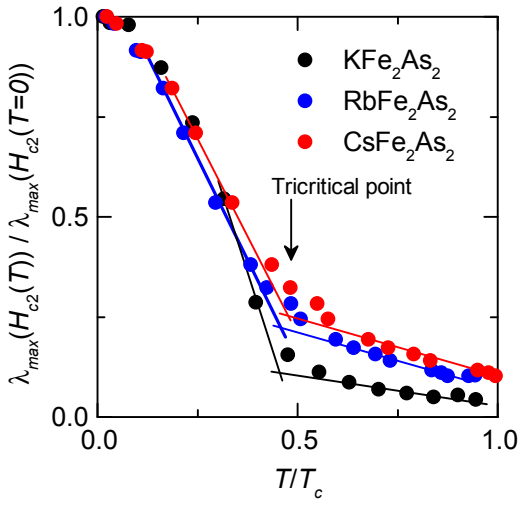


**Figure 4.18:** Normalized peak value of the magnetostriction coefficient at the upper critical field of $KFe_2As_2$, $RbFe_2As_2$, and $CsFe_2As_2$ for $H \parallel a$. Especially for $CsFe_2As_2$, this value might be affected by the peak effect close to the transition. The reduced temperature $T/T_c$ below which the transition becomes discontinuous (the tricritical point) is approximately the same for all compounds.

anisotropy of the Ginzburg-Landau coherence length $\xi_{\mathrm{GL}}$ via [27]

$$\Gamma \equiv \frac{H_{orb}^{\parallel ab}}{H_{orb}^{\parallel c}} = \frac{\xi_{\mathrm{GL}}^{ab}}{\xi_{\mathrm{GL}}^{c}}, \tag{4.1}$$

since

$$\mu_0 H_{orb}^{\parallel c} = \frac{\Phi_0}{2\pi(\xi_{\mathrm{GL}}^{ab})^2}, \quad \mu_0 H_{orb}^{\parallel ab} = \frac{\Phi_0}{2\pi \xi_{\mathrm{GL}}^{ab} \xi_{\mathrm{GL}}^{c}}. \tag{4.2}$$

As the upper critical field $H_{c2}^{\parallel c}$ of $KFe_2As_2$, $RbFe_2As_2$, and $CsFe_2As_2$ is orbitally limited, $\xi_{\mathrm{GL}}^{ab}$ can be determined using equation 4.2. The coherence length $\xi_{\mathrm{GL}}^{c}$ can then be calculated from the anisotropy at $T = T_c$ (figure 4.15) or from the anisotropy of the slope $\left|\frac{\partial H_{c2}}{\partial T}\right|_{T=T_c}$ (figure 4.14) using equation 4.1. The coherence length is related to the Fermi velocity via $\xi \propto \hbar v_{\mathrm{F}}/(k_{\mathrm{B}} T_c)$ [34]. This Fermi velocity $v_{\mathrm{F}}$ results from an integral over the Fermi surface and from an average over multiple bands [27]. The orbitally limited $H_{orb}^{\parallel ab}$ can also be determined from the anisotropy and equation 4.1. Critical quantities and coherence lengths of $KFe_2As_2$, $RbFe_2As_2$, and $CsFe_2As_2$ are listed in table 4.6. Since the mean free paths $l$ ($l > 100\,\mathrm{nm}$ for the *ac*-plane, see section 5.2.4) are larger than the Ginzburg-Landau coherence lengths, superconductivity in $KFe_2As_2$, $RbFe_2As_2$, and $CsFe_2As_2$ can be described in the so-called clean limit ($l \gg \xi_{\mathrm{GL}}$). This is consistent with the observation that

**Table 4.1:** Critical quantities and coherence lengths.

| | $T_c$ | $\mu_0 H_{c2}^{\parallel c}$ | $\mu_0 H_{c2}^{\parallel ab}$ | $\mu_0 H_{orb}^{\parallel ab}$ | $\left\lvert\frac{\partial \mu_0 H_{c2}^{\parallel c}}{\partial T}\right\rvert_{T_c}$ | $\left\lvert\frac{\partial \mu_0 H_{c2}^{\parallel ab}}{\partial T}\right\rvert_{T_c}$ | $\xi_{\mathrm{GL}}^{c}$ | $\xi_{\mathrm{GL}}^{ab}$ |
|---|---|---|---|---|---|---|---|---|
| | K | T | T | T | T/K | T/K | nm | nm |
| $KFe_2As_2$ | 3.4 | 1.5 | 4.8 | 10.4 | 0.59 | 4.19 | 2.1 | 14.8 |
| $RbFe_2As_2$ | 2.5 | 1.0 | 4.0 | 7.8 | 0.57 | 4.30 | 2.4 | 18.1 |
| $CsFe_2As_2$ | 2.25 | 1.8 | 4.5 | 7.6 | 1.10 | 4.66 | 3.2 | 13.5 |

$H_{c2}/T_c \left|\frac{\partial H_{c2}}{\partial T}\right|_{T=T_c}$ for $T = 0$ is approximately equal to the predicted value 0.73 [39] for $H \parallel c$.

## 4.7 Conclusions

$KFe_2As_2$, $RbFe_2As_2$, and $CsFe_2As_2$ are a series of iron-based materials with similar superconducting properties. They enable the study of multiband superconductivity in systems that are clean compared to other materials, due to the absence of additional disorder that would be introduced by substitutional atoms. Superconductivity can be described in the clean limit. The upper critical field becomes paramagnetically limited at low temperatures for the magnetic field in the *ab*-plane.

# 5 Quantum oscillations and electronic correlations in $KFe_2As_2$, $RbFe_2As_2$, and $CsFe_2As_2$

## 5.1 Electronic correlations in iron-based superconductors

### 5.1.1 Electronic correlations in a Fermi liquid

Electronic correlations are the restriction of the free movement of electrons by other electrons. Correlating mechanisms can be direct Coulomb interactions acting on the charge or exchange interactions acting on the spin via the Pauli principle. Already in the absence of electronic correlations or other many-body interactions, the effective mass of an electron in a metal deviates from the free electron mass. The effective mass that results directly from the dispersion $E(\boldsymbol{k})$ of non-interacting electrons, i.e., the band structure, is called the band mass $m_b$. The inverse tensor of the band mass is

$$m^{-1}_{b,r,\,i,j}(\boldsymbol{k}) = \frac{1}{\hbar^2}\frac{\partial^2 E_r(\boldsymbol{k})}{\partial k_i \partial k_j} \tag{5.1}$$

where $r$ is the band index. The band mass is larger when the curvature of the dispersion is smaller, which is typically the case close to the boundaries of the Brillouin zone. Spin-orbit coupling can increase the band mass, for example in $p$-electron systems like some semiconductors, and should therefore be included in calculations of $m_b$.

If the excitations of an interacting electron system have a one-to-one correspondence to those of the noninteracting system, their properties can be phenomenologically described by the effective quasiparticle mass $m^*$,

$$m^* = m_b(1 + \frac{1}{3}F_1^s), \tag{5.2}$$

where $F_1^s$ is a Landau parameter [42].

The interface between experimental observations and a theoretical many-body description is the spectral function $A(\boldsymbol{k}, \omega)$. The spectral weight of its quasiparticle peak, $Z_{\boldsymbol{k}}$, is proportional to the inverse of the mass enhancement caused by many-body interactions [42]

$$Z_{\boldsymbol{k}} \propto \frac{m_b}{m^*}. \tag{5.3}$$

The enhanced density of states at the Fermi energy for every spin quantum number $s$ is

$$D_s(E_\mathrm{F}) = \frac{m_s^* k_{\mathrm{F},s}}{\pi^2 \hbar^2}, \tag{5.4}$$

where $\hbar k_\mathrm{F}$ is the quasiparticle momentum at the Fermi energy $E_\mathrm{F}$. The larger density of states can be measured as an enhanced Sommerfeld coefficient of the specific heat

$$\gamma = \frac{\pi^2}{3} k_\mathrm{B}^2 D(E_\mathrm{F}), \tag{5.5}$$

where $D(E_\mathrm{F}) = \sum_s D_s(E_\mathrm{F})$, and a modified spin susceptibility

$$\chi_s = \left(\frac{g}{2}\frac{e\hbar}{2m_e}\right)^2 \frac{D(E_\mathrm{F})}{1+F_0^a}, \tag{5.6}$$

where $g$ is the $g$-factor, $m_e$ is the free electron mass, and $F_0^a$ is a Landau parameter [42]. Other quantities that reveal correlations are, for example, the spectral function measured by ARPES, the Drude weight in optical conductivity spectra, or the effective mass determined from the temperature dependence of the amplitudes of quantum oscillations.

### 5.1.2 Experimental signs of correlations in iron-based superconductors

Electronic correlations in iron-based superconductors have been revealed experimentally in several compounds (see Ref. [3] for a review by Johnston). Stewart [5] stressed in his review that the measured Sommerfeld coefficients could not be explained by band structure calculations on the level of density functional theory. Yin *et al.* [43] compiled experimentally obtained effective masses and attempted to model them with calculations in the framework of dynamical mean-field theory (DMFT). de' Medici *et al.* [44] extracted a trend in the correlations of 122-compounds, which increase notably in the $Ba_{1-x}K_xFe_2As_2$ series. The end member of this series, $KFe_2As_2$, is one of the iron-based superconductors with the largest mass enhancements. Hardy *et al.* [9] discussed a proximity of selected bands to a Mott transition as a possible reason for the large Sommerfeld coefficient and spin susceptibility (see section 5.4.2). Of the known 122-compounds only $RbFe_2As_2$ and $CsFe_2As_2$ have larger Sommerfeld coefficients [11] and effective quasiparticle masses (this work) than $KFe_2As_2$.

It is instructive to compare three extensively studied substitution series with $BaFe_2As_2$ as the mother compound with respect to electronic correlations: the iron-cobalt series $Ba(Fe_{1-x}Co_x)_2As_2$, the barium-potassium series $Ba_{1-x}K_xFe_2As_2$, and the arsenic-phosphorus series $BaFe_2(As_{1-x}P_x)_2$. In the $Ba(Fe_{1-x}Co_x)_2As_2$ series mass enhancements are small, about a factor of 2, for all $x$, despite an increase of the Sommerfeld coefficient around the superconducting dome and at larger $x$ [32].

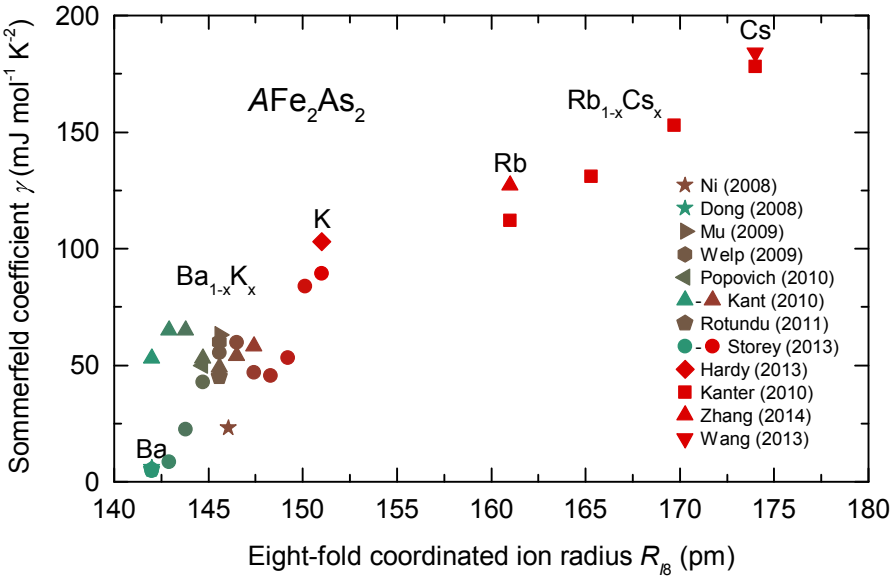


**Figure 5.1:** The Sommerfeld coefficient of the specific heat $\gamma$ of $Ba_{1-x}K_xFe_2As_2$ [46] and $Rb_{1-x}Cs_xFe_2As_2$ [11], plotted against the eight-fold coordinated ion radius $R_{I8}$ of the alkali or alkaline earth atom. Replacing Ba by K in the $Ba_{1-x}K_xFe_2As_2$ not only increases $R_{I8}$, but also dopes holes, up to 0.5 holes per iron atom for $KFe_2As_2$.

In the $BaFe_2(As_{1-x}P_x)_2$ series there is a mass enhancement of a factor of 4 to 10 in the vicinity of the putative quantum critical point hidden by the superconducting dome, but otherwise the mass enhancement factor is small, approximately 2 [45]. Only in the $Ba_{1-x}K_xFe_2As_2$ series does the mass enhancement factor increase with substitution, from about 2 to 9 [44]. Storey *et al.* [46] measured the specific heat of the $Ba_{1-x}K_xFe_2As_2$ series, which exhibits an increasing Sommerfeld coefficient (see figure 5.1).

The proximity to a Mott localization of charge carriers leads to bad metallicity [3]. In iron-based superconductors the electrical resistivity at room temperature is large, even when the residual resistivity at low temperatures is small [3]. The mean free path of quasiparticles at room temperature is of the same order of magnitude as the Fermi wavelength, which is a hallmark of bad metallicity in proximity to a Mott transition [47]. Figure 5.2 from [48] compares the resistivity of three 122 substitution series and highlights the bad metallicity in $Ba_{1-x}K_xFe_2As_2$.

Also, the small Drude weight observed in optical conductivity spectra is a sign of correlations, since this quantity is inversely proportional to the effective charge carrier mass [3, 47, 49]. Of the three substitution series with $BaFe_2As_2$ as the mother compound, namely $Ba(Fe_{1-x}Co_x)_2As_2$, $Ba_{1-x}K_xFe_2As_2$, and $BaFe_2(As_{1-x}P_x)_2$, only the (Ba,K)-122 series exhibits a decreasing Drude weight [48, 50] (see figure 5.3).

There is an apparent discrepancy between mass enhancements measured by spe-

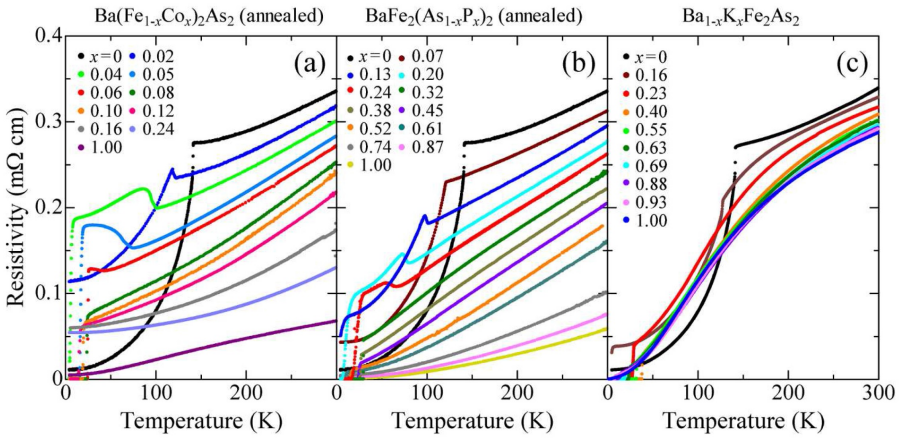


**Figure 5.2:** In-plane resistivity of three 122 substitution series, taken from Nakajima *et al.* [48]. The room-temperature resistivity of $Ba_{1-x}K_xFe_2As_2$ remains large for all $x$.

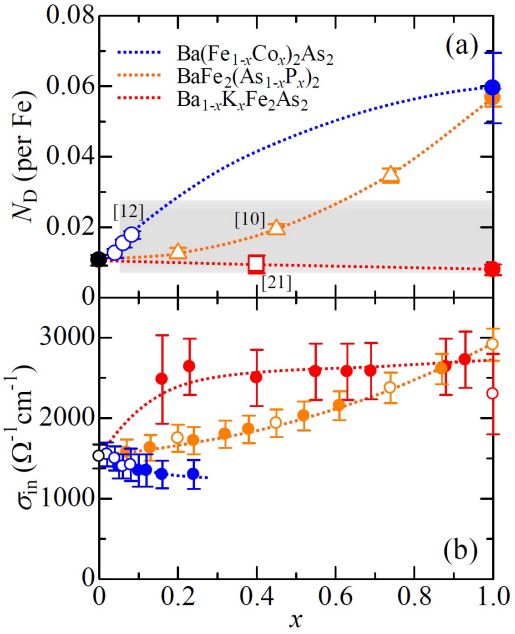


**Figure 5.3:** Spectral weight of the narrow (a) and broad (b) Drude component of optical conductivity spectra, taken from Nakajima *et al.* [48]. The Drude weight of the narrow component decreases for $Ba_{1-x}K_xFe_2As_2$.

cific heat and optical conductivity which can be explained with the multiband nature of the materials [44]. While the density of states is proportional to a sum of terms $m^*/m_b$, the Drude weight is proportional to a sum of terms $m_b/m^*$. Therefore, the density of states is dominated by the mass enhancement of the heaviest band, while the Drude weight is dominated by the smallest mass enhancement. A difference in mass enhancements between different bands can be directly observed in ARPES or quantum oscillation measurements. Yoshida *et al.* [13] measured the Fermi surface of $KFe_2As_2$ with ARPES (see figure 5.11). They also determined mass enhancements for all bands, which compare well with the de Haas-van Alphen data of Terashima *et al.* [12]. For reviews on quantum oscillation studies of other iron-based superconductors see [51, 52].

## 5.2 Quantum oscillations in the magnetostriction

### 5.2.1 Theoretical description

A means to study electronic correlations in a material is to measure quantum oscillations and to extract effective quasiparticle masses of each band from the temperature dependence of the oscillation amplitudes. In contrast to the cumulative measure of correlations, the Sommerfeld coefficient of the specific heat, quantum oscillations yield a measure of the strength of correlations on a per band basis. Compared to ARPES, quantum oscillation measurements have the advantage of being a bulk probe not sensitive to the surface of the sample. Disadvantages are the need for high magnetic fields and very pure samples.

A magnetic field modifies the dispersion of quasiparticles perpendicular to the magnetic field. Assuming a magnetic field $\boldsymbol{B} = B\hat{\mathrm{e}}_z$ along the $z$-direction, quasiparticles will move on closed orbits in the $xy$-plane and occupy Landau levels

$$E_n(\boldsymbol{k}) = \hbar\omega_c \left(n + \frac{1}{2}\right) + E(k_z) \pm \frac{1}{2} g\mu_\mathrm{B} B, \quad n = 0, 1, 2, ..., \tag{5.7}$$

where $\omega_c$ is the cyclotron frequency,

$$\omega_c = \frac{eB}{m^*}, \tag{5.8}$$

and $g$ is the $g$-factor, which is $g = 2$ for free electrons. In momentum space the states lie on Landau tubes aligned in the $z$-direction with cross-sections in the $xy$-plane

$$S_n = \frac{2\pi e}{\hbar} \left(n + \frac{1}{2} \pm \frac{1}{4} g\right) B, \quad n = 0, 1, 2, ... \tag{5.9}$$

With increasing magnetic field the cross-sections of the Landau tubes grow, so that one Landau tube after the other traverses the Fermi surface with cross-section $A$. When this happens, a peak in the density of states crosses the Fermi energy, causing

oscillations in many physical quantities. For quasiparticles of each spin oscillations with a period in the inverse magnetic field

$$\Delta\left(\frac{1}{B}\right) = \frac{2\pi e}{\hbar}\frac{1}{A} \tag{5.10}$$

are observed [53]. In case $g = 2$, the phase difference between the oscillations from spin-up and spin-down quasiparticles is not noticed because it coincides with the period.

A common method to measure quantum oscillations is to use the de Haas-van Alphen effect, oscillations in the magnetization $M$. According to the Lifshitz-Kosevich formula [53] for the oscillatory part of the magnetization $\widetilde{M}$:

$$\widetilde{M} = \sum_r \widetilde{M}_r = \sum_{r,p} a_{r,p} \sin\left(\frac{2\pi p F_r}{B} + \phi_{r,p}\right). \tag{5.11}$$

Here, the index $r$ counts the different frequencies $F_r$ observed as well as their contributions $\widetilde{M}_r$ to the oscillatory magnetization parallel to the magnetic field $B$. The index $p$ counts the harmonics, $\phi_{r,p}$ are the phases and $a_{r,p}$ are the amplitudes:

$$a_{r,p} \propto \frac{F_r}{\mu_r^* p^{3/2}} B^{1/2} C_r R_{T,r,p} R_{D,r,p} R_{S,r,p}, \tag{5.12}$$

where $C_r$ is the curvature factor of the cross-section $A_r$ of the Fermi surface:

$$C_r = \left|\frac{\partial^2 A_r}{\partial k_\parallel^2}\right|^{-1/2}, \tag{5.13}$$

so that the smaller the curvature in the direction of the magnetic field, the larger the amplitude. The largest amplitude results from a two-dimensional Fermi surface when the field is applied along its normal.

The temperature factor $R_T$ describes the temperature-dependence of the amplitudes with one free parameter, the mass enhancement factor $\mu^* \equiv m^*/m_e$ with respect to the free electron mass $m_e$.

$$R_{T,r,p} = \frac{X}{\sinh(X)}, \quad X = \frac{2\pi^2 p k_\mathrm{B} T \mu_r^*}{e\hbar B}. \tag{5.14}$$

Therefore, average effective masses $m_r^*$ can be determined for each observed orbit $r$ by fitting $R_{T,r,p}$ to the measured amplitude as a function of temperature. When the amplitudes are obtained by means of a Fourier transform over a range of inverse fields, the single magnetic field $B$ in $R_T$ is taken as the average of the inverse applied magnetic fields that limit this range.

The Dingle factor $R_D$ describes the effect of impurity scattering on the amplitudes.

$$R_{D,r,p} = \exp\left(-\frac{\pi p m_{b,r}}{eB\tau_r}\right) = \exp\left(-\frac{\pi\hbar p k_{\mathrm{F},r}}{eBl_r}\right). \tag{5.15}$$

The approximation of a circular Fermi surface cross section, $\pi k_{\mathrm{F}}^2 = A = 2\pi eF/\hbar$ allows the extraction of the mean free path $l = \tau v_{\mathrm{F}}$ from the $B$-dependence of the oscillation amplitudes.

$$R_{D,r,p} \approx \exp\left(-\pi p \sqrt{\frac{2\hbar}{e}} \frac{\sqrt{F_r}}{B l_r}\right). \tag{5.16}$$

The spin-splitting factor $R_S$ describes the influence of the splitting of the energy levels of spin-up and spin-down quasiparticles by $g^*\mu_{\mathrm{B}}B$. This introduces a phase difference between quantum oscillations originating from spin-up and spin-down quasiparticles, reducing the amplitude by a factor

$$R_{S,r,p} = \cos\left(\frac{\pi p m_{s,r}^* g_r^*}{2m_e}\right), \tag{5.17}$$

where $m_s^*$ is the so-called spin mass which is renormalized by electron-electron interactions only, in contrast to the effective quasi-particle mass $m^*$, which is also renormalized by electron-phonon interaction [52]. The effective $g$-factor $g^*$ is two for free electrons. A complication arises when there is an appreciable difference in the effective masses of spin-up and spin-down quasiparticles $m_\uparrow^*$ and $m_\downarrow^*$ [54]. If this is the case, the contributions of spin-up and spin-down quasiparticles to the oscillatory magnetization must be considered separately, with amplitudes $a_\uparrow$ and $a_\downarrow$, and phases $\phi_\uparrow$ and $\phi_\downarrow$.

In this work quantum oscillations were measured in the magnetostriction. The effect of oscillatory magnetostriction was predicted by Chandrasekhar [55] and first observed by Green and Chandrasekhar [56] in bismuth in 1963. The strain $\epsilon_{ij}$ can be deduced from the Gibbs free energy (see equation 3.9) via

$$\epsilon_{ij} = -\frac{1}{V}\frac{\partial G}{\partial \sigma_{ij}}. \tag{5.18}$$

Alternatively, the magnetostriction coefficient $\lambda$ can be deduced directly from the stress dependence of the magnetization

$$\lambda_{ijk} = \frac{1}{V}\frac{\partial M_k}{\partial \sigma_{ij}}. \tag{5.19}$$

Considering only a magnetization $M$ parallel to the applied field and only uniaxial pressure in perpendicular directions $p_i \equiv -\sigma_{ii}$, $i = a, c$ or $i = 1, 3$, (as for equation 3.13; not to be confused with the summation index $p$ counting the harmonics), the

Lifshitz-Kosevich formula for the oscillatory magnetostriction coefficient becomes

$$\begin{aligned}\widetilde{\lambda_i} &= -\frac{1}{V}\frac{\partial\widetilde{M}}{\partial p_i} \\ &= -\frac{1}{V}\sum_{r,p,s}\Bigg[\frac{\partial F_r}{\partial p_i}\frac{a_{r,p,s}}{F_r}\left(\sin\left(\frac{2\pi pF_r}{B}+\phi_{r,p,s}\right)+\frac{2\pi pF_r}{B}\cos\left(\frac{2\pi pF_r}{B}+\phi_{r,p,s}\right)\right) \\ &\qquad + \frac{\partial(a_{r,p,s}/F_r)}{\partial p_i}F_r\sin\left(\frac{2\pi pF_r}{B}+\phi_{r,p,s}\right) \\ &\qquad + \frac{\partial\phi_{r,p,s}}{\partial p_i}a_{r,p,s}\cos\left(\frac{2\pi pF_r}{B}+\phi_{r,p,s}\right)\Bigg],\end{aligned} \tag{5.20}$$

where the symbols have the same meaning as for equations 5.11 to 5.17, but an additional index $s =\uparrow,\downarrow$ was introduced to account for spin-dependent effective masses and phases. In the simplest case, the pressure dependence of the cross-section of the Fermi surface is much larger than the pressure dependence of the effective mass, of the effective $g$-factor, or of the phase. Then the oscillatory magnetostriction is approximately [53, 57, 58]

$$\widetilde{\lambda_i} \approx -\frac{1}{V}\sum_{r,p,s}\frac{\partial F_r}{\partial p_i}\frac{2\pi p}{B}a_{r,p,s}\cos\left(\frac{2\pi pF_r}{B}+\phi_{r,p,s}\right), \tag{5.21}$$

where also $F \gg B$ was used.

Magnetostriction can be measured along different crystal directions while keeping the direction of the magnetic field fixed. The oscillatory part of the magnetostriction then varies with the stress dependence of the cross-sections of the Fermi surface in the particular directions. By comparing measurements along main crystal directions, the anisotropy of the stress dependence of the Fermi surface can be deduced. To obtain absolute values of the stress dependence of the Fermi surface it is necessary to measure the oscillatory magnetization with the same phase and on the same crystal as the magnetostriction. This was not feasible with our experimental setup. Alternatively, when quantum oscillation data measured under hydrostatic pressure is available, the combined information yields the anisotropic stress dependence of the Fermi surface. Information on the anisotropy of the stress dependence of the Fermi surface is a feature of oscillatory magnetostriction that distinguishes this method from de Haas-van Alphen oscillations in the magnetization or magnetic torque, or Shubnikov-de Haas oscillations in the resistivity.

### 5.2.2 Oscillations

We measured the magnetostriction coefficients $\lambda_a$ and $\lambda_c$ of $KFe_2As_2$ [10, 14], $RbFe_2As_2$, and $CsFe_2As_2$ single crystals in magnetic fields $H \parallel a$ and $H \parallel c$ up to 14 T and for temperatures down to 50 mK. While for $RbFe_2As_2$ both $\lambda_a$ and $\lambda_c$ could be measured on the same sample, for $KFe_2As_2$ and $CsFe_2As_2$ $\lambda_a$ and $\lambda_c$ had to be measured

on different samples, called samples S1 and S2 respectively, because S1 was too thin for measurements of $\lambda_c$. This provides the opportunity to compare different samples of nominally the same compound made in different batches. Quantum oscillations were observed for all samples and field directions.

Figure 5.4 shows the oscillatory part of the magnetostriction coefficient $\lambda_a$ of $KFe_2As_2$, $RbFe_2As_2$, and $CsFe_2As_2$ for $H \parallel c$ at different temperatures. For $KFe_2As_2$ and $RbFe_2As_2$ quantum oscillations could be observed up to temperatures of 0.5 K, for $CsFe_2As_2$ up to 0.25 K.

Figure 5.5 shows the oscillatory part of the magnetostriction coefficient $\lambda_a$ of $KFe_2As_2$, $RbFe_2As_2$, and $CsFe_2As_2$ for $H \parallel a$ at different temperatures. For $KFe_2As_2$ quantum oscillations could be observed up to temperatures of 4 K, for $RbFe_2As_2$ up to 2.5 K, and for $CsFe_2As_2$ up to 1 K. The absence of modulations for $KFe_2As_2$ and $RbFe_2As_2$ shows that the spectrum contains only a single frequency. The beating observed for $CsFe_2As_2$ can be explained by field-dependent spin-splitting.

### 5.2.3 Spin splitting

A magnetic field introduces an energy difference between spin-up and spin-down quasiparticles of $g^*\mu_B B$ that leads to a phase difference in quantum oscillations. In case the effective $g$-factor $g^*$ deviates from two or the effective mass deviates from the free electron mass, this phase difference can be observed as a splitting of oscillation peaks. The amplitudes are reduced by the spin-splitting factor in the Lifshitz-Kosevich formula (see equation 5.17). In case the $g$-factor or the effective mass is changed by spin-orbit coupling or by many-body interactions, a splitting of the oscillation peaks can be observed and the amplitudes are reduced by the spin-splitting factor in the Lifshitz-Kosevich formula (see equation 5.17).

Figure 5.6 shows the oscillatory parts of the magnetostriction coefficients $\lambda_a$ and $\lambda_c$ of $KFe_2As_2$, $RbFe_2As_2$, and $CsFe_2As_2$ for $H \parallel a$ at $T = 50$ mK. A spin-splitting of the oscillation peaks is observed, especially pronounced in $\lambda_c$. The spin-splitting decreases with increasing inverse field, which means it increases with the magnetic field. In the series $KFe_2As_2$ to $RbFe_2As_2$ to $CsFe_2As_2$ the spin-splitting decreases. For $CsFe_2As_2$ it is only indirectly visible due to the beating that is caused by its field-dependence.

### 5.2.4 Mean free path

The Dingle factor $R_D$ in the Lifshitz-Kosevich formula allows the extraction of the mean free path under certain simplifying assumptions (see equation 5.16). When the quantity $\ln(aB^{1/2}R_T^{-1})$, where $a$ is the amplitude of the oscillation, and $R_T$ is the temperature factor (equation 5.14) is plotted against $1/B$ (see figure 5.8), the slope of the plot contains the inverse of the mean free path $l$ (see equation 5.16).

$$\ln\left(\frac{a\sqrt{B}}{R_T}\right) = -\pi p\sqrt{\frac{2\hbar}{e}}\frac{\sqrt{F}}{Bl}. \tag{5.22}$$

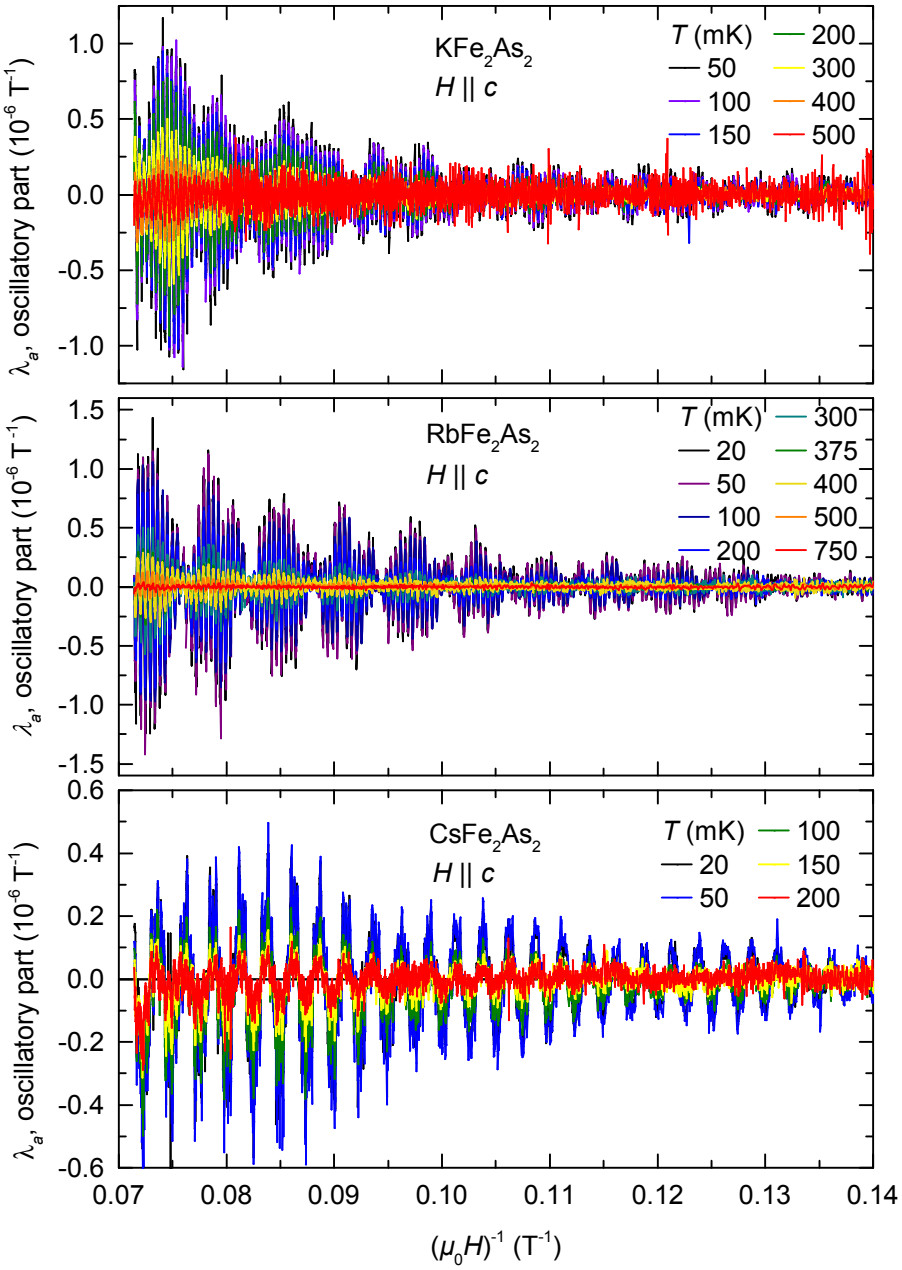


**Figure 5.4:** The oscillatory part of the magnetostriction coefficient $\lambda_a$ of $KFe_2As_2$, $RbFe_2As_2$, and $CsFe_2As_2$ for $H \parallel c$ at different temperatures.

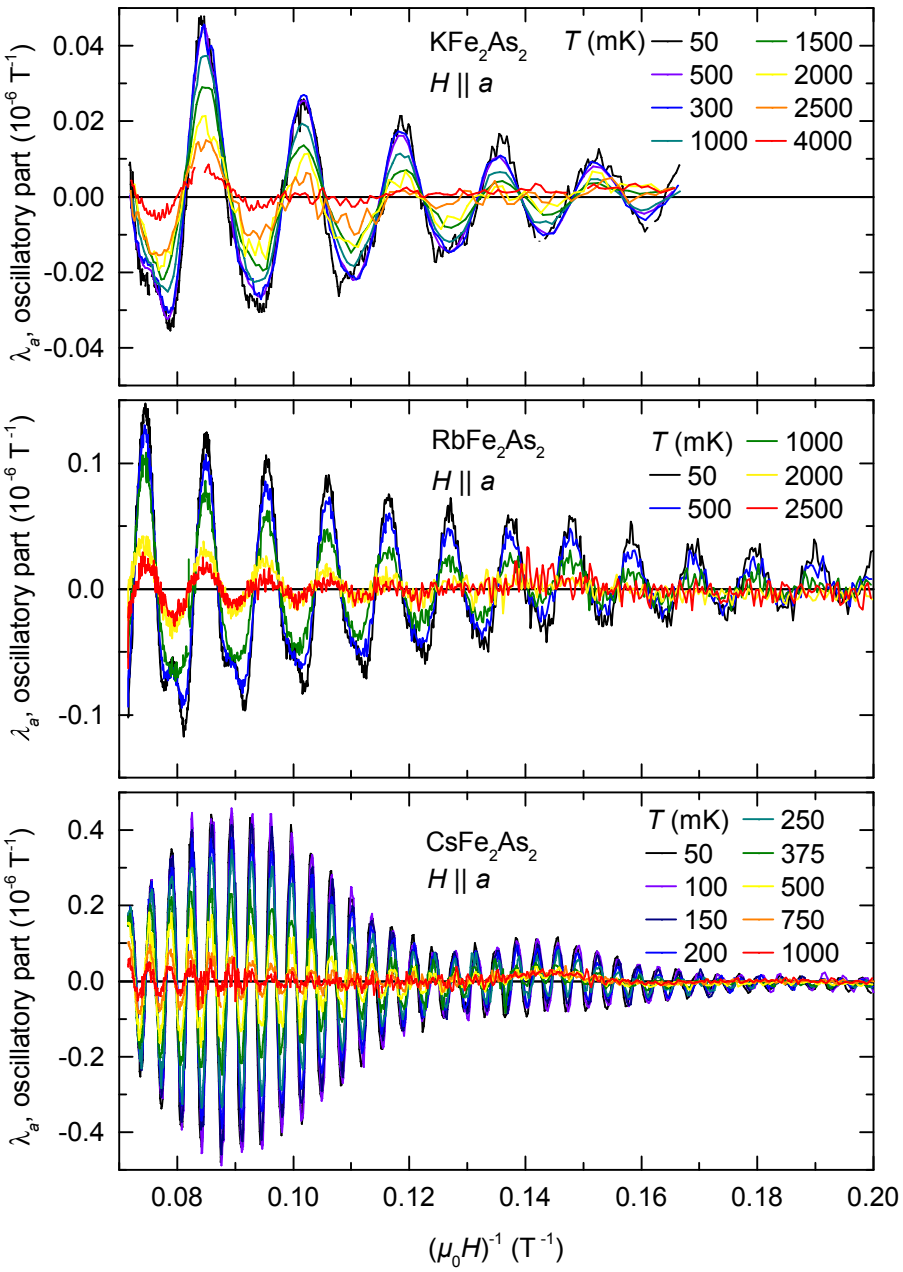


**Figure 5.5:** The oscillatory part of the magnetostriction coefficient $\lambda_a$ of $KFe_2As_2$, $RbFe_2As_2$, and $CsFe_2As_2$ for $H \parallel a$ at different temperatures. Oscillations with one single frequency are visible. The beatings observed for $CsFe_2As_2$ can be explained by field-dependent spin-splitting.

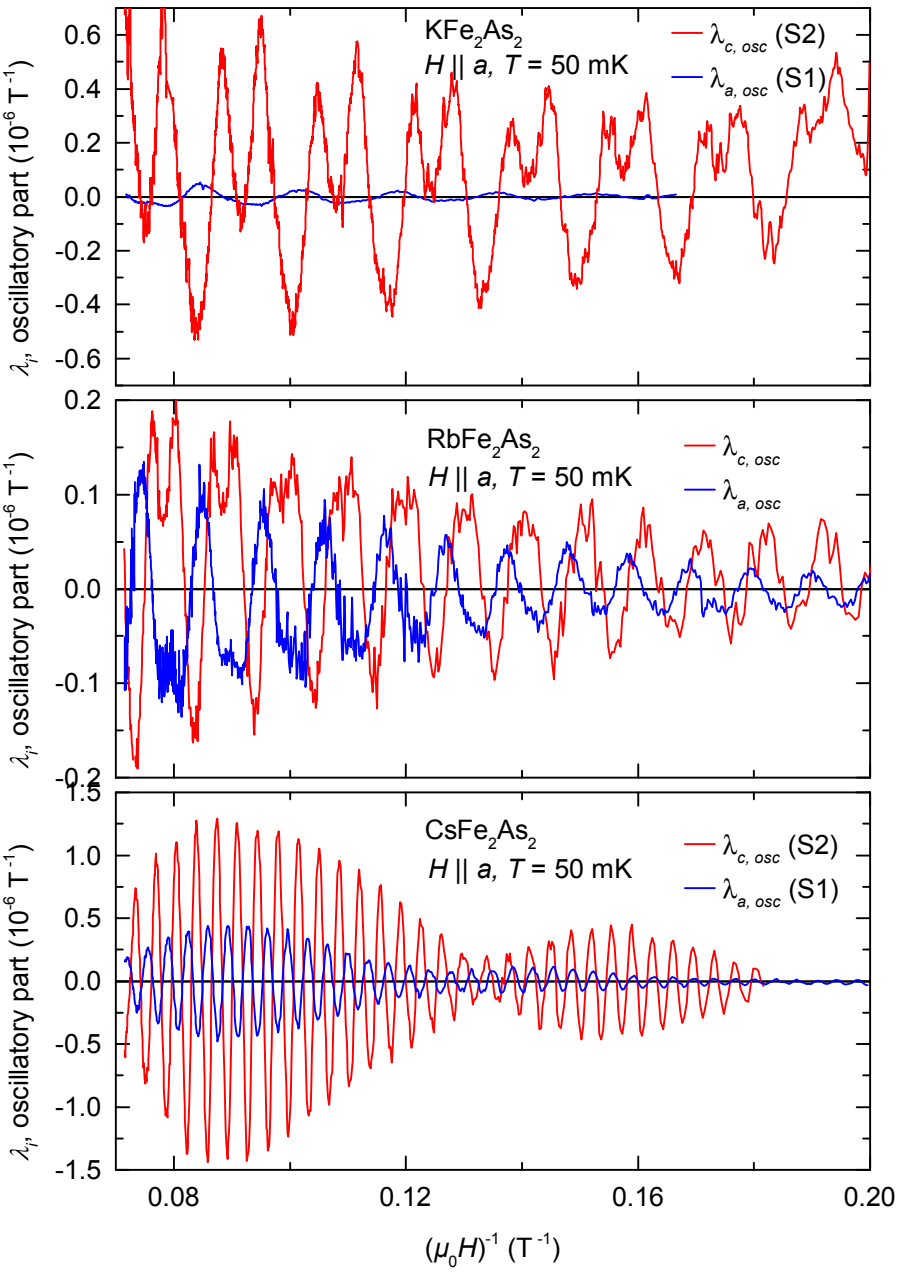


**Figure 5.6:** The oscillatory parts of the magnetostriction coefficients $\lambda_a$ and $\lambda_c$ of $KFe_2As_2$, $RbFe_2As_2$, and $CsFe_2As_2$ for $H \parallel a$ at $T = 50\,\mathrm{mK}$. The spin-splitting of the oscillation peaks decreases in the series. For $CsFe_2As_2$ it is only indirectly visible due to the beating.

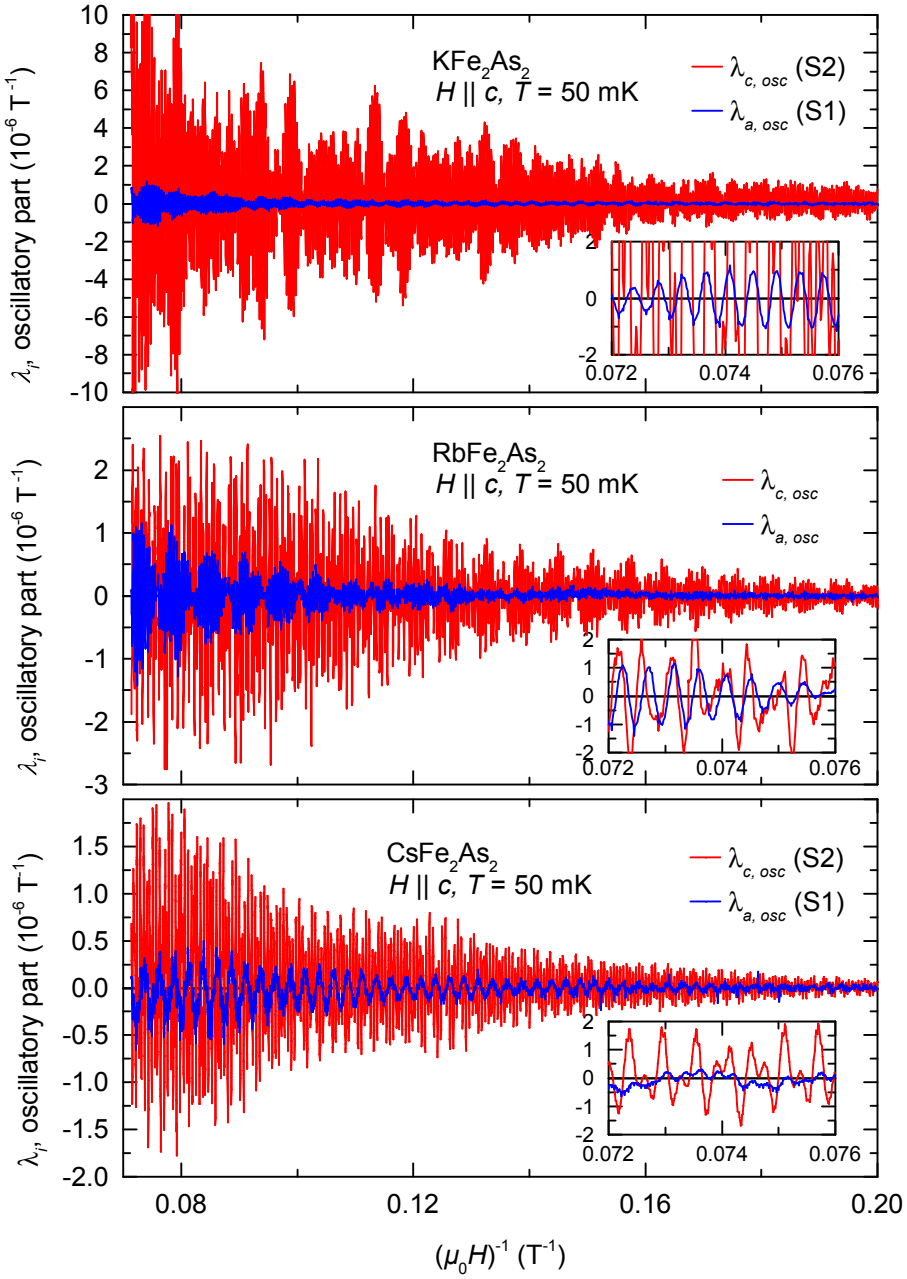


**Figure 5.7:** The oscillatory parts of the magnetostriction coefficients $\lambda_a$ and $\lambda_c$ of $KFe_2As_2$, $RbFe_2As_2$, and $CsFe_2As_2$ for $H \parallel c$ at $T = 50\,\mathrm{mK}$.

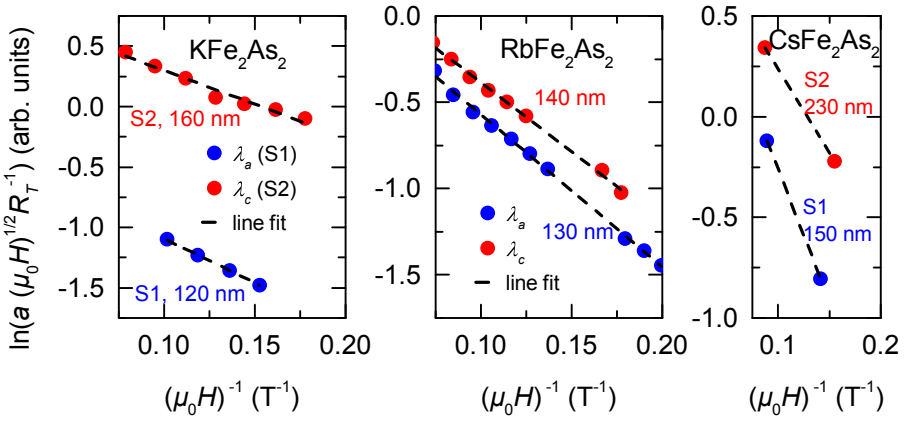


**Figure 5.8:** Plots used to determine the mean free path of the orbit observed for $H \parallel a$ (see equation 5.22). For $KFe_2As_2$ and $CsFe_2As_2$ sample 2 is purer than sample 1.

For $H \parallel a$ the amplitudes $a$ can be read directly from the plot of the quantum oscillations as a function of inverse field (fig. 5.6). For $CsFe_2As_2$ the spin-splitting is too small to be observed directly. It is only visible due to its field-dependence that causes the beatings. Since only two beating maxima are observed, only two points are available for the determination of the slope. Fortunately this is sufficient. The following mean free paths result from this analysis for the orbit observed for $H \parallel a$: For $KFe_2As_2$ $l \approx 120\,\mathrm{nm}$ for sample 1 and $l \approx 160\,\mathrm{nm}$ for sample 2. For $RbFe_2As_2$ $l \approx 130\,\mathrm{nm}$. For $CsFe_2As_2$ $l \approx 150\,\mathrm{nm}$ for sample 1 and $l \approx 230\,\mathrm{nm}$ for sample 2. This leads to the conclusion that both for $KFe_2As_2$ and $CsFe_2As_2$ sample 2 is purer than sample 1.

## 5.3 Fermi surfaces

### 5.3.1 Fermi surfaces of iron-based superconductors

The Fermi surfaces of iron-based superconductors consist of up to five sheets, depending on the number of $d$-electron or hole bands that cross the Fermi energy. The prominent structural elements are iron arsenic layers that are stacked along the crystallographic $c$-direction and separated by other structural elements. Due to this anisotropy, common features of the Fermi surface include more or less distorted tubes with axes parallel to $c$.

Before discussing Fermi surfaces in detail, a clarification of notation regarding reciprocal space is in order to avoid confusion. For an extensive review of this issue see Ref. [3]. The '11', '111', and '1111' compounds with space group $P4/nmm$ have a primitive tetragonal (pt) unit cell containing one FeAs layer. The conventional translational vectors of the reciprocal lattice $\boldsymbol{k}_x, \boldsymbol{k}_y, \boldsymbol{k}_z$ are parallel to their respective conventional translational vectors of the direct lattice $\boldsymbol{a}, \boldsymbol{b}, \boldsymbol{c}$. The '122' compounds

with space group $I4/mmm$ have a conventional body-centered tetragonal (bct) unit cell containing two FeAs layers. The reciprocal lattice is again body-centered tetragonal, but the conventional translational vectors of the reciprocal lattice $\boldsymbol{k}_x, \boldsymbol{k}_y$ are at angles of 45° to the conventional vectors of the direct lattice $\boldsymbol{a}, \boldsymbol{b}$. See figure 5.9 for depictions of the two Brillouin zones.

Regarding notation of the points in the first BZ, there is never confusion with the Γ point, which denotes the center of the BZ. The $M$ point in the pt BZ and the $X$ point in the bct BZ refer to the same position in reciprocal space with respect to the conventional tetragonal direct lattice. The top center of the BZ is referred to as $Z$ point in the pt BZ and as $M$ point in the bct BZ. The distance from the center to the top center is $\pi/c$ in the pt BZ and $2\pi/c$ in the bct BZ.

In some calculations not the pt or bct unit cell are used, but only a square with iron atoms at its corners, approximating the FeAs layers with only one Fe atom per unit cell. The respective BZ is called 'unfolded' BZ. Compared to the conventional BZ, which is called 'folded' BZ, it is rotated by 45° and larger by a factor of $\sqrt{2}$. The $X$ point in the 'unfolded' BZ denotes the same point in reciprocal space as the $M$ point in the 'folded' pt BZ and the $X$ point in the 'folded' bct BZ.

Some compounds (e.g., FeSe, LaFeAsO, Ca,Sr,Ba-122) undergo a structural phase transition at low temperatures and become orthorhombic (e.g., space group $Cmma$ for '1111', $Fmmm$ for '122'). This brings about further complications in notation.

As a special service to the reader I will refer to points in reciprocal space not by $M$, $X$, or $Z$ but by $\boldsymbol{Q}$-vectors in conventional reciprocal lattice units $(2\pi/a, 2\pi/a, 2\pi/c)$. Using the center of the Brillouin zone as the origin $(0, 0, 0)$, the unit vectors point along the conventional tetragonal, crystallographic $a$, $b$, and $c$ axes, respectively. In this notation the corner of the BZ is $\boldsymbol{Q} = (0.5, 0.5, 0)$ and the top center of the BZ is $\boldsymbol{Q} = (0, 0, 0.5)$ for pt systems and $\boldsymbol{Q} = (0, 0, 1)$ for bct systems.

In LiFeAs [59], LaFeAsO [60], $CaFe_2As_2$ [61], $SrFe_2As_2$ [62], and $BaFe_2As_2$ [63] the Fermi surface consists of two to three distorted hole cylinders or pockets centered at $\boldsymbol{Q} = (0, 0, q_z)$ and two distorted electron cylinders centered at $\boldsymbol{Q} = (0.5, 0.5, q_z)$.

In the $Ba_{1-x}K_xFe_2As_2$ series the Fermi surface develops with hole doping in the following way (see figures 5.10, 5.11): The cross-sections of the distorted hole cylinders centered at $\boldsymbol{Q} = (0, 0, q_z)$ grow continuously [64]. At the same time so-called 'propellers' develop at $\boldsymbol{Q} = (0.5, 0.5, q_z)$ [65, 66]. The 'hub' of the 'propeller' is an electron-like feature of the Fermi surface centered directly at $\boldsymbol{Q} = (0.5, 0.5, q_z)$. The four 'blades' of the 'propeller' are hole-like features and are located close to the 'hub'. Alternatively, a botanic picture can be used to describe these Fermi surface sheets as 'flowers' with a 'stem' and four 'petals'. At a composition of $x = 0.5$ to $x = 0.6$ the electron-like 'hubs' shift above the Fermi energy and only the blades remain [67–69]. $KFe_2As_2$ has exclusively hole bands. Its Fermi surface consists of three warped hole cylinders centered at $\boldsymbol{Q} = (0, 0, q_z)$ and one warped hole cylinder close to every four of the points equivalent to $\boldsymbol{Q} = (0.5, 0.5, q_z)$ [13], as well as a small hole pocket at $\boldsymbol{Q} = (0, 0, 1)$ [14]. DFT calculations performed by Heid (IFP) and Ikeda [70] predict very similar Fermi surfaces for $RbFe_2As_2$ and $CsFe_2As_2$ (figure 5.12). This work provides first experimental confirmation of this prediction.

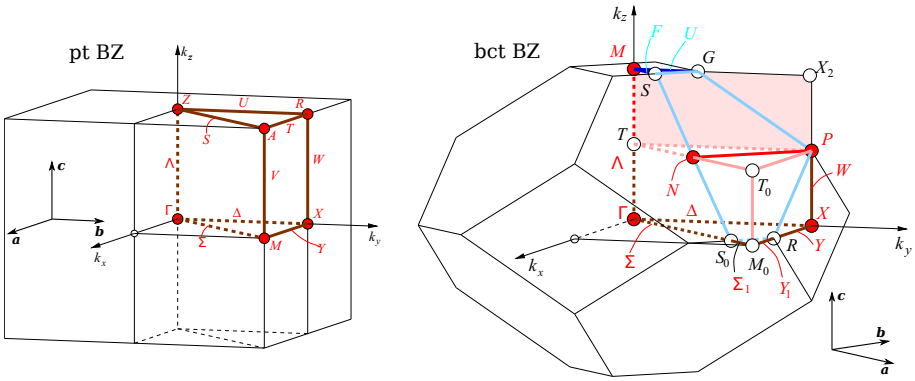


**Figure 5.9:** First Brillouin zones (BZ) of the primitive tetragonal (pt) lattice (left) and the body centered tetragonal (bct) lattice (right) for $c > a$. Taken from the Bilbao Crystallographic Server [71]. Note the different orientations of the depicted BZ with respect to the conventional direction in the direct lattice $\boldsymbol{a}$.

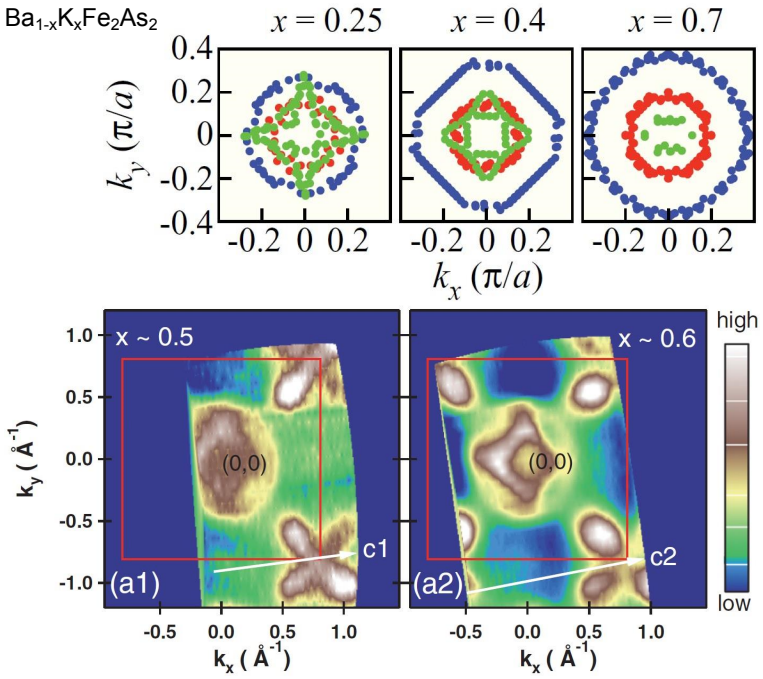


**Figure 5.10:** Top panels: Fermi surface cuts of $Ba_{1-x}K_xFe_2As_2$, $x = 0.25, 0.4, 0.7$ at $\boldsymbol{Q} = (q_x, q_y, 0)$ obtained by ARPES by Nakayama *et al.* [64]. Blue and red: Cylinders centered at $\boldsymbol{Q} = (0, 0, 0)$. Green: Fermi surface sheets centered at $\boldsymbol{Q} = (0.5, 0.5, 0)$, but plotted at $\boldsymbol{Q} = (0, 0, 0)$ in these figures. Bottom panels: ARPES intensity maps of $Ba_{1-x}K_xFe_2As_2$, $x = 0.5$ (left) and $x = 0.6$ (right) measured by Malaeb *et al.* [67].

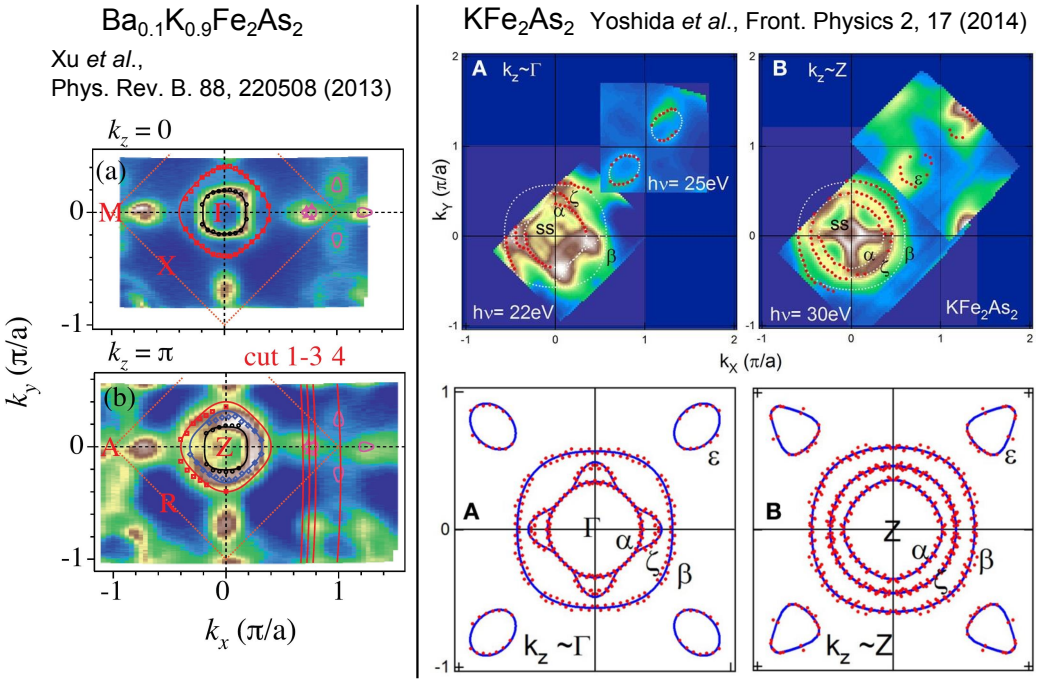


**Figure 5.11:** Left panels: ARPES intensity maps of $Ba_{0.1}K_{0.9}Fe_2As_2$ at the Fermi energy for (a) $\boldsymbol{Q} = (q_x, q_y, 0)$, (b) $\boldsymbol{Q} = (q_x, q_y, 1)$ measured by Xu *et al.* [68]. Special emphasis is on the occurrence of hole cylinders close to $\boldsymbol{Q} = (0.5, 0.5, q_z)$ and the absence of electron cylinders directly at $\boldsymbol{Q} = (0.5, 0.5, q_z)$. Top right panels: ARPES intensity maps of $KFe_2As_2$ at the Fermi energy for (A) approximately $\boldsymbol{Q} = (q_x, q_y, 0)$, (B) approximately $\boldsymbol{Q} = (q_x, q_y, 1)$, where $-0.5 \leq q_{x,y} \leq 1.0$ measured by Yoshida *et al.* [13]. Below: Fermi surface cuts.

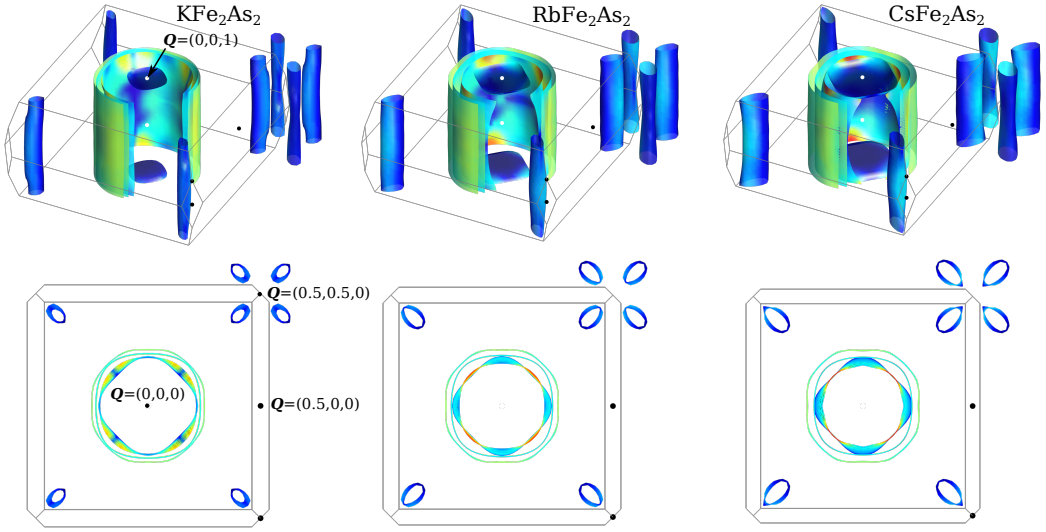


**Figure 5.12:** Fermi surfaces of $KFe_2As_2$, $RbFe_2As_2$, and $CsFe_2As_2$ as calculated by Ikeda [70] using density functional theory. The size of the 'propeller blades' or 'flower petals' around $\boldsymbol{Q} = (0.5, 0.5, q_z)$ is predicted to grow in the series, as well as the pocket at $\boldsymbol{Q} = (0, 0, 1)$.

### 5.3.2 Fermi surface cross-sections

Extremal cross-sections of the Fermi surface $A$ can be extracted directly from the frequencies $F$ of quantum oscillations via the Onsager relation [53]

$$A = \frac{2\pi e}{\hbar} \cdot F. \tag{5.23}$$

The frequencies, in turn, are obtained by means of a Fourier transform. In order to compute the Fourier transform, first a polynomial of low order was subtracted from the measured magnetostriction coefficient, thus extracting its oscillatory part. The oscillatory part of the magnetostriction coefficient as a function of inverse magnetic field was then linearly interpolated to obtain evenly spaced data points. Finally, the fast Fourier transform (FFT) was computed in a certain range of inverse magnetic field. In addition to the frequencies $F$, the FFT also delivers the amplitude and the phase for every frequency.

The minimum resolvable frequency difference, or the frequency resolution $\Delta F$, is given by the inverse of the range of inverse magnetic fields.

$$\Delta F = \left( \frac{1}{\mu_0 H_{min}} - \frac{1}{\mu_0 H_{max}} \right)^{-1} \tag{5.24}$$

For example, for $H_{min} = 2\,\mathrm{T}$ and $H_{max} = 14\,\mathrm{T}$ the frequency resolution is $\Delta F = 2.33\,\mathrm{T}$, while for $H_{min} = 7\,\mathrm{T}$ and $H_{max} = 14\,\mathrm{T}$ it is $\Delta F = 14.0\,\mathrm{T}$ (see figure 5.13). The maximum resolvable frequency $F_{max}$ (called Nyquist frequency) is determined

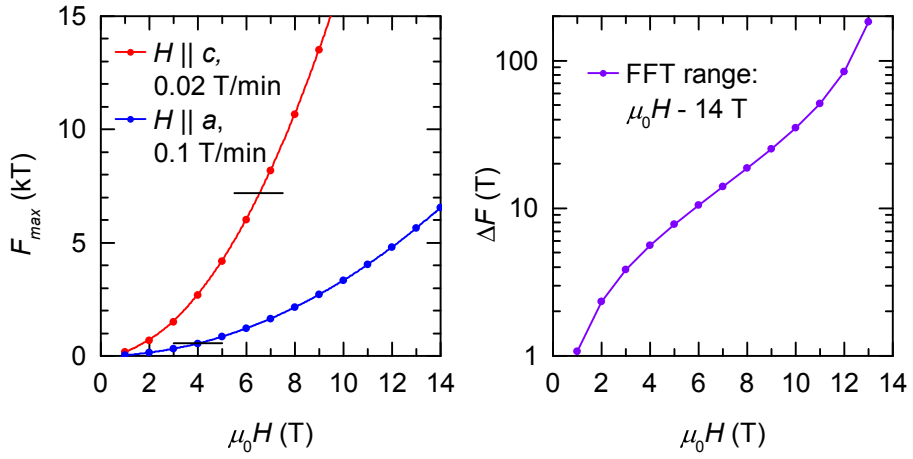


**Figure 5.13:** Left: Maximum resolvable frequency for the parameters used in the measurements of the magnetostriction. Maximum observed frequencies are indicated by black horizontal lines. Right: Frequency resolution for different ranges of inverse magnetic field used in the Fourier transform.

by the sampling interval $\Delta(1/\mu_0 H)$:

$$F_{max} = \frac{1}{2\Delta\left(\frac{1}{\mu_0 H}\right)}. \tag{5.25}$$

Quantum oscillations in the magnetostriction were measured with a constant ramp rate of the magnetic field $r = 0.02\,\mathrm{T/min}$ for $H \parallel c$ and $r = 0.1\,\mathrm{T/min}$ for $H \parallel a$, taking averages of the capacitance over a fixed time interval $\Delta t = 9\,\mathrm{s}$. Therefore, the sampling interval in the inverse magnetic field $\Delta(1/\mu_0 H)$ is smaller at higher fields

$$\Delta\left(\frac{1}{\mu_0 H}\right) = \frac{r}{(\mu_0 H)^2}\Delta t \tag{5.26}$$

and accordingly the maximum resolvable frequency $F_{max}$ is larger at higher magnetic fields (see figure 5.13). In total there are three contributions that determine the dependence of the amplitudes on the range of inverse magnetic fiels chosen for the Fourier transform: Apart from the magnetic field dependence described by the Dingle factor $R_D$ (equation 5.15) and other field-dependent quantities contained in the amplitudes, there are the field-dependence of the maximum resolvable frequency $F_{max}$ and the range-dependence of the frequency resolution $\Delta F$. In order to extract information on observable frequencies and amplitudes, Fourier spectra with different field ranges were compared.

Figure 5.14 shows the Fourier spectra of the oscillatory parts of the magnetostriction coefficients $\lambda_a$ and $\lambda_c$ of $KFe_2As_2$, $RbFe_2As_2$, and $CsFe_2As_2$ at $T = 50\,\mathrm{mK}$ for $H \parallel c$ and $H \parallel a$. The inverse field ranges for the FFT were chosen as large as possible to obtain the best possible frequency resolution. For $H \parallel a$ only one small

frequency and its harmonics below $\sim 0.6\,\mathrm{kT}$ were observed. For $H \parallel c$ a multitude of frequencies were observed, and for the identification of single frequencies a number of specific frequency ranges will be discussed in the following. The position of fundamental frequencies are marked by thick, black vertical lines in the figures. Expected positions of second and third harmonics are marked by thinner vertical lines. The assignment of frequencies to Fermi surface features for $RbFe_2As_2$ and $CsFe_2As_2$ was based on the assignment of frequencies for $KFe_2As_2$ made by Terashima *et al.* [12] on the basis of angle-dependent dHvA measurements. Therefore, the following notation, which was established by previous work on $KFe_2As_2$ [72], is used in some figures: $\epsilon_l$ and $\epsilon_h$ denote the lower ($l$) and the higher ($h$) frequency, respectively, assigned to the hole tubes in the corner of the Brillouin zone, $\alpha_l$ and $\alpha_h$ the inner tube at the center of the BZ, $\zeta_l$ and $\zeta_h$ the middle tube, and $\beta$ the outer tube.

Figure 5.15 shows the low-frequency part of the Fourier spectra for $H \parallel c$. Two distinct frequencies, and for $KFe_2As_2$ also their higher harmonics, can be identified. Following the work of Terashima *et al.* [12] on $KFe_2As_2$, these frequencies are assigned to the hole tubes in the corner of the BZ. Apparently, the tubes have two extremal cross-sections, but from quantum oscillation data alone it can not be decided at which $q_z$ in the Brillouin zone the larger and the smaller cross-section lie. According to both LDA calculations by Ikeda (see figure 5.12) and LDA+DMFT calculations on $KFe_2As_2$ by Backes [73], the larger cross-section is located at $q_z = 0$ and the smaller one at $q_z = 1$. In ARPES data on $KFe_2As_2$ by Yoshida *et al.* [13] the tubes appear roughly twice as big and no difference in cross-section is seen at these $q_z$. As becomes evident from the data shown in figure 5.15, in the series $KFe_2As_2$ to $RbFe_2As_2$ to $CsFe_2As_2$ the average cross-section of the tube increases, while the difference between minimum and maximum cross-sections (the warping) decreases.

Figure 5.16 shows the frequency range of the Fourier spectra associated with the inner hole tube. In the series $KFe_2As_2$ to $RbFe_2As_2$ to $CsFe_2As_2$ the average cross-section of the tube decreases, while the difference between minimum and maximum cross-sections (the warping) increases. For $KFe_2As_2$ a series of frequencies associated with magnetic breakdown orbits is visible. They are discussed in subsection 5.3.3.

Figure 5.17 shows the frequency range associated with the middle hole tube. In line with angle-dependent dHvA measurements by Terashima *et al.* [12], two frequencies that lie wide apart are observed for $KFe_2As_2$. The lower frequency is assigned to a large part of the middle tube with a smaller cross-section around the center of the BZ, and the higher frequency to a small part of the middle tube at the top of the BZ [12]. For $RbFe_2As_2$ and $CsFe_2As_2$ a corresponding larger frequency above $4\,\mathrm{kT}$ is not observed (figure 5.17). Instead, the smaller frequency increases and its amplitude peak splits. Either the middle tubes of $RbFe_2As_2$ and $CsFe_2As_2$ have very small warping or they still have large warping but the larger frequency is not observed in our data and there are three extremal cross-sections. It is unlikely that the appreciable splitting would be caused by a small misalignment(below $2^\circ$) of the crystal $c$-axis with respect to $H$. Assuming that the frequency pair at the lower frequency constitutes all extremal cross-sections of the middle tube, already a hole count of $25\,\%$ is reached, as for $KFe_2As_2$ without the outer tube (see subsection

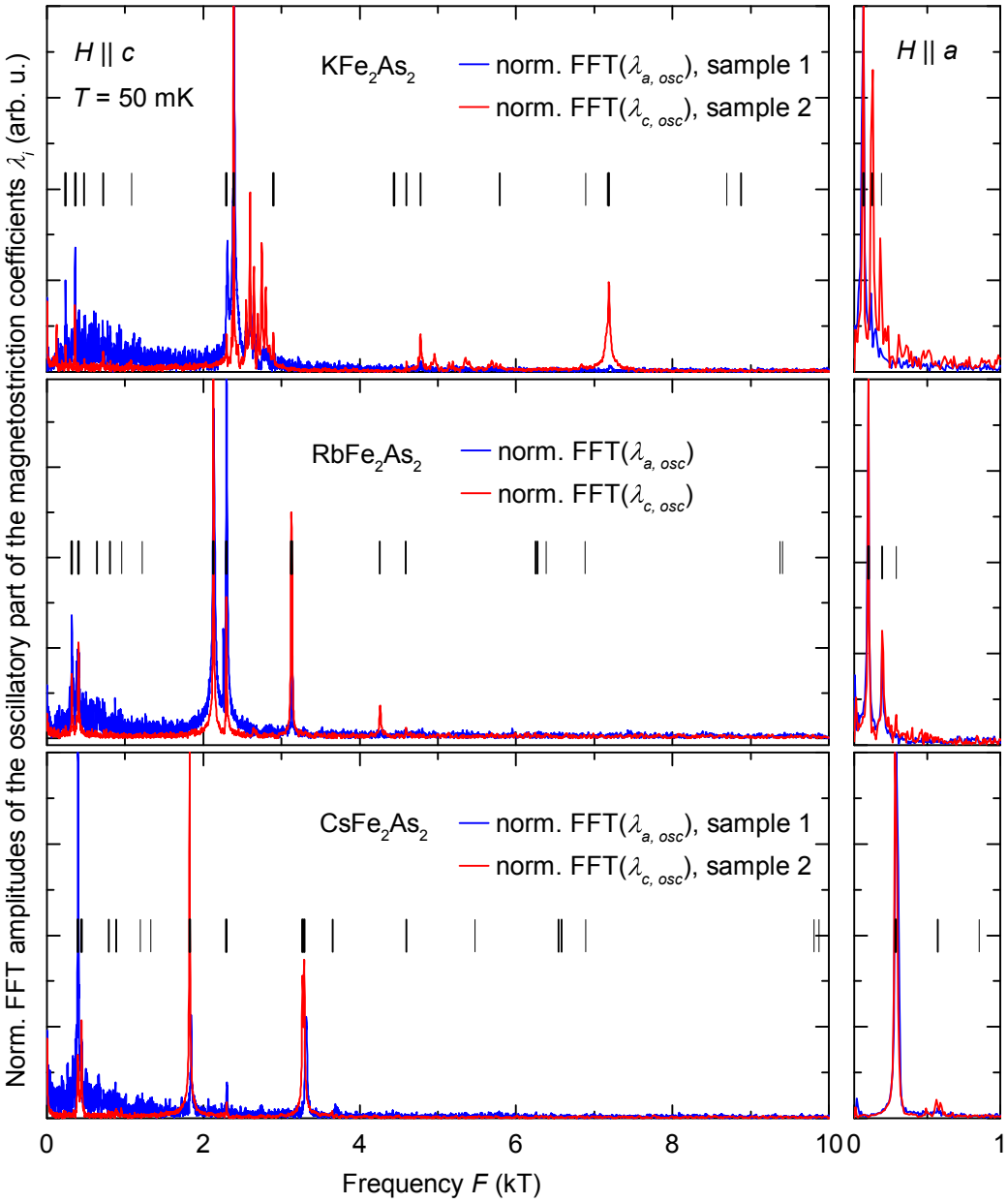


**Figure 5.14:** Fourier spectra of the oscillatory parts of the magnetostriction coefficients $\lambda_a$ and $\lambda_c$ of $KFe_2As_2$, $RbFe_2As_2$, and $CsFe_2As_2$ at $T = 50\,\mathrm{mK}$ for $H \parallel c$ (left) and $H \parallel a$ (right). Field ranges chosen for the FFT are $2 - 14\,\mathrm{T}$ for $H \parallel c$ and $6 - 14\,\mathrm{T}$, $4.2 - 14\,\mathrm{T}$, and $5.5 - 14\,\mathrm{T}$ for $KFe_2As_2$, $RbFe_2As_2$, and $CsFe_2As_2$, respectively, for $H \parallel a$. Fundamental frequencies are marked by thick, black, vertical lines and expected frequencies of second and third harmonics are marked by thinner vertical lines

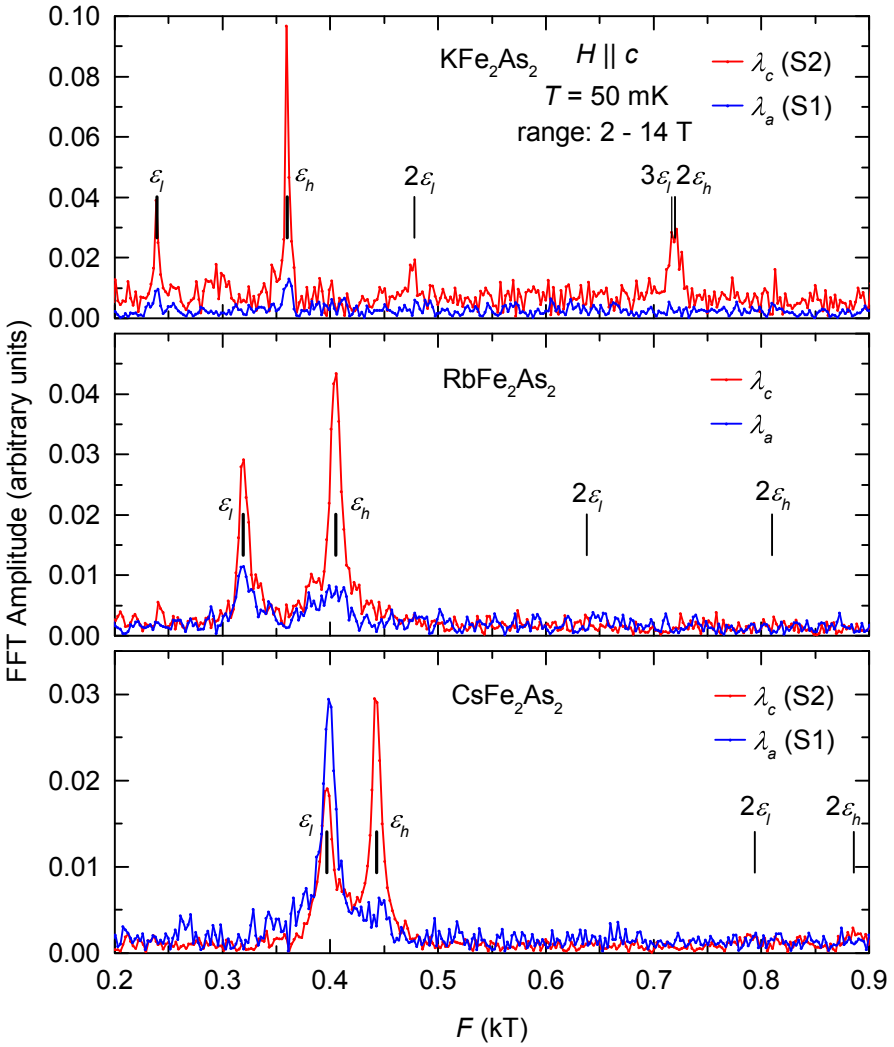


**Figure 5.15:** Low-frequency part of the Fourier spectra of the oscillatory part of the magnetostriction coefficient for $H \parallel c$ at $T = 50\,\mathrm{mK}$. Fundamental frequencies associated with the hole tubes in the corner of the Brillouin zone ($\epsilon_l$ and $\epsilon_h$) are marked by thick, black, vertical lines. Expected frequencies of second and third harmonics are marked by thinner vertical lines. In the series $KFe_2As_2$ to $RbFe_2As_2$ to $CsFe_2As_2$ the size of the tube increases, while the warping decreases.

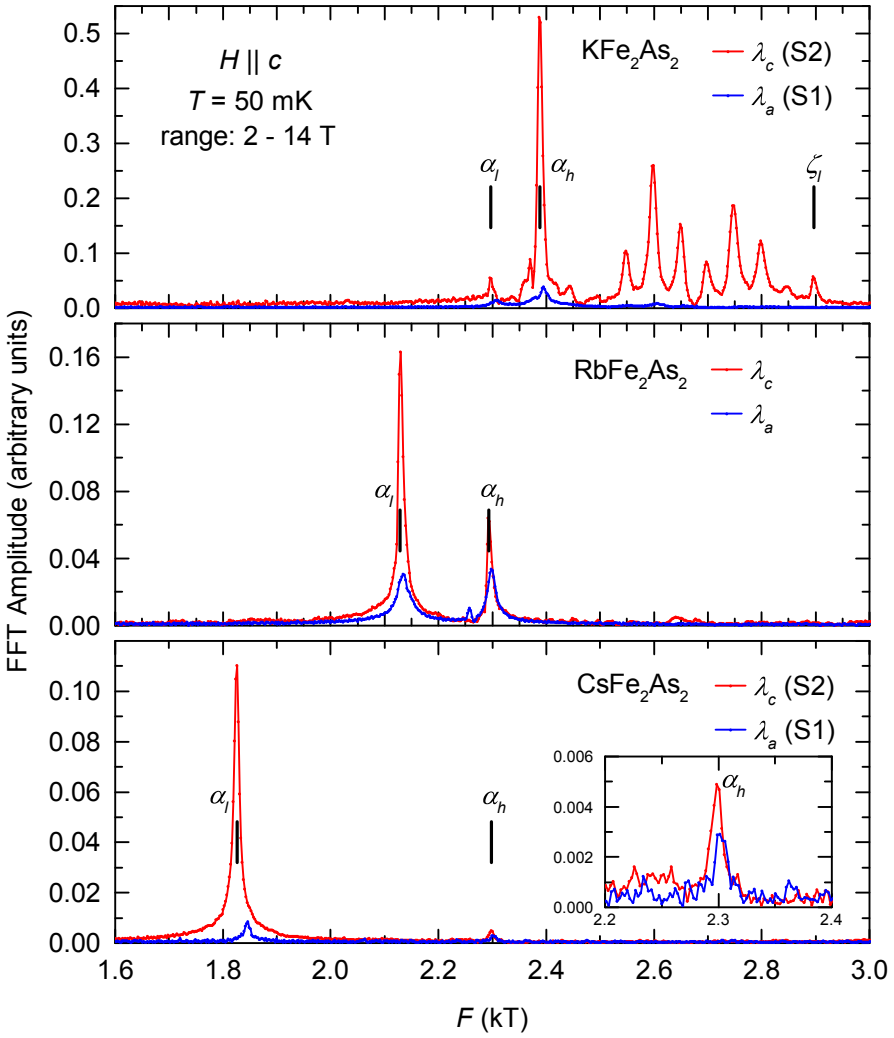


**Figure 5.16:** Fourier frequencies associated with the inner hole tube in the center of the BZ ($\alpha_l$ and $\alpha_h$). In the series $KFe_2As_2$ to $RbFe_2As_2$ to $CsFe_2As_2$ the size of the tube decreases, while the warping increases. For $KFe_2As_2$ a series of frequencies associated with magnetic breakdown orbits is visible (see section 5.3.3).

5.3.4). Therefore, the frequency pair is interpreted as the complete representation of a middle hole tube with very small warping.

Figure 5.18 shows the frequency range associated with the outer hole tube. For $KFe_2As_2$ the frequency belonging to the outer tube is very close to the third harmonic of a well pronounced frequency of the inner tube, as already noted by Terashima *et al.* [12]. This explains the shoulder on the left-hand side of the peak. Quite possibly, there is also a second peak associated with the outer tube buried in the wide foot of the peak. For $Ba_{0.07}K_{0.93}Fe_2As_2$ Terashima *et al.* [12] observed a clear, albeit small splitting of 0.08 kT of the corresponding peak. This can be interpreted as a very small warping of the outer tube [12]. Also for $KFe_2As_2$ a small warping is expected, since the hole count already reaches the expected 50 % with the observed peak (see subsection 5.3.4). Thus no further frequency is expected to appear.

For $RbFe_2As_2$ and $CsFe_2As_2$ no peak exceeds the noise level in this frequency region. One reason for the absence of a frequency associated with the outer tube in our data is impurity scattering (see equation 5.16). Larger extremal cross-sections of the Fermi surface imply a larger orbit in real space. For the same mean free path, impurity scattering suppresses larger orbits more strongly than smaller ones. Therefore, the orbit might be observed in purer crystals with less impurity scattering or in higher magnetic fields where the orbits in real space are smaller. Another reason for the absence might be the high effective mass (see equation 5.14). In that case lower temperatures would be beneficial.

Figure 5.19 shows the Fourier spectra for $H \parallel a$. Only small frequencies and their harmonics can be seen. They are associated with the small hole pockets at the top of the BZ. In the series $KFe_2As_2$ to $RbFe_2As_2$ to $CsFe_2As_2$ the size of the pocket increases. For $H \parallel c$ they are not seen, probably because of the large curvature at the extremal cross-section (see equation 5.13).

All detected frequencies are listed in table 5.3.2.

### 5.3.3 Magnetic breakdown orbits in $KFe_2As_2$

A multitude of equally spaced frequencies between 2.3 kT and 2.9 kT, and their second harmonics between 4.6 kT and 5.8 kT, are observed for $KFe_2As_2$ in a magnetic field $H \parallel c$, as already mentioned above (figure 5.16). They are shown in figure 5.20 on an enlarged scale. These frequencies can be ascribed to so-called magnetic breakdown orbits between the inner and the middle hole tube with frequencies 2.3 kT and 2.9 kT, respectively [12]. When two Fermi surfaces are very close to each other, a high magnetic field can lead to tunneling of quasiparticles between orbits on different Fermi surfaces separated by a small energy gap $\epsilon_g$. This effect is called magnetic breakdown. The condition for it to occur is that the separation between the Landau levels $\hbar\omega_c$ must be [53]

$$\hbar\omega_c \gtrsim \frac{\epsilon_g^2}{E_\mathrm{F}}. \tag{5.27}$$

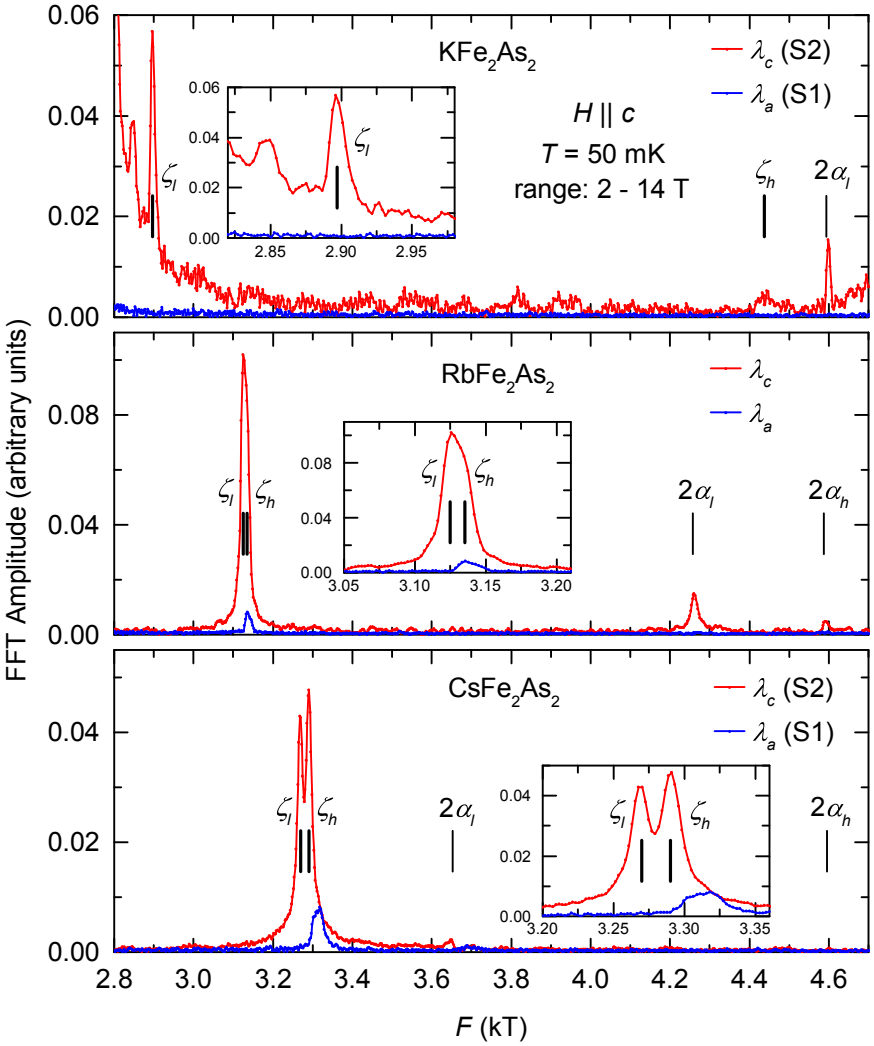


**Figure 5.17:** Fourier frequencies associated with the middle hole tube in the center of the BZ ($\zeta_l$ and $\zeta_h$). For $KFe_2As_2$ frequencies corresponding to a minimum and a maximum cross-section are observed [12]. For $RbFe_2As_2$ and $CsFe_2As_2$ a frequency above 4 kT is not observed. Instead the lower frequency splits, pointing to much smaller warping. In the series $KFe_2As_2$ to $RbFe_2As_2$ to $CsFe_2As_2$ the size of the tube grows.

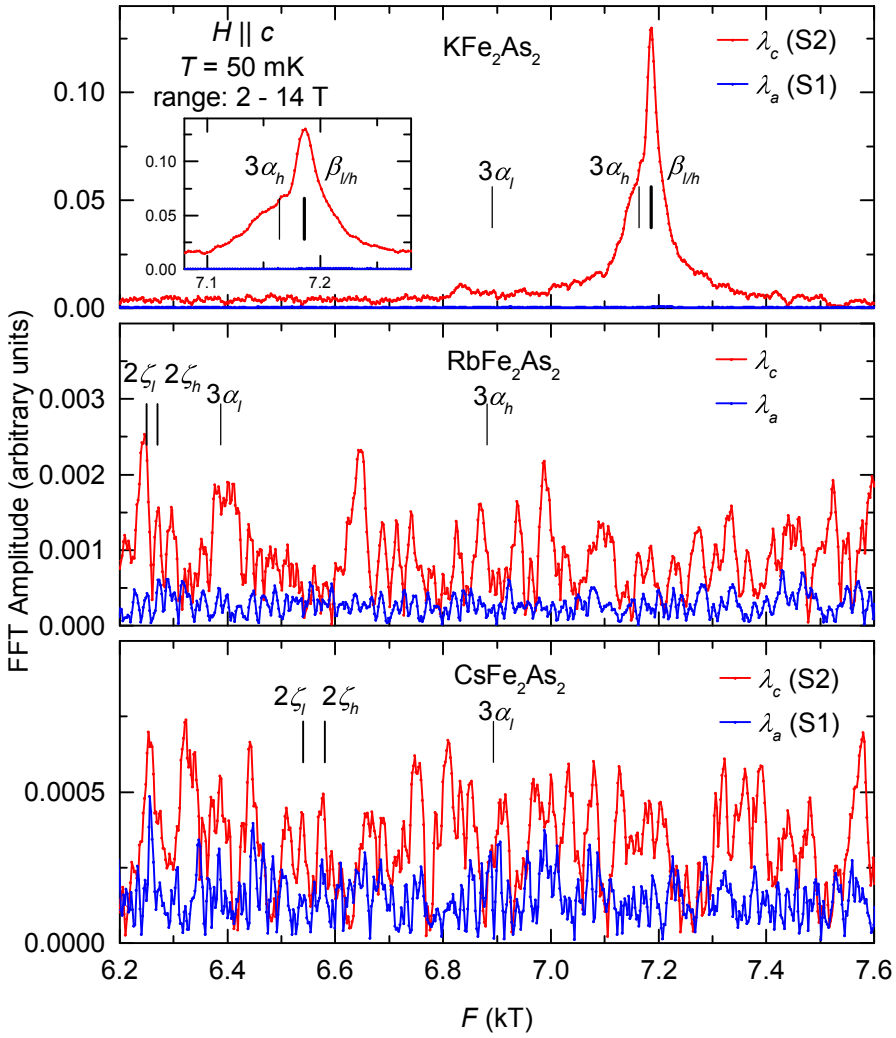


**Figure 5.18:** Fourier frequencies associated with the outer hole tube in the center of the BZ ($\beta$). For $KFe_2As_2$ the frequency belonging to the outer tube is very close to the third harmonic of a well pronounced frequency of the inner tube ($3\alpha_h$) [12]. For $RbFe_2As_2$ and $CsFe_2As_2$ no peak exceeds the noise level in this frequency region.

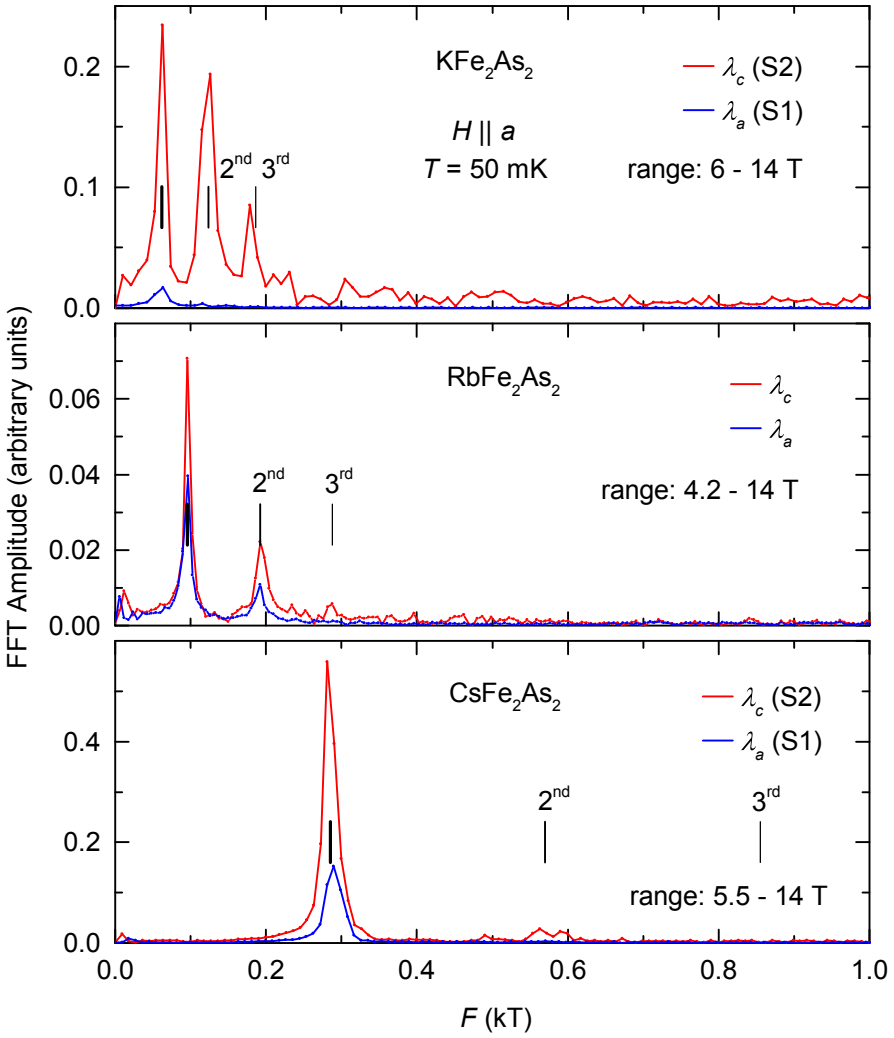


**Figure 5.19:** Fourier frequencies associated with the hole pockets at the top of the BZ, marked by black vertical lines. Expected positions of second and third harmonics are marked by thinner black, vertical lines. In the series $KFe_2As_2$ to $RbFe_2As_2$ to $CsFe_2As_2$ the size of the pocket increases.

**Table 5.1:** The Fourier frequencies extracted from quantum oscillations in the magnetostriction coefficient $\lambda$ of $KbFe_2As_2$, $RbFe_2As_2$, and $CsFe_2As_2$ for $H \parallel c$ and $H \parallel a$. The data for $KbFe_2As_2$ [10] compare well with the dHvA measurements of Terashima *et al.* [12].

| | | Fourier frequencies $F$ (kT) | | | |
|---|---|---|---|---|---|
| | Fermi | $KFe_2As_2$ | | $RbFe_2As_2$ | $CsFe_2As_2$ |
| | surface | dHvA[12] | $\lambda$[10] | $\lambda$ | $\lambda$ |
| $H \parallel c$ | corner | 0.24 | 0.24 | 0.32 | 0.40 |
| | corner | 0.36 | 0.36 | 0.41 | 0.44 |
| | inner | 2.30 | 2.30 | 2.13 | 1.83 |
| | inner | 2.39 | 2.39 | 2.29 | 2.30 |
| | middle | 2.89 | 2.90 | 3.13 | 3.27 |
| | middle | 4.40 | 4.44 | 3.14 | 3.29 |
| | outer | 7.16 | 7.19 | - | - |
| $H \parallel a$ | top center | - | 0.062 | 0.096 | 0.29 |

In the case of $KFe_2As_2$, the inner and the middle hole tube are sufficiently close to each other at certain points in reciprocal space that magnetic breakdown occurs already at moderate magnetic fields. ARPES measurements [13] (see figure 5.11) and LDA+DMFT calculations [73] suggest that magnetic breakdown is possible at eight points where the inner and the middle hole tubes are especially close. The frequencies of the breakdown orbits can be explained assuming a certain number of disconnected areas between the inner and the middle tube [12]: four areas $A_1$ and four areas $A_2$, where $A1 = 2A_2$, so that $A_{middle} = A_{inner} + 12A_2$ and the frequency corresponding to $A_2$ is 50 T (see figure 5.21).

For $RbFe_2As_2$ only two small amplitudes at approximately 2.25 kT and 2.65 kT surmount the noise level that could be signs of magnetic breakdown (figure 5.16). For $CsFe_2As_2$ no such frequencies are detected. The feeble occurrence or absence of frequencies associated with magnetic breakdown in $RbFe_2As_2$ and $CsFe_2As_2$ reveals a larger distance of their respective Fermi surfaces in reciprocal space.

### 5.3.4 Hole count and size of outer hole tubes

The number of states enclosed by the Fermi surface is the electron or hole count, that is the number of electrons or holes in partially occupied bands. Luttinger's theorem states that interactions between fermions do not affect the Fermi volume, or the total number of occupied states. Thus, also in a correlated electron system forming a Fermi liquid, the electron or hole count $N$ is given by the ratio of the Fermi volume $V_\mathrm{F}$ and the volume of one state in reciprocal space $V_{1k}$:

$$N = \frac{V_\mathrm{F}}{V_{1k}} = 2V_\mathrm{F}\frac{V}{(2\pi)^3}, \tag{5.28}$$

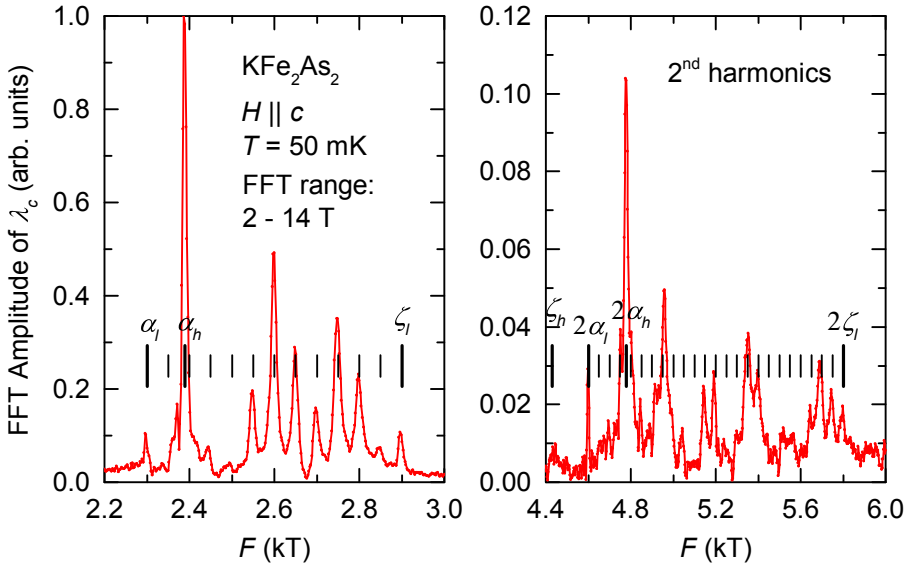


**Figure 5.20:** Frequencies associated with magnetic breakdown orbits between the inner (2.3 kT) and the middle (2.9 kT) hole tube of $KFe_2As_2$. Left: The distance of frequencies resulting from magnetic breakdown (indicated by small vertical lines) is 0.05 kT. Right: The distance of frequencies in the region of second harmonics is still 0.05 kT, not 0.1 kT, confirming their explanation by magnetic breakdown.

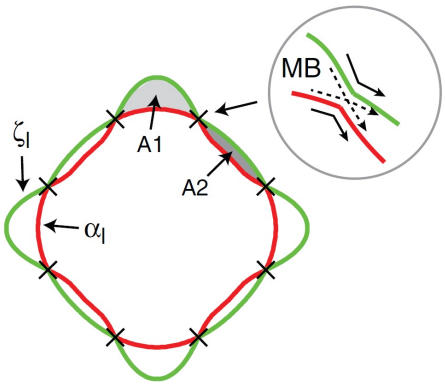


**Figure 5.21:** The frequencies of the breakdown orbits can be explained assuming a certain number of disconnected areas between the inner and the middle tube: four areas $A_1$ and four areas $A_2$, where $A_1 = 2A_2$, so that $A_{middle} = A_{inner} + 12A_2$ and the frequency corresponding to $A_2$ is 50 T. Taken from [12]. Possibly $A_2 = 2A_1$ as predicted by LDA+DMFT calculations [73].

where $V$ is the volume of the crystal and the factor of two is due to the spin degeneracy (spin quantum number 1/2). Expressing $V_\mathrm{F}$ as a fraction $f$ of the volume of the first Brillouin zone $V_{BZ} = (2\pi)^3/V_{uc}$, where $V_{uc}$ is the volume of the primitive unit cell of the direct lattice, the number $N_{uc}$ of carriers in $V_{uc}$ can be calculated.

$$f \equiv \frac{V_\mathrm{F}}{V_{BZ}}, \tag{5.29}$$

$$N_{uc} = \frac{N}{V} V_{uc} = 2f. \tag{5.30}$$

The Fermi volumes of the different bands of $KFe_2As_2$, $RbFe_2As_2$, and $CsFe_2As_2$ were estimated by approximating the inner, middle, and outer hole tubes, as well as the hole tubes at the corners of the BZ, as cylinders and the hole pocket at the top center of the BZ as a sphere. Adding up the contributions of the different bands, the Fermi volume of $KFe_2As_2$ can be calculated to be approximately $f = 51.4\,\%\,\mathrm{BZ}$, or roughly $50\,\%\,\mathrm{BZ}$. The volume of the conventional body centered tetragonal (bct) Brillouin zone $f$ refers to is $V_{BZ} = 2 \cdot (2\pi)^3/(a^2 c)$. The volume of the respective cell in direct space is $V_{uc} = a^2 c/2$, the volume of the primitive unit cell (and half the volume of the conventional bct unit cell). Hence the number of holes per primitive unit cell is approximately one. Since there is one formula unit in the primitive unit cell, there is one hole per two iron atoms and the iron atoms are nominally in a $3d^{5.5}$ configuration, if full ionization of $K^{1+}$ and $As^{3-}$ is assumed. The hole count confirms the nominal doping of one hole per formula unit, or 0.5 holes per iron atom, inferred from replacing $Ba^{2+}$ by $K^{1+}$ in $BaFe_2As_2$. For $BaFe_2As_2$ Terashima *et al.* [74] give a count of 0.0235 holes and 0.0246 electrons per primitive cell, so the hole and electron counts compensate and the iron atoms in $BaFe_2As_2$ are nominally in a $3d^6$ state.

The deduced hole count of $KFe_2As_2$ agrees well with data of Terashima *et al.* [12], who obtain $f = 51.3\,\%\,\mathrm{BZ}$ by dHvA measurements, and with data of Yoshida *et al.* [13], who obtain $f = 60\,\%\,\mathrm{BZ}$ from ARPES measurements, stating that the values deduced from ARPES are typically $10 - 20\%$ larger than for dHvA due to excess carriers at the sample surface.

Table 5.3.4 compares the Fermi volumes as a fraction of the Brillouin zone on a per band basis (see also figure 5.22). The contributions to the hole count of the tubes at the corner and the pocket at the top of the BZ increase in the series. The contribution of the inner tube decreases. The part of the middle tube around $q_z = 0$ makes an increasing contribution to the hole count. According to angle-dependent dHvA measurements of Terashima *et al.* [12], the wider part of the middle tube of $KFe_2As_2$ is restricted to a relatively small section around $q_z = 1$. For $RbFe_2As_2$ and $CsFe_2As_2$ the warping of the middle tube is very small and the hole count of the middle tube both at $q_z = 0$ and $q_z = 1$ increases.

Although the outer hole tube is not seen in our measurements for $RbFe_2As_2$ and $CsFe_2As_2$, its size can be inferred from the hole count, since all other bands

**Table 5.2:** The estimated Fermi volume of the five hole bands, as fractions of the respective first Brillouin zone in %. Tube-like features like the inner, middle, and outer hole tube as well as the 'petals' in the corner of the BZ were approximated as cylinders. The hole pockets at the top center of the BZ were approximated as spheres. ARPES gives estimates that are too large due to excess surface carriers [13]. For $RbFe_2As_2$ and $CsFe_2As_2$ the outer hole tube is missing in the data, but its size can be inferred assuming the same Fermi volume as for $KFe_2As_2$.

| Estimated Fermi volume $V_F$ (% BZ) | | | | | |
|---|---|---|---|---|---|
| Fermi | | $KFe_2As_2$ | | $RbFe_2As_2$ | $CsFe_2As_2$ |
| surface | dHvA[12] | ARPES[13] | $\lambda$ | $\lambda$ | $\lambda$ |
| corner | 0.86 | 2.1 | 0.85 | 1.16 | 1.46 |
| corner | 1.29 | 2.1 | 1.29 | 1.47 | 1.63 |
| inner | 8.2 | 9.1 | 8.2 | 7.7 | 6.7 |
| inner | 8.5 | 9.8 | 8.5 | 8.3 | 8.5 |
| middle | 10.3 | 12.2 | 10.4 | 11.3 | 12.0 |
| middle | 15.7 | 17.0 | 15.9 | 11.4 | 12.1 |
| outer | 25.6 | 27.3 | 25.7 | (26.8*) | (25.4*) |
| outer | - | 30.0 | - | - | - |
| top center | - | - | 0.00015 | 0.00029 | 0.0016 |
| sum | 51.3 | 61.1 | 51.4 | 24.6** | 26.0** |

*assuming a total 51.4 % BZ, as for $KFe_2As_2$.
**without the outer hole tube.

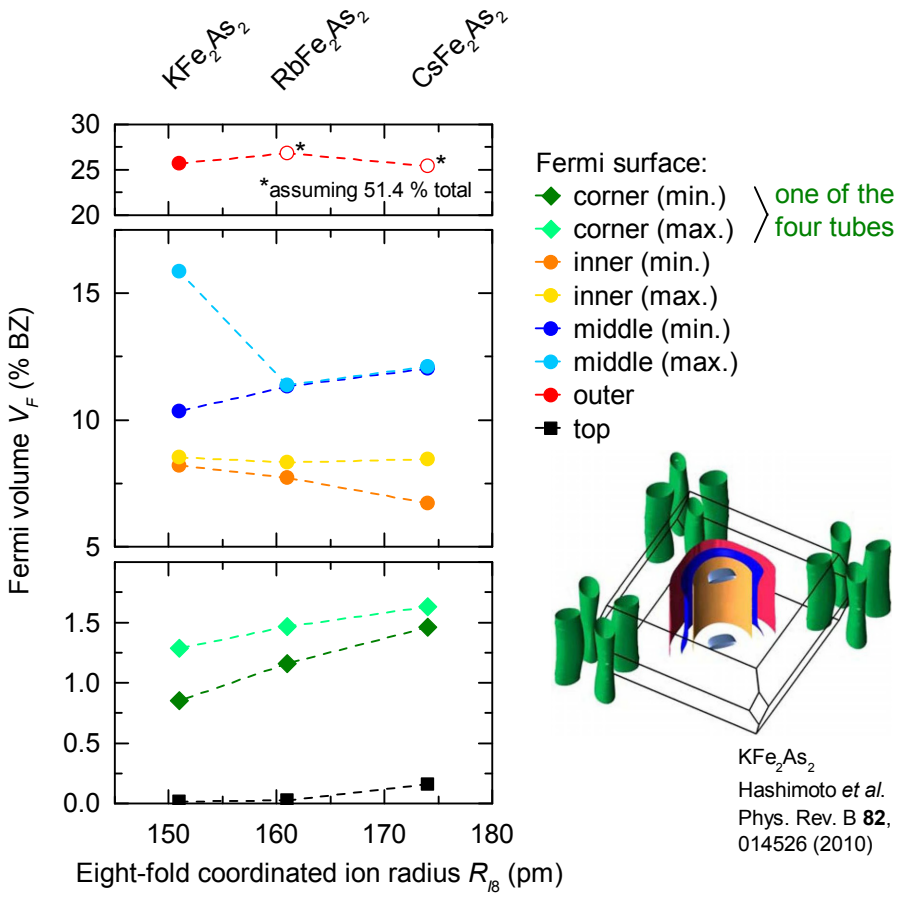


**Figure 5.22:** Fermi volume $V_F$ (% BZ) that would result if every observed frequency of the oscillatory magnetostriction was associated with a two-dimensional tube of the Fermi surface, or a sphere, in case of the pocket at the top of the Brillouin zone. To obtain the approximate $V_F$ of warped tubes, an average of the lower and the higher observed frequency must be taken. For $RbFe_2As_2$ and $CsFe_2As_2$ the value for the outer tube was deduced assuming a total count of 51.4 % BZ, as for $KFe_2As_2$. The hole count per formula unit is twice the volume fraction of the BZ. The plot of the Fermi surface of $KFe_2As_2$ was taken from Ref. [75].

are observed. This requires the assumption that the hole doping is the same for $RbFe_2As_2$ and $CsFe_2As$ as for $KFe_2As_2$ and accordingly the total Fermi volume of these compounds would also be 51.4% (or roughly 50%) of their respective Brillouin zone. With this assumption a very similar fraction of the Fermi volume is missing for $RbFe_2As_2$ and $CsFe_2As$: approximately 25%. Accordingly, a frequency belonging to the outer hole tube of roughly $7.0 - 7.4\,\mathrm{kT}$ and $6.5 - 6.9\,\mathrm{kT}$ would be expected for $RbFe_2As_2$ and $CsFe_2As$, respectively. These values lie well in the range of resolvable frequencies, so the reason for the absence in our data is probably scattering at impurities. Therefore, these frequencies should be observable for even purer samples and in higher magnetic fields.

Following this estimation, approximately half the holes counted, namely 0.5 per formula unit or 0.25 per iron atom, reside in the band belonging to the outer hole tube.

### 5.3.5 Anisotropy of the stress dependence of the Fermi surface

Since the uniaxial stress dependence of the Fermi surface enters the amplitudes of the quantum oscillations in the magnetostriction (see equation 5.21), a comparison of the oscillations of $\lambda_c$ and $\lambda_a$ for the same field direction can provide additional information on the anisotropy of the Fermi surface. Only for $RbFe_2As_2$ $\lambda_c$ and $\lambda_a$ were measured on the same crystal. Therefore, a direct comparison of absolute amplitudes is strictly only possible for this compound. Nonetheless, we attempt to compare the anisotropy also with $KFe_2As_2$ and $CsFe_2As_2$. When different samples S1, S2 with different mean free paths $l_1, l_2$ are compared, we try to correct the difference in amplitude due to the Dingle factor (equation 5.16): First the natural logarithm of the amplitude of S1 is taken, and then multiplied by the ratio of mean free paths $l_1/l_2$ determined in subsection 5.2.4. Next, the exponential function is applied, and finally the expression is multiplied by the amplitude to the power of $1 - l_1/l_2$. Figure 5.23 shows the anisotropy of the abolute value of the stress dependence of the cross-sections of the Fermi surface

$$\left|\frac{\partial F_r}{\partial \sigma_c}\right| \Big/ \left|\frac{\partial F_r}{\partial \sigma_a}\right|, \tag{5.31}$$

plotted against the structural $c/a$ ratio for $KFe_2As_2$, $RbFe_2As_2$, and $CsFe_2As_2$. The increase of the anisotropy of $|\partial F_r/\partial \sigma_i|$ from $KFe_2As_2$ to $RbFe_2As_2$ for the middle tube and the tube at the corners of the BZ, and its decrease to $CsFe_2As_2$ is reminiscent of the behavior of the anisotropy of the upper critical field (section 4.5).

## 5.4 Effective masses

### 5.4.1 Effective masses

The oscillatory magnetostriction was measured at several different temperatures $T$ (see figures 5.4 and 5.5). The Fourier spectra yield the amplitudes at different

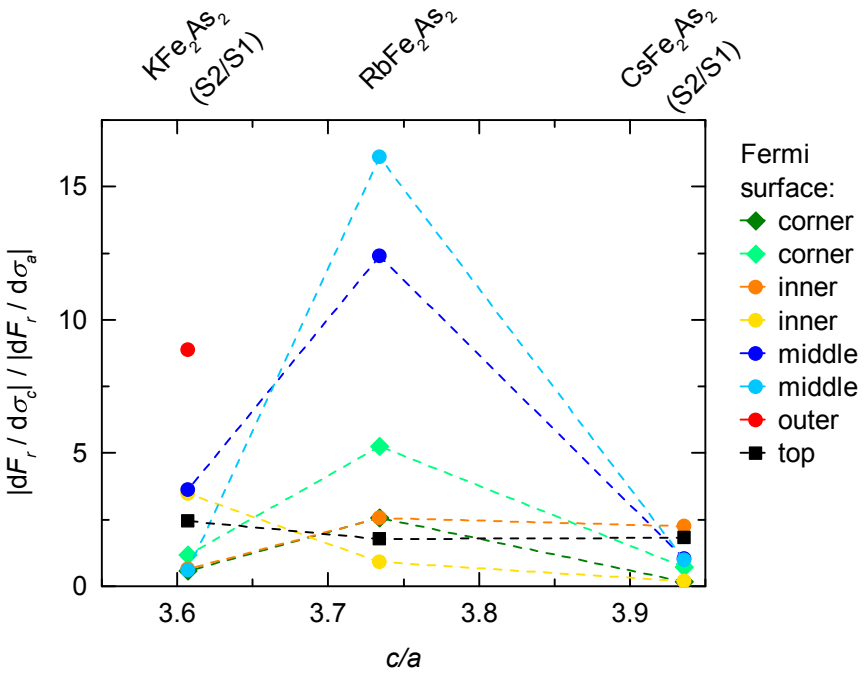


**Figure 5.23:** Anisotropy of the stress dependence of the Fermi surface $|\partial F_r/\partial\sigma_i|$, $i = a, c$, plotted against the structural $c/a$ ratio. The anisotropy can strictly only be computed for $RbFe_2As_2$ since for $KFe_2As_2$ and $CsFe_2As_2$ the quantum oscillations in $\lambda_a$ and $\lambda_c$ were measured on different samples (S1 and S2). The values for $KFe_2As_2$ and $CsFe_2As_2$ were therefore corrected for different mean free paths.

temperatures, which are needed to extract the effective quasiparticle mass $m^*$ via the temperature factor $R_T$ in the Lifshitz-Kosevich formula (eq. 5.14). The expression for $R_T$ was fitted to the amplitudes as a function of temperature, with $m^*$ as the only free parameter apart from an arbitrary scaling factor. Figures 5.24 and 5.25 shows these fits.

The effective masses of the outer tubes of $RbFe_2As_2$ and $CsFe_2As_2$ could not be determined by a fit of $R_T$, since the frequencies were not observed. Their effective masses can, however, be estimated by comparison of the Sommerfeld coefficient $\gamma$ from the effective masses of the observed bands with $\gamma$ measured by specific heat [9, 11]. The contribution of each band to the Sommerfeld coefficient can be estimated under the assumption of a two-dimensional Fermi surface with circular cross-section and a quadratic dispersion of the quasiparticles

$$\gamma = \frac{\pi^2}{3} k_\mathrm{B}^2 D(E_\mathrm{F}) \approx \frac{\pi k_\mathrm{B}^2 N_\mathrm{A} a^2}{3\hbar^2} m^* \tag{5.32}$$

where $N_\mathrm{A}$ is the Avogadro number and $a$ is the structural $a$-parameter. Adding up the contributions of the hole tubes, counting four tubes in the corner of the BZ and neglecting the hole pocket at the top of the BZ, $\gamma = 76\,\mathrm{mJ\ mol^{-1}\ K^{-2}}$ for $RbFe_2As_2$ and $\gamma = 117\,\mathrm{mJ\ mol^{-1}\ K^{-2}}$ for $CsFe_2As_2$ is obtained. Thus, to reach the measured values of $\gamma = 112\,\mathrm{mJ\ mol^{-1}\ K^{-2}}$ for $RbFe_2As_2$ and $\gamma = 178\,\mathrm{mJ\ mol^{-1}\ K^{-2}}$ for $CsFe_2As_2$ [11], fractions $\gamma = 36\,\mathrm{mJ\ mol^{-1}\ K^{-2}}$ for $RbFe_2As_2$ and $\gamma = 61\,\mathrm{mJ\ mol^{-1}\ K^{-2}}$ for $CsFe_2As_2$ are missing. This is equivalent to $m^*/m_e = 24$ for the outer tube of $RbFe_2As_2$ and $m^*/m_e = 41$ for the outer tube of $CsFe_2As_2$. According to this estimate, the outer tube has the largest $m^*$ of all bands. Together with the large size of the orbit, this makes it more difficult to observe the outer tube at small fields, providing an explanation for its absence in our data.

Figure 5.26 shows the effective quasiparticle masses of $KFe_2As_2$, $RbFe_2As_2$, and $CsFe_2As_2$ in comparison. The general trend in the series is an increase of the effective masses in all bands. The exception is the relatively small widened part around $q_z = 1$ of the middle tube of $KFe_2As_2$, which according to Terashima *et al.* [12] and Yoshida *et al.* [13] has a high $m^*/m_e$ of 18 free electron masses. But this widened part disappears for $RbFe_2As_2$ and $CsFe_2As_2$, which exhibit only very small warping of the middle tube (see figure 5.22). The part of the middle tube around $q_z = 0$ follows the trend of increasing $m^*$ in the series.

To obtain the mass enhancement caused by electronic correlations, the bare band mass $m_b$ is needed. It can be computed with density functional theory. Ikeda (formerly Kyoto University, now Ritsumeikan University) calculated the band structure with this method and the band-resolved density of states [70]. Using equation 5.32, estimates of the average band masses are obtained for the in-plane orbits. Values lie in the range $m_b \approx 0.5$ to $3\,m_e$ (see figure 5.26). This compares well with the band masses of $KFe_2As_2$ reported in Ref. [13, 72]. In the series $KFe_2As_2$ to $RbFe_2As_2$ to $CsFe_2As_2$ the band masses change very little. The mass enhancement $m^*/m_b$, in contrast, increases in the series. Figure 5.27 shows the mass enhancement plotted against the cross-sectional area of the Fermi surface of the respective band expressed

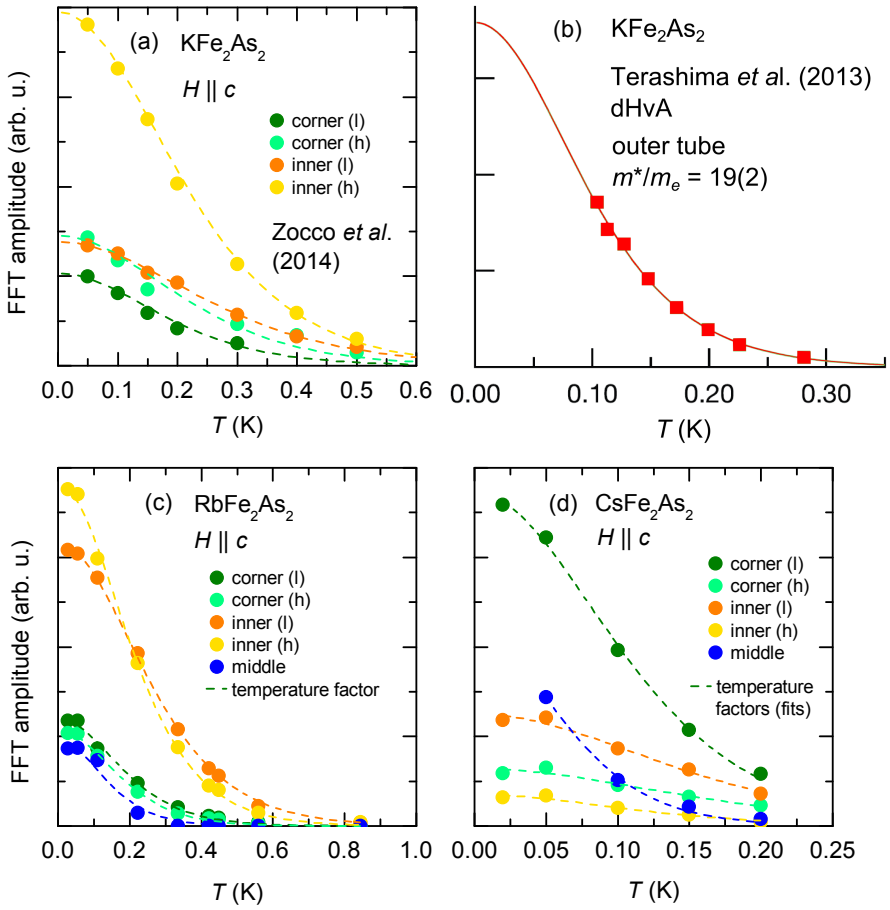


**Figure 5.24:** The temperature dependence of the Fourier amplitudes for $H \parallel c$. (a) $KFe_2As_2$ [14], (b) the outer hole cylinder of $KFe_2As_2$ measured by Terashima *et al.* [12] by dHvA oscillations, (c) $RbFe_2As_2$, (d) $CsFe_2As_2$. Effective masses $m^*$ are determined by fits of the temperature factor $R_T$ (eq. 5.14).

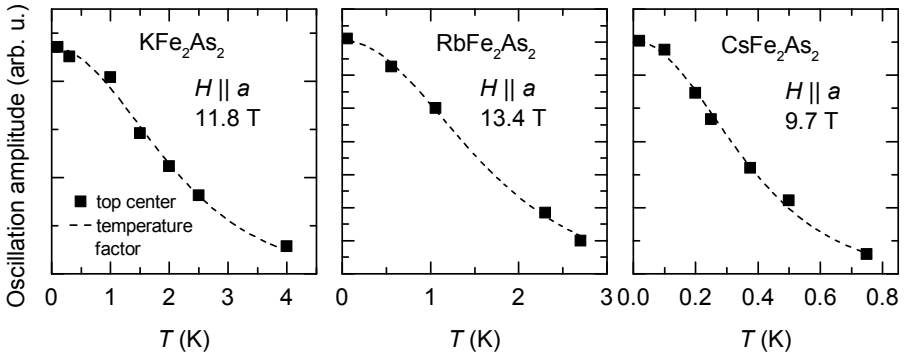


**Figure 5.25:** The temperature dependence of the Fourier amplitudes for $H \parallel a$ for $KFe_2As_2$, $RbFe_2As_2$, and $CsFe_2As_2$. Effective masses $m^*$ are determined by fits of the temperature factor $R_T$ (eq. 5.14).

as a fraction of the Brillouin zone. Apart from the hole tubes in the corner of the Brillouin zone, the mass enhancement increases with the size of the Fermi surface. Multiplied by a factor of two this is the approximate hole count of the respective bands.

### 5.4.2 Possible mechanisms behind the mass enhancement

The mass enhancement $m^*/m_b$ increases in the series $KFe_2As_2$ to $RbFe_2As_2$ to $CsFe_2As_2$ and it increases with the hole count of the tubes running through the center of the Brillouin zone. Also the mass enhancement of the tubes at the corner of the BZ zone is significant, as is the increase of the effective mass of the pocket at the top of the BZ. What mechanism causes the mass enhancement?

The hole pocket at the top of the BZ is quite small and it is located at the edge of the BZ. Therefore, spin-orbit coupling might be expected to increase its band mass [53]. The band-resolved density of states calculated by Ikeda [70], expressed as a Sommerfeld coefficient $\gamma$ is 0.28, 0.46, and $0.83\,\mathrm{mJ\,mol^{-1}\,K^{-2}}$ for $KFe_2As_2$, $RbFe_2As_2$, and $CsFe_2As_2$, respectively. These values were calculated neglecting electron-phonon interaction and spin-orbit coupling, nonetheless they can explain a factor-of-three increase of the band mass along the series. Thus, the four-fold increase of the effective mass of the band belonging to the hole pocket at the top of the BZ might be entirely due to the increase of the band mass.

The band belonging to the hole tubes at the corner of the BZ exhibits a mass enhancement that is similar to that of the outer hole tube. In fact, according to calculated band structures [72], these two features of the Fermi surface arise from the same band crossing the Fermi energy at different sections of the BZ. A complication with the hole tubes at the corner of the BZ is that flat bands of unoccupied states lie very close above the Fermi energy. Many-body interactions with these states might affect the effective mass.

Kanter *et al.* [11] speculated that flat bands close to the Fermi energy might

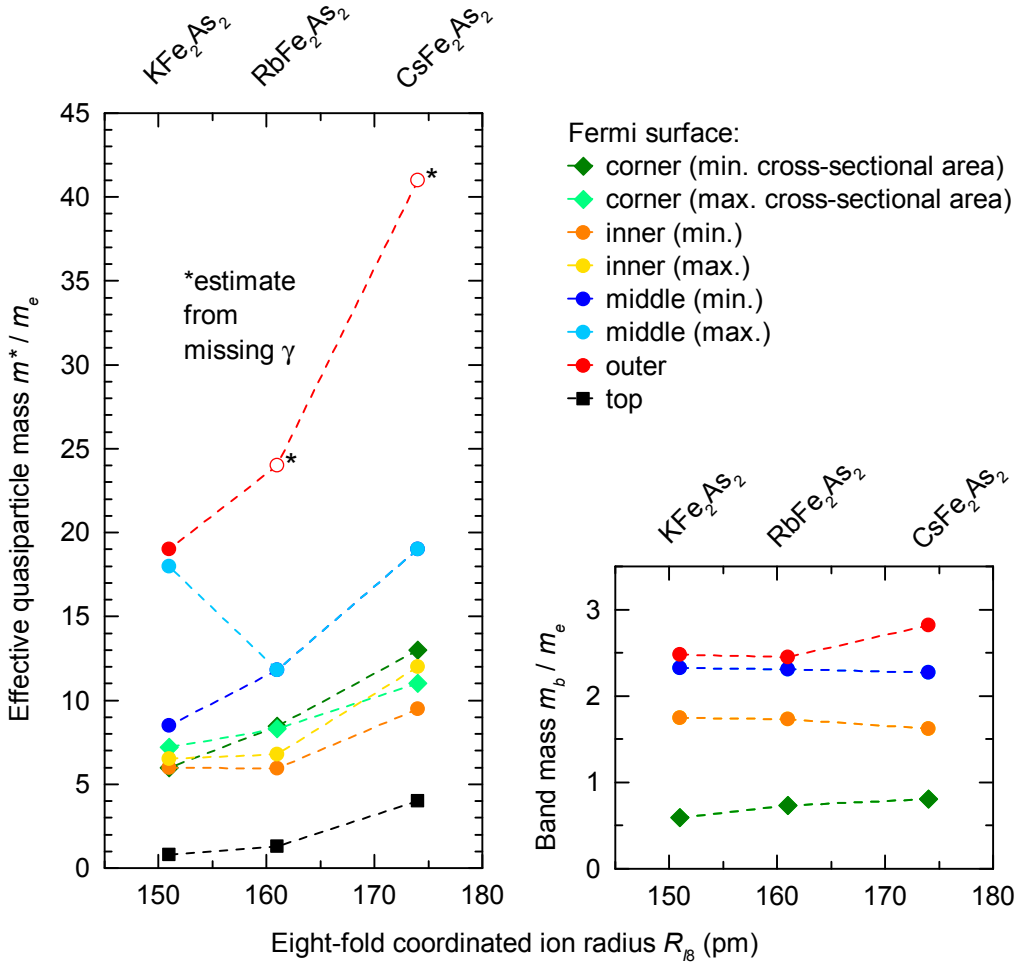


**Figure 5.26:** Left: Effective quasiparticle masses $m^*$ for all bands of $KFe_2As_2$, $RbFe_2As_2$, and $CsFe_2As_2$. The data for $KFe_2As_2$ are taken from Terashima *et al.* [12] and Zocco *et al.* [14]. The effective masses for the outer tubes of $RbFe_2As_2$ and $CsFe_2As_2$ were estimated from the missing part of the Sommerfeld coefficient of specific heat measured by Kanter *et al.* [11]. Bottom right: Band masses $m_b$, estimated from the band-resolved density of states calculated by Ikeda [70], neglecting electron-phonon interaction and spin-orbit coupling. Top right: Mass enhancement $m^*/m_b$. While the band masses change only little in the series $KFe_2As_2$ to $RbFe_2As_2$ to $CsFe_2As_2$, the mass enhancement increases.

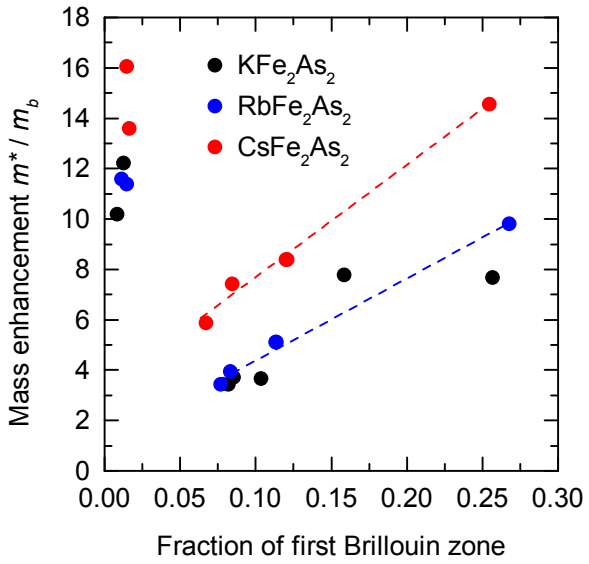


**Figure 5.27:** Mass enhancement $m^*/m_b$ for $KFe_2As_2$, $RbFe_2As_2$, and $CsFe_2As_2$, plotted against the cross-sectional area of the Fermi surface of the respective band expressed as a fraction of the first Brillouin zone. Apart from the hole tubes in the corner of the first Brillouin zone the mass enhancement increases with the size of the Fermi surface, which measures the hole count when multiplied by a factor of two.

explain the large observed Sommerfeld coefficient of $RbFe_2As_2$ and $CsFe_2As_2$. They encouraged quantum oscillation studies on single crystals to test that hypothesis. The calculations of the band mass and the mass enhancement (fig. 5.26) show that the band mass cannot explain the increase of $m^*$ in the $A122$ series, nor the increase of $m^*$ with the hole count of the tubes running through the center of the BZ. The explanation of these observations is thus an open problem.

The electronic correlations of iron-based superconductors cannot be explained by models considering only repulsive Coulomb interactions by including a Hubbard $U$ in the Hamiltonian [44]. One hypothesis for the origin of correlations is the effect of intraorbital exchange interactions, also called Hund's rule coupling $J$ (for a review by Georges and de Medici see reference [76]). In this picture Hund's rule coupling works to decouple different bands and to increase correlations selectively for different bands. This way bands can have different proximity to a Mott transition. If one band undergoes a Mott transition while other bands stay itinerant, this is called an orbital-selective Mott transition [44]. Considering the filling of a band as a parameter, a Mott transition is reached for half filling. In the case of iron $d$-orbitals, half filling is realized for an occupation of five electrons or holes, if all the $d$-orbitals are treated on equal footing. If, however, the orbitals are decoupled by crystal-field effects or Hund's rule coupling, filling must be considered for every orbital separately and half filling is realized for one electron or hole per orbital. According to calculations by de' Medici *et al.* [44] for the $Ba_{1-x}K_xFe_2As_2$ series, the filling is different for the different $d$-orbitals. Hence the $d$-bands have different proximity to the Mott transition and exhibit differences in mass enhancement. Specifically, de' Medici *et al.* [44] predict the largest mass enhancement for bands bearing predominantly $d_{xy}$ character.

The band associated with the outer hole tube has the largest effective mass. From polarization dependent ARPES measurements on $KFe_2As_2$, Yoshida *et al.* [13] deduce a dominant $yz$, $xz$, and $xy$ character of the inner, middle, and outer Fermi surface in the center of the BZ, respectively. Also, LDA and LDA+DMFT calculations on $KFe_2As_2$ [73] predict a predominant $d_{xy}$ character of the outer hole tube. Therefore, the scenario of a proximity to an orbital-selective Mott transition is in line with our data. The outer tube is also the best candidate for a Mott transition, since it has the largest cross-section of the Fermi surface, therefore the largest contribution to the hole count, so it is closest to half-filling.

Wu *et al.* [77] invoke decoupled bands with different degrees of electronic correlations without Hund's rule coupling as the cause. They explain the low in-plane magnetic moment of LaFeAsO with the effects of spin-orbit coupling, Fe $d$ and As $4p$ hybridization, and the crystal-field splitting. They state: "The presence of an itinerant band coupled to one with moderate Mott physics makes the problem of the iron pnictides more akin to that of the Kondo lattice in heavy fermions than the cuprates" [77]. This raises the question whether the observed correlation effects can be explained without invoking Hund's rule coupling.

Apart from the effective quasiparticle mass also the quasiparticle coherence scale is affected by electronic correlations. In case of decoupled bands, the coherence scale can be different for each band. As discussed by Hardy *et al.* [9], there is a

crossover of quasiparticle coherence with temperature in $KFe_2As_2$. This crossover is visible in the resistivity as a change in the temperature dependence from $T^2$ at low temperatures to a different curvature at room temperature. In thermal expansion and magnetization the crossover is visible as a broad maximum around 100 K [9]. Below the quasiparticle coherence scale quasiparticles exist in a Fermi liquid. Above the scale they lose coherence and cease to exist. The magnetization (figure 2.5) and the thermal expansion [19] of $RbFe_2As_2$ and $CsFe_2As_2$ are similar to that of $KFe_2As_2$, but show the broad maximum at lower temperatures, pointing to a lower quasiparticle coherence scale. According to Georges *et al.* [76] Hund's rule coupling reduces the quasiparticle coherence scale of non-half-filled bands.

Independent of the exact mechanism, it can be stated that some effect decouples the different bands and selectively increases their effective masses, quite possibly tuning the proximity to orbital-selective Mott transitions and the quasiparticle coherence scale. This mechanism is not only driven by doping as in the $Ba_{1-x}K_xFe_2As_2$ series but also by replacing K by Rb and finally by Cs in the $AFe_2As_2$ series.

## 5.5 Possible links between superconductivity and electronic correlations

Most iron-based superconductors exhibit $\gamma$ values that would be typical also for conventional superconductors or organic superconductors. Only $Ba_{1-x}K_xFe_2As_2$, $RbFe_2As_2$, and $CsFe_2As_2$ venture into the realm of $\gamma$ values typical for heavy-fermion superconductors. The origin of electronic correlations in these iron-based superconductors, which are *d*-metals, is an unsolved mystery (see section 5.4). Possibly, exchange interactions (Hund's rule coupling) lie behind this peculiar behavior [44, 76].

Figure 5.28 shows the Sommerfeld coefficient of the specific heat in the normal state, $\gamma$, of $Ba_{1-x}K_xFe_2As_2$, $RbFe_2As_2$, and $CsFe_2As_2$, plotted against the superconducting transition temperature $T_c$. Starting at a low $\gamma$ value for $BaFe_2As_2$, the Sommerfeld coefficient rises as $T_c$ reaches its maximum value for $Ba_{0.6}K_{0.4}Fe_2As_2$, and rises further, while $T_c$ decreases towards $KFe_2As_2$, $RbFe_2As_2$, and $CsFe_2As_2$. Impurities in single crystals or powders can increase the Sommerfeld coefficient and thus may lead to an overestimation of electronic correlations intrinsic to a material. This explains the variation in Sommerfeld coefficients reported for $Ba_{1-x}K_xFe_2As_2$, in addition to the difficulties of extracting the normal-state Sommerfeld coefficient from the specific heat of a superconductor with relatively high $T_c$. For $KFe_2As_2$, $RbFe_2As_2$, and $CsFe_2As_2$ the large Sommerfeld coefficients are confirmed by the effective masses determined from quantum oscillations. Therefore, their origin really lies in electronic correlations and not in impurities.

The specific heat of $KFe_2As_2$, $RbFe_2As_2$, and $CsFe_2As_2$ displays a similar jump $\Delta C$ at the superconducting transition [9, 78, 79] (see figure 5.29). Plotted against $T_c$, this jump $\Delta C$ does not follow the phenomenological Bud'ko-Ni-Canfield (BNC) scaling $\Delta C \propto T_c^3$ observed for many iron-based superconductors [80] (see figure

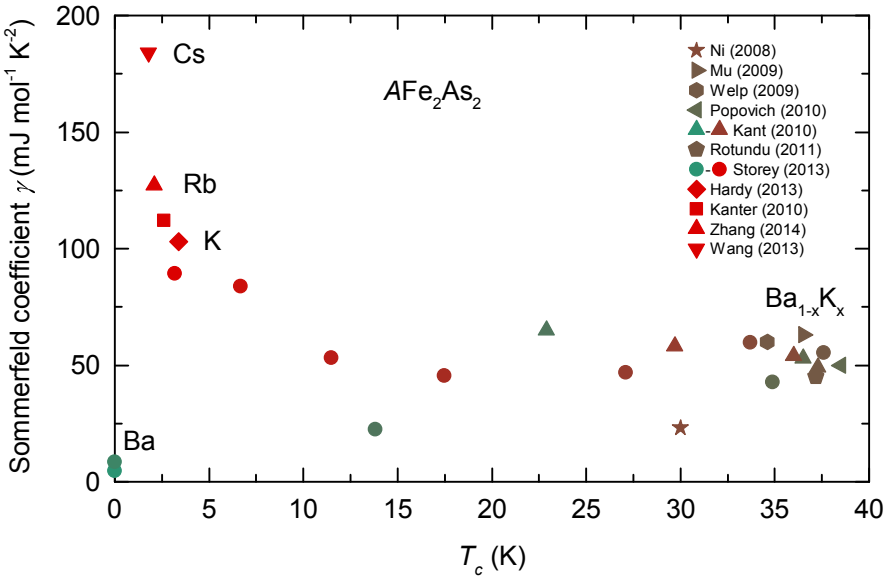


**Figure 5.28:** The Sommerfeld coefficient of the specific heat $\gamma$ of $Ba_{1-x}K_xFe_2As_2$, $RbFe_2As_2$, and $CsFe_2As_2$, plotted against the superconducting transition temperature $T_c$.

5.30). This deviation from BNC scaling would vanish, if the large Sommerfeld coefficient $\gamma$ was included by plotting $\Delta C/\gamma$ against $T_c$. The quantity $\Delta C/\gamma T_c$ is predicted to be 1.43 by BCS theory for weak coupling, and it is expected to increase with coupling strength. The value is expected to decrease with increasing anisotropy in the single-band case and to decrease with increasing difference between intraband coupling strengths in the tow-band case [27]. Thus, the low values $\Delta C/\gamma T_c \approx 0.54$, 0.42, 0.36 of $KFe_2As_2$, $RbFe_2As_2$, and $CsFe_2As_2$, respectively, may be explained by the different coupling strengths of the distinct bands. For $KFe_2As_2$ pairing potentials for individual bands were discussed in the framework of a four-band BCS model by Hardy *et al.* [30].

According to figure 2.2, the iron-arsenic layers of $CsFe_2As_2$ have nearly the same structure as those of $Ba_{0.5}K_{0.5}Fe_2As_2$, which is quite close to the optimally doped $Ba_{0.6}K_{0.4}Fe_2As_2$. Considering the vastly different superconducting transition temperatures of 2.25 K and $35 - 38$ K, respectively, it would be interesting to study the differences between the two compounds. One difference is the interlayer coupling, since $CsFe_2As_2$ has a larger spacer atom between the iron-arsenic layers than $Ba_{0.5}K_{0.5}Fe_2As_2$. Another difference is the doping, with a nominal doping of 0.5 holes per iron atom for $CsFe_2As_2$ and 0.25 holes per iron atom for $Ba_{0.5}K_{0.5}Fe_2As_2$. In the course of the hole doping, there is a change of the Fermi surface, a Lifshitz transition, where the electron-like features of the Fermi surface vanish and only hole-like features remain (see section 5.3). In the $T_c$-$x$ phase diagram, $Ba_{0.5}K_{0.5}Fe_2As_2$ lies close to the center of the superconducting dome, possibly more exposed to fluc-

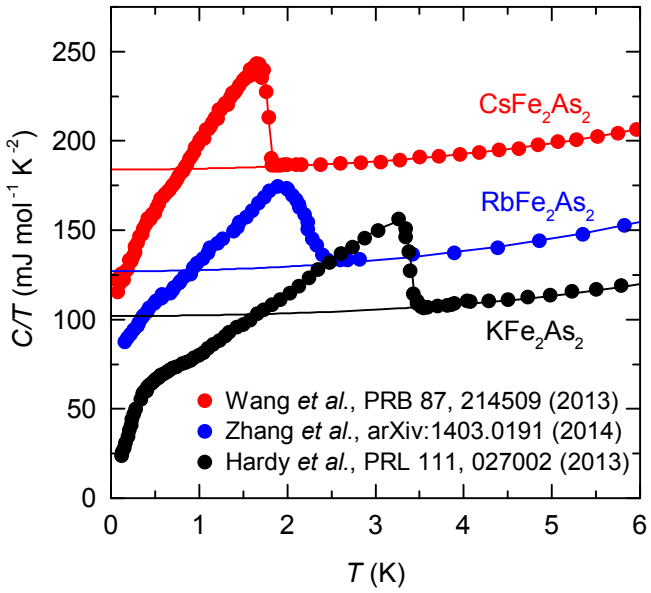


**Figure 5.29:** The specific heat divided by temperature $C/T$ of $KFe_2As_2$ [9], $RbFe_2As_2$ [78], and $CsFe_2As_2$ [79]. The jump of the specific heat $\Delta C$ at the superconducting transition is of similar height for the three compounds.

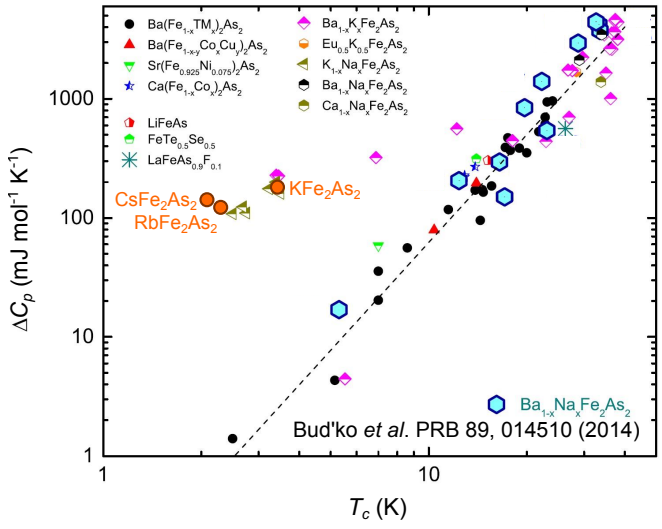


**Figure 5.30:** The jump of the specific heat $\Delta C$, plotted against $T_c$ of various 122-materials (extended, from Ref. [80]). The line marks the so-called Bud'ko-Ni-Canfield (BNC) scaling $\Delta C \propto T_c^3$. The series $Ba_{1-x}K_xFe_2As_2$ [81], $RbFe_2As_2$ [11, 78], $CsFe_2As_2$ [79], and $K_{1-x}Na_xFe_2As_2$ [82] do not obey BNC scaling due to their large Sommerfeld coefficient (see text).

tuations in the wake of the magneto-structural transition.

In the picture of band-selective proximities to Mott transitions [44], increasing hole doping causes a decoupling of the bands, restricting orbital fluctuations. So a reduction of fluctuations goes hand in hand with increasing hole concentration and increasing electronic correlations. In $MgB_2$ the high $T_c$ of 39 K is reached by the interaction of two anisotropic bands with electron-phonon coupling as the pairing glue [27, 83]. If some sort of fluctuations, especially involving interband interactions, are essential to the pairing in $Ba_{1-x}K_xFe_2As_2$, $RbFe_2As_2$, and $CsFe_2As_2$, then the decoupling of the bands might explain the reduction of $T_c$ in the series.

### 5.5.1 Uniaxial pressure dependences

One means to study the relation between superconductivity and electronic correlations is to change a tuning parameter and to see how that affects each. Hydrostatic pressure $p$ is a suitable tuning parameter. It is known how $T_c$ decreases with pressure for $KFe_2As_2$ [84], $RbFe_2As_2$ [85], and $CsFe_2As_2$ [86]. Remarkably, $T_c$ starts to increase again, after some critical pressure $p_c$ is reached (observed for $KFe_2As_2$ [84] and $CsFe_2As_2$ [86]). Unfortunately, no measurements of the Sommerfeld coefficient under pressure have been reported to date. The increase of the unit-cell volume in the series $KFe_2As_2$, to $RbFe_2As_2$, to $CsFe_2As_2$ cannot be used as a substitute for 'negative' pressure. Since $T_c$ decreases in this series, its development cannot be ascribed to a simple volume effect. Thermal expansion curves at low temperature (figure 4.2) deliver the uniaxial pressure dependence of both the Sommerfeld coefficient $\gamma$ and $T_c$ at zero pressure (see equations 3.14 and 3.16). Figure 5.31 shows the uniaxial pressure dependence of these quantities, for the $a$- and for the $c$-direction. Some reservations are in order regarding the absolute values of the uniaxial pressure dependence in the $c$-direction, as discussed in section 4.2. Ignoring these, it can be stated that in the light of uniaxial pressure, superconductivity and electronic correlations in the normal state seem to be unrelated in $KFe_2As_2$, somewhat related in $RbFe_2As_2$, and going hand-in-hand in $CsFe_2As_2$ (see figure 5.31).

## 5.6 Conclusions

The Fermi liquids in $KFe_2As_2$, $RbFe_2As_2$, and $CsFe_2As_2$ exhibit increasingly strong electronic correlations. The first experimental information on the Fermi surfaces of $RbFe_2As_2$ and $CsFe_2As$ was obtained by means of quantum oscillations in the magnetostriction, comparing frequencies with those of $KFe_2As_2$, for which the Fermi surface has already been well studied [12–14]. The topology of the Fermi surfaces remains the same in the series, while some particular features change in size. The size of the small pocket at the top center of the Brillouin zone increases systematically, as well as the size of the warped tubes at the corners of the Brillouin zone. The average cross-section of the inner tube running through the center of the Brillouin zone decreases, while the large part of the middle tube increases. The cross-section of the outer tube is not observed in the measurements on $RbFe_2As_2$ and $CsFe_2As_2$,

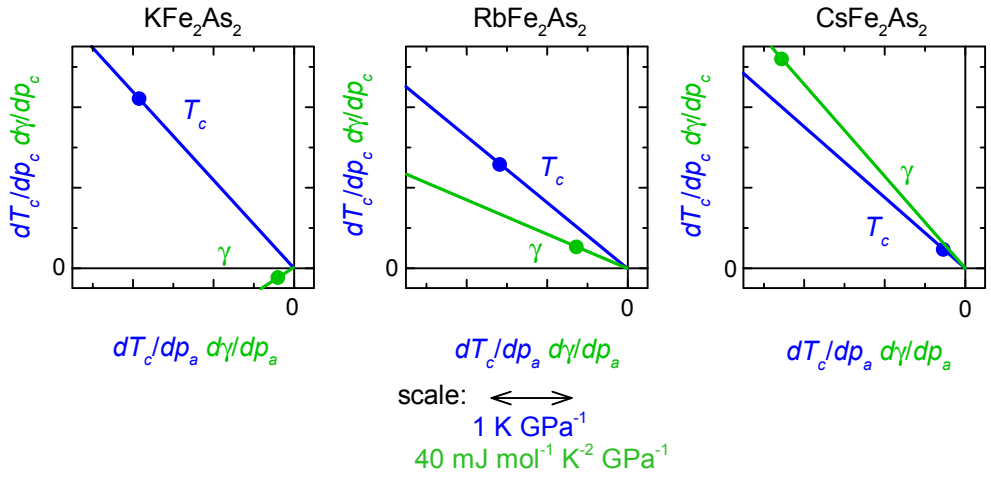


**Figure 5.31:** The uniaxial pressure dependence with respect to the $a$- and to the $c$-direction of the superconducting transition temperature, $T_c$, and of the Sommerfeld coefficient in the normal state, $\gamma$, of $KFe_2As_2$, $RbFe_2As_2$, and $CsFe_2As_2$ as determined from thermal expansion (see figure 4.2). The lines denote the respective combination of uniaxial pressure along $a$ and along $c$ that would lead to a maximum effect on $T_c$ (blue) or on $\gamma$ (green). Reservations regarding absolute values apply (see section 4.2).

but it can be estimated under the plausible assumption that the hole count remains the same in the series. The hole count confirms the nominal hole doping of one hole per formula unit, corresponding to a nominal $3d^{5.5}$ state of the iron atoms. Effective quasiparticle masses increase within the series, albeit with differences between the bands. The effective mass belonging to the outer tubes can be estimated from the Sommerfeld coefficient and effective masses of all other bands. The mass enhancement compared to the band mass is largest for the outer tube and the tubes at the corner of the Brillouin zone.

The large effective quasiparticle masses cannot be explained by calculations in the local density approximation, therefore remormalization effects must be responsible [72, 73]. One hypothesis for the mechanism behind the correlation effects is the scenario of a proximity to an orbital-selective Mott transition [44]. In this picture, Hund's rule coupling decouples the bands and increases electronic correlations with different strength in different bands. Specifically, bands with dominating $d_{xy}$ character that are close to half-filling are predicted to be closest to an orbital-selective Mott transition [44]. The effective quasiparticle masses determined from quantum oscillations confirm differences in mass enhancement between the bands. The outer hole tube running through the center of the Brillouin zone has the largest hole count and the largest mass enhancement. This is compatible with the scenario of band-dependent proximity to a Mott transition laid out by de' Medici *et al.* [44].

# 6 Summary

$KFe_2As_2$, $RbFe_2As_2$, and $CsFe_2As_2$ are a series of rather clean, ambient-pressure, low-temperature superconductors well suited to study several intriguing aspects of the class of iron-based superconductors. This thesis presents a comparative study of these materials based on thermal expansion and magnetostriction measurements at very low temperatures.

Much is already known about $KFe_2As_2$, including its $H$-$T$ phase diagram [8, 10] and its Fermi surface consisting of three hole tubes in the center of the Brillouin zone, one hole tube in every corner, and a hole pocket at the top center [12–14]. The origin of the enhanced Sommerfeld coefficient and the enhanced effective masses of $KFe_2As_2$ has already been discussed in the framework of band-dependent proximities to Mott transitions caused by Hund's rule coupling [9, 44]. But the issue of strong electronic correlations in iron-based superconductors, which are $d$ metals, is not settled and remains one of the most intriguing aspects of these materials. Although it is known for several years that $RbFe_2As_2$ and $CsFe_2As_2$ have even larger Sommerfeld coefficients than $KFe_2As_2$ [11], only now have single crystals of $RbFe_2As_2$ and $CsFe_2As_2$ become available in sufficient quality to study the Fermi surface and effective quasiparticle masses experimentally.

This thesis presents the first $H$-$T$ phase diagrams of $RbFe_2As_2$ and $CsFe_2As_2$ single crystals down to very low temperatures. The field anisotropy of these phase diagrams is considerable, with an orbitally limited upper critical field for magnetic fields applied parallel to the $c$ direction and a paramagnetically limited upper critical field for magnetic fields applied parallel to the $ab$ plane. The multiband character of superconductivity leaves its fingerprint in the $H$-$T$ phase diagrams and in the thermal expansion curves presented in this work. This data thus enables future theoretical studies of multiband superconductivity in $RbFe_2As_2$ and $CsFe_2As_2$ in addition to $KFe_2As_2$, so that now a series of three similar systems is available for such studies.

The now available single crystals are pure enough to display quantum oscillations. This thesis presents quantum oscillations of the magnetostriction and delivers the first experimental data on the Fermi surfaces and the effective quasiparticle masses of $RbFe_2As_2$ and $CsFe_2As_2$. All Fermi surfaces could be observed except the outer hole tube running through the center of the Brillouin zone. Its properties could be deduced, however, from the properties of all other bands with the help of the total hole count and the total Sommerfeld coefficient. The Fermi surfaces of $RbFe_2As_2$ and $CsFe_2As_2$ exhibit the same general features as those of $KFe_2As_2$, with differences in the size of particular features. The hole pocket at the top center of the Brillouin zone grows in the series $KFe_2As_2$ to $RbFe_2As_2$ to $CsFe_2As_2$. In that sense, the Fermi

surface of $CsFe_2As_2$ is most three-dimensional. The cross-section of the warped tubes in the corner of the Brillouin zone increases in the series, as well as the main part of the middle tube running through the center of the Brillouin zone. The cross-section of the inner tube in the center decreases and the cross-section of the outer tube can be estimated to remain approximately the same fraction of the Brillouin zone. As the exact cross-sections of the Fermi surfaces cannot be obtained by calculations in the framework of density functional theory due to the large electronic correlations, the measurements of the Fermi surfaces will proof valuable in theoretical studies of material properties and in the development of more sophisticated theoretical tools for the calculation of the electronic structure.

The measured effective quasiparticle masses of all bands increase in the series $KFe_2As_2$ to $RbFe_2As_2$ to $CsFe_2As_2$. A comparison with calculated band masses yields the mass enhancement. This is largest for the band associated with the hole tubes in the corner of the Brillouin zone and the outer hole tube in the center of the Brillouin zone. The fact that the largest mass enhancement occurs for the band with the largest hole count and predominant $d_{xy}$ character is compatible with the Hund's rule coupling scenario for the origin of the mass enhancement already laid out for $KFe_2As_2$ [9, 44]. Future theoretical studies must now test if this scenario of band-dependent proximities to Mott transitions caused by Hund's rule coupling really also explains the mass enhancements in $RbFe_2As_2$ and $CsFe_2As_2$.

# Bibliography


[1] M. R. Norman, "The challenge of unconventional superconductivity," Science **332**, 196 (2011).

[2] Y. Kamihara, T. Watanabe, M. Hirano, and H. Hosono, "Iron-based layered superconductor La[$O_{1-x}F_x$]FeAs ($x = 0.05 - 0.12$) with $T_c = 26$ K," J. Am. Chem. Soc. **130**, 3296 (2008).

[3] D. C. Johnston, "The puzzle of high temperature superconductivity in layered iron pnictides and chalcogenides," Adv. Phys. **59**, 803 (2010).

[4] J. Paglione and R. L. Greene, "High-temperature superconductivity in iron-based materials," Nature Phys. **6**, 645 (2010).

[5] G. R. Stewart, "Superconductivity in iron compounds," Rev. Mod. Phys. **83**, 1589 (2011).

[6] P. J. Hirschfeld, M. M. Korshunov, and I. I. Mazin, "Gap symmetry and structure of Fe-based superconductors," Rep. Prog. Phys. **74**, 124508 (2011).

[7] A. Chubukov, "Pairing mechanism in Fe-based superconductors," Annu. Rev. Condens. Matter Phys. **3**, 57 (2012).

[8] P. Burger, F. Hardy, D. Aoki, A. E. Böhmer, R. Eder, R. Heid, T. Wolf, P. Schweiss, R. Fromknecht, M. J. Jackson, C. Paulsen, and C. Meingast, "Strong pauli-limiting behavior of $H_{c2}$ and uniaxial pressure dependencies in $KFe_2As_2$," Phys. Rev. B **88**, 014517 (2013).

[9] F. Hardy, A. E. Böhmer, D. Aoki, P. Burger, T. Wolf, P. Schweiss, R. Heid, P. Adelmann, Y. X. Yao, G. Kotliar, J. Schmalian, and C. Meingast, "Evidence of strong correlations and coherence-incoherence crossover in the iron pnictide superconductor $KFe_2As_2$," Phys. Rev. Lett. **111**, 027002 (2013).

[10] D. A. Zocco, K. Grube, F. Eilers, T. Wolf, and H. v. Löhneysen, "Pauli-limited multiband superconductivity in $KFe_2As_2$," Phys. Rev. Lett. **111**, 057007 (2013).

[11] J. Kanter, Z. Bukowski, J. Karpinski, and B. Batlogg, "Heavy quasi particle mass in (Rb,Cs)$Fe_2As_2$," in *Annual Report of the Laboratory for Solid State Physics* (ETH Zürich, Department of Physics, 2010).

[12] T. Terashima, N. Kurita, M. Kimata, M. Tomita, S. Tsuchiya, M. Imai, A. Sato, K. Kihou, C.-H. Lee, H. Kito, H. Eisaki, A. Iyo, T. Saito, H. Fukazawa, Y. Kohori, H. Harima, and S. Uji, "Fermi surface in $KFe_2As_2$ determined via de Haas–van Alphen oscillation measurements," Phys. Rev. B **87**, 224512 (2013).

[13] T. Yoshida, S.-i. Ideta, I. Nishi, A. Fujimori, M. Yi, R. Moore, S.-K. Mo, D. Lu, Z.-X. Shen, Z. Hussain, K. Kihou, C. H. Lee, A. Iyo, H. Eisaki, and H. Harima, "Orbital character and electron correlation effects on two- and three-dimensional Fermi surfaces in $KFe_2As_2$ revealed by angle-resolved photoemission spectroscopy," Front. Physics **2**, 17 (2014).

[14] D. A. Zocco, K. Grube, F. Eilers, T. Wolf, and H. v. Löhneysen, "Fermi surface of $KFe_2As_2$ from quantum oscillations in magnetostriction," (2014), arXiv:1401.4403 .

[15] R. D. Shannon, "Revised effective ionic radii and systematic studies of interatomic distances in halides and chalcogenides," Acta Crystallogr. Sect. A **32**, 751 (1976).

[16] D. Johrendt and R. Pöttgen, "Superconductivity, magnetism and crystal chemistry of $Ba_{1-x}K_xFe_2As_2$," Physica C **469**, 332 (2009).

[17] M. Rotter, M. Pangerl, M. Tegel, and D. Johrendt, "Superconductivity and crystal structures of $(Ba_{1-x}K_x)Fe_2As_2$ ($x$ =0–1)," Angew. Chem. Int. Ed. **47**, 7949 (2008).

[18] S. A. J. Kimber, A. Kreyssig, Y.-Z. Zhang, H. O. Jeschke, R. Valenti, F. Yokaichiya, E. Colombier, J. Yan, T. C. Hansen, T. Chatterji, R. J. McQueeney, P. C. Canfield, A. I. Goldman, and D. N. Argyriou, "Similarities between structural distortions under pressure and chemical doping in superconducting $BaFe_2As_2$," Nat. Mater. **8**, 471 (2009).

[19] A. Böhmer, *Competing Phases in Iron-Based Superconductors Studied by High-Resolution Thermal-Expansion and Shear-Modulus Measurements*, Ph.D. thesis (2014), Karlsruher Institut für Technologie (KIT).

[20] S. Drobnik, *Thermische Ausdehnung und Magnetostriktion von $CeCu_{6-x}Au_x$ bei sehr tiefen Temperaturen*, Ph.D. thesis (2008), Karlsruher Institut für Technologie (KIT).

[21] S. Zaum, *Thermische Ausdehnung, Magnetostriktion und Thermokraft von $CeCoIn_5$ und $CeCu_{6-x}Au_x$ bei sehr tiefen Temperaturen*, Ph.D. thesis (2011), Karlsruher Institut für Technologie (KIT).

[22] M. Watanabe, M. Morishita, and Y. Ootuka, "Magnetoresistance of $RuO_2$-based resistance thermometers below 0.3 K," Cryogenics **41**, 143 (2001).

[23] D. S. Inosov, J. T. Park, A. Charnukha, Y. Li, A. V. Boris, B. Keimer, and V. Hinkov, "Crossover from weak to strong pairing in unconventional superconductors," Phys. Rev. B **83**, 214520 (2011).

[24] L. Boeri, O. V. Dolgov, and A. A. Golubov, "Is $LaFeAsO_{1-x}F_x$ an electron-phonon superconductor?" Phys. Rev. Lett. **101**, 026403 (2008).

[25] Z. P. Yin, A. Kutepov, and G. Kotliar, "Correlation-enhanced electron-phonon coupling: Applications of GW and screened hybrid functional to bismuthates, chloronitrides, and other high-$T_c$ superconductors," Phys. Rev. X **3**, 021011 (2013).

[26] Y. Ota, K. Okazaki, Y. Kotani, T. Shimojima, W. Malaeb, S. Watanabe, C.-T. Chen, K. Kihou, C. H. Lee, A. Iyo, H. Eisaki, T. Saito, H. Fukazawa, Y. Kohori, and S. Shin, "Evidence for excluding the possibility of d-wave superconducting-gap symmetry in ba-doped $KFe_2As_2$," Phys. Rev. B **89**, 081103 (2014).

[27] M. Zehetmayer, "A review of two-band superconductivity: materials and effects on the thermodynamic and reversible mixed-state properties," Supercond. Sci. Technol. **26**, 043001 (2013).

[28] F. Bouquet, R. A. Fisher, N. E. Phillips, D. G. Hinks, and J. D. Jorgensen, "Specific heat of $Mg^{11}B_2$: Evidence for a second energy gap," Phys. Rev. Lett. **87**, 047001 (2001).

[29] F. Bouquet, Y. Wang, R. A. Fisher, D. G. Hinks, J. D. Jorgensen, A. Junod, and N. E. Phillips, "Phenomenological two-gap model for the specific heat of $MgB_2$," Europhys. Lett. **56**, 856 (2001).

[30] F. Hardy, R. Eder, M. Jackson, D. Aoki, C. Paulsen, T. Wolf, P. Burger, A. Böhmer, P. Schweiss, P. Adelmann, R. A. Fisher, and C. Meingast, "Multiband superconductivity in $KFe_2As_2$: Evidence for one isotropic and several lilliputian energy gaps," J. Phys. Soc. Jpn. **83**, 014711 (2014).

[31] S. L. Bud'ko, Y. Liu, T. A. Lograsso, and P. C. Canfield, "Hydrostatic and uniaxial pressure dependence of superconducting transition temperature of $KFe_2As_2$ single crystals," Phys. Rev. B **86**, 224514 (2012).

[32] C. Meingast, F. Hardy, R. Heid, P. Adelmann, A. Böhmer, P. Burger, D. Ernst, R. Fromknecht, P. Schweiss, and T. Wolf, "Thermal expansion and grüneisen parameters of $Ba(Fe_{1-x}Co_x)_2As_2$: A thermodynamic quest for quantum criticality," Phys. Rev. Lett. **108**, 177004 (2012).

[33] G. Brändli, "Magnetostriktion in Supraleitern," Phys. Kondens. Mater. **11**, 111 (1970).

[34] K. H. Bennemann and J. B. Ketterson, *Superconductivity* (Springer-Verlag, 2008).

[35] A. Larkin and Y. Ovchinnikov, "Pinning in type II superconductors," J. Low. Temp. Phys. **34**, 409 (1979).

[36] A. B. Pippard, "A possible mechanism for the peak effect in type II superconductors," Philos. Mag. **19**, 217 (1969).

[37] H. K. Mak, P. Burger, L. Cevey, T. Wolf, C. Meingast, and R. Lortz, "Thermodynamic observation of a vortex melting transition in the Fe-based superconductor $Ba_{0.5}K_{0.5}Fe_2As_2$," Phys. Rev. B **87**, 214523 (2013).

[38] P. Burger, *Thermodynamische Eigenschaften von K- und Co-substituierten $BaFe_2As_2$-Supraleitern in magnetischen Feldern*, Ph.D. thesis (2013), Karlsruher Institut für Technologie (KIT).

[39] N. R. Werthamer, E. Helfand, and P. C. Hohenberg, "Temperature and purity dependence of the superconducting critical field, $H_{c2}$. III. electron spin and spin-orbit effects," Phys. Rev. **147**, 295 (1966).

[40] T. Maniv, V. Zhuravlev, I. Vagner, and P. Wyder, "Vortex states and quantum magnetic oscillations in conventional type-II superconductors," Rev. Mod. Phys. **73**, 867 (2001).

[41] E. Helfand and N. R. Werthamer, "Temperature and purity dependence of the superconducting critical field, $H_{c2}$. II," Phys. Rev. **147**, 288 (1966).

[42] P. Coleman, *Introduction to Many Body Physics* (to be published, Cambridge University Press, 2014).

[43] Z. P. Yin, K. Haule, and G. Kotliar, "Kinetic frustration and the nature of the magnetic and paramagnetic states in iron pnictides and iron chalcogenides," Nature Phys. **10**, 932 (2011).

[44] L. de' Medici, G. Giovannetti, and M. Capone, "Selective mott physics as a key to iron superconductors," Phys. Rev. Lett. **112**, 177001 (2014).

[45] P. Walmsley, C. Putzke, L. Malone, I. Guillamón, D. Vignolles, C. Proust, S. Badoux, A. I. Coldea, M. D. Watson, S. Kasahara, Y. Mizukami, T. Shibauchi, Y. Matsuda, and A. Carrington, "Quasiparticle mass enhancement close to the quantum critical point in $BaFe_2(As_{1-x}P_x)_2$," Phys. Rev. Lett. **110**, 257002 (2013).

[46] J. G. Storey, J. W. Loram, J. R. Cooper, Z. Bukowski, and J. Karpinski, "Electronic specific heat of $Ba_{1-x}K_xFe_2As_2$ from 2 to 380 K," Phys. Rev. B **88**, 144502 (2013).

[47] E. Morosan, D. Natelson, A. H. Nevidomskyy, and Q. Si, "Strongly correlated materials," Adv. Mater. **24**, 4896 (2012).

[48] M. Nakajima, S. Ishida, T. Tanaka, K. Kihou, Y. Tomioka, T. Saito, C. H. Lee, H. Fukazawa, Y. Kohori, T. Kakeshita, A. Iyo, T. Ito, H. Eisaki, and S. Uchida, "Normal-state charge dynamics in doped $BaFe_2As_2$: Roles of doping and necessary ingredients for superconductivity," (2013), arXiv:1308.6133 .

[49] M. M. Qazilbash, J. J. Hamlin, R. E. Baumbach, L. Zhang, D. J. Singh, M. B. Maple, and D. N. Basov, "Electronic correlations in the iron pnictides," Nat. Phys. **5**, 647 (2009).

[50] M. Nakajima, S. Ishida, T. Tanaka, K. Kihou, Y. Tomioka, T. Saito, C. H. Lee, H. Fukazawa, Y. Kohori, T. Kakeshita, A. Iyo, T. Ito, H. Eisaki, and S. Uchida, "Strong electronic correlations in iron pnictides: Comparison of the optical spectra for $BaFe_2As_2$-related compounds," (2013), arXiv:1308.6113 .

[51] A. I. Coldea, "Quantum oscillations probe the normal electronic states of novel superconductors," Phil. Trans. R. Soc. A **368**, 3503 (2010).

[52] A. Carrington, "Quantum oscillation studies of the Fermi surface of iron-pnictide superconductors," Rep. Prog. Phys. **74**, 124507 (2011).

[53] D. Shoenberg, *Magnetic oscillations in metals* (Cambridge University Press, 1984).

[54] A. McCollam, R. Daou, S. Julian, C. Bergemann, J. Flouquet, and D. Aoki, "Spin-dependent masses and field-induced quantum critical points," Physica B **359–361**, 1 (2005).

[55] B. Chandrasekhar, "A note on the possibility of observing De Haas-Van Alphen oscillations in magnetostriction," Phys. Lett. **6**, 27 (1963).

[56] B. A. Green and B. S. Chandrasekhar, "Observation of oscillatory magnetostriction in bismuth at 4.2°K," Phys. Rev. Lett. **11**, 331 (1963).

[57] P. R. Aron, "Oscillatory magnetostriction in the noble metals," J. Low. Temp. Phys. **9**, 67 (1972).

[58] R. Griessen and R. Sorbello, "Oscillatory magnetostriction and the stress dependence of the Fermi surface of aluminum, indium, zinc, and magnesium," J. Low. Temp. Phys. **16**, 237 (1974).

[59] S. V. Borisenko, V. B. Zabolotnyy, D. V. Evtushinsky, T. K. Kim, I. V. Morozov, A. N. Yaresko, A. A. Kordyuk, G. Behr, A. Vasiliev, R. Follath, and B. Büchner, "Superconductivity without nesting in LiFeAs," Phys. Rev. Lett. **105**, 067002 (2010).

[60] D. Lu, M. Yi, S.-K. Mo, J. Analytis, J.-H. Chu, A. Erickson, D. Singh, Z. Hussain, T. Geballe, I. Fisher, and Z.-X. Shen, "ARPES studies of the electronic structure of LaOFe(P,As)," Physica C **469**, 452 (2009), superconductivity in Iron-Pnictides.

[61] T. Kondo, R. M. Fernandes, R. Khasanov, C. Liu, A. D. Palczewski, N. Ni, M. Shi, A. Bostwick, E. Rotenberg, J. Schmalian, S. L. Bud'ko, P. C. Canfield, and A. Kaminski, "Unexpected Fermi-surface nesting in the pnictide parent compounds $BaFe_2As_2$ and $CaFe_2As_2$ revealed by angle-resolved photoemission spectroscopy," Phys. Rev. B **81**, 060507 (2010).

[62] D. Hsieh, Y. Xia, L. Wray, D. Qian, K. Gomes, A. Yazdani, G. F. Chen, J. L. Luo, N. L. Wang, and M. Z. Hasan, "Experimental determination of the microscopic origin of magnetism in parent iron pnictides," (2008), arXiv:0812.2289 .

[63] M. Yi, D. Lu, J.-H. Chu, J. G. Analytis, A. P. Sorini, A. F. Kemper, B. Moritz, S.-K. Mo, R. G. Moore, M. Hashimoto, W.-S. Lee, Z. Hussain, T. P. Devereaux, I. R. Fisher, and Z.-X. Shen, "Symmetry-breaking orbital anisotropy observed for detwinned $Ba(Fe_{1-x}Co_x)_2As_2$ above the spin density wave transition," Proc. Natl. Acad. Sci. USA **108**, 6878 (2011).

[64] K. Nakayama, T. Sato, P. Richard, Y.-M. Xu, T. Kawahara, K. Umezawa, T. Qian, M. Neupane, G. F. Chen, H. Ding, and T. Takahashi, "Universality of superconducting gaps in overdoped $Ba_{0.3}K_{0.7}Fe_2As_2$ observed by angle-resolved photoemission spectroscopy," Phys. Rev. B **83**, 020501 (2011).

[65] V. B. Zabolotnyy, D. S. Inosov, D. V. Evtushinsky, A. Koitzsch, A. A. Kordyuk, G. L. Sun, J. T. Park, D. Haug, V. Hinkov, A. V. Boris, C. T. Lin, M. Knupfer, A. N. Yaresko, B. Buchner, A. Varykhalov, R. Follath, and S. V. Borisenko, "$(\pi, \pi)$ electronic order in iron arsenide superconductors," Nature **457**, 569 (2009).

[66] D. V. Evtushinsky, A. A. Kordyuk, V. B. Zabolotnyy, D. S. Inosov, T. K. Kim, B. Büchner, H. Luo, Z. Wang, H.-H. Wen, G. Sun, C. Lin, and S. V. Borisenko, "Propeller-like low temperature Fermi surface of $Ba_{1-x}K_xFe_2As_2$ from magnetotransport and photoemission measurements," J. Phys. Soc. Jpn. **80**, 023710 (2011).

[67] W. Malaeb, T. Shimojima, Y. Ishida, K. Okazaki, Y. Ota, K. Ohgushi, K. Kihou, T. Saito, C. H. Lee, S. Ishida, M. Nakajima, S. Uchida, H. Fukazawa, Y. Kohori, A. Iyo, H. Eisaki, C.-T. Chen, S. Watanabe, H. Ikeda, and S. Shin, "Abrupt change in the energy gap of superconducting $Ba_{1-x}K_xFe_2As_2$ single crystals with hole doping," Phys. Rev. B **86**, 165117 (2012).

[68] N. Xu, P. Richard, X. Shi, A. van Roekeghem, T. Qian, E. Razzoli, E. Rienks, G.-F. Chen, E. Ieki, K. Nakayama, T. Sato, T. Takahashi, M. Shi, and H. Ding, "Possible nodal superconducting gap and Lifshitz transition in heavily hole-doped $Ba_{0.1}K_{0.9}Fe_2As_2$," Phys. Rev. B **88**, 220508 (2013).

[69] H. Hodovanets, Y. Liu, E. D. Mun, T. A. Lograsso, S. L. Bud'ko, and P. C. Canfield, "Fermi surface reconstruction in $(Ba_{1-x}K_x)Fe_2As_2$ ($0.44 \leq x \leq 1$) probed by thermoelectric power measurements," (2014), arXiv:1405.4306 .

[70] H. Ikeda, private communication (2014).

[71] M. I. Aroyo, D. Orobengoa, G. de la Flor, E. S. Tasci, J. M. Perez-Mato, and H. Wondratschek, "Brillouin-zone database on the *Bilbao Crystallographic Server*," Acta Crystallogr. Sect. A **70**, 126 (2014).

[72] T. Terashima, M. Kimata, N. Kurita, H. Satsukawa, A. Harada, K. Hazama, M. Imai, A. Sato, K. Kihou, C.-H. Lee, H. Kito, H. Eisaki, A. Iyo, T. Saito, H. Fukazawa, Y. Kohori, H. Harima, and S. Uji, "Fermi surface and mass enhancement in $KFe_2As_2$ from de Haas–van Alphen effect measurements," J. Phys. Soc. Jpn. **79**, 053702 (2010).

[73] S. Backes, D. Guterding, H. O. Jeschke, and R. Valenti, "Electronic structure and de Haas-van Alphen frequencies in $KFe_2As_2$ within LDA+DMFT," (2014), arXiv:1403.6993 .

[74] T. Terashima, N. Kurita, M. Kimata, M. Tomita, S. Tsuchiya, H. Satsukawa, A. Harada, K. Hazama, M. Imai, A. Sato, S. Uji, K. Kihou, C.-H. Lee, H. Kito, Y. Tomioka, T. Ito, A. Iyo, H. Eisaki, T. Liang, M. Nakajima, S. Ishida, S. ichi Uchida, T. Saito, H. Fukazawa, Y. Kohori, and H. Harima, "Quantum oscillations in iron-based superconductors: $BaFe_2As_2$ vs. $KFe_2As_2$," JPCS **449**, 012022 (2013).

[75] K. Hashimoto, A. Serafin, S. Tonegawa, R. Katsumata, R. Okazaki, T. Saito, H. Fukazawa, Y. Kohori, K. Kihou, C. H. Lee, A. Iyo, H. Eisaki, H. Ikeda, Y. Matsuda, A. Carrington, and T. Shibauchi, "Evidence for superconducting gap nodes in the zone-centered hole bands of $KFe_2As_2$ from magnetic penetration-depth measurements," Phys. Rev. B **82**, 014526 (2010).

[76] A. Georges, L. d. Medici, and J. Mravlje, "Strong correlations from Hund's coupling," Annu. Rev. Condens. Matter Phys. **4**, 137 (2013).

[77] J. Wu, P. Phillips, and A. H. Castro Neto, "Theory of the magnetic moment in iron pnictides," Phys. Rev. Lett. **101**, 126401 (2008).

[78] Z. Zhang, A. F. Wang, X. C. Hong, J. Zhang, B. Y. Pan, J. Pan, Y. Xu, X. G. Luo, X. H. Chen, and S. Y. Li, "Heat transport in $RbFe_2As_2$ single crystal: evidence for nodal superconducting gap," (2014), arXiv:1403.0191 .

[79] A. F. Wang, B. Y. Pan, X. G. Luo, F. Chen, Y. J. Yan, J. J. Ying, G. J. Ye, P. Cheng, X. C. Hong, S. Y. Li, and X. H. Chen, "Calorimetric study of single-crystal $CsFe_2As_2$," Phys. Rev. B **87**, 214509 (2013).

[80] S. L. Bud'ko, D. Y. Chung, D. Bugaris, H. Claus, M. G. Kanatzidis, and P. C. Canfield, "Heat capacity jump at $T_c$ and pressure derivatives of superconducting transition temperature in the $Ba_{1-x}Na_xFe_2As_2$ ($0.1 \leq x \leq 0.9$) series," Phys. Rev. B **89**, 014510 (2014).

[81] S. L. Bud'ko, M. Sturza, D. Y. Chung, M. G. Kanatzidis, and P. C. Canfield, "Heat capacity jump at $T_c$ and pressure derivatives of superconducting transition temperature in the $Ba_{1-x}K_xFe_2As_2$ ($0.2 \leq x \leq 1.0$) series," Phys. Rev. B **87**, 100509 (2013).

[82] V. Grinenko, D. V. Efremov, S.-L. Drechsler, S. Aswartham, D. Gruner, M. Roslova, I. Morozov, K. Nenkov, S. Wurmehl, A. U. B. Wolter, B. Holzapfel, and B. Büchner, "Superconducting specific-heat jump $\Delta C_{\rm el} \propto T_c^{\beta}(\beta \approx 2)$ for $K_{1-x}Na_xFe_2As_2$," Phys. Rev. B **89**, 060504 (2014).

[83] J. Geerk, R. Schneider, G. Linker, A. G. Zaitsev, R. Heid, K.-P. Bohnen, and H. v. Löhneysen, "Observation of interband pairing interaction in a two-band superconductor: $MgB_2$," Phys. Rev. Lett. **94**, 227005 (2005).

[84] F. F. Tafti, A. Juneau-Fecteau, M.-E. Delage, S. R. de Cotret, J.-P. Reid, A. F. Wang, X.-G. Luo, X. H. Chen, N. Doiron-Leyraud, and L. Taillefer, "Sudden reversal in the pressure dependence of T-c in the iron-based superconductor $KFe_2As_2$," Nature Phys. **9**, 349 (2013).

[85] Z. Shermadini, H. Luetkens, A. Maisuradze, R. Khasanov, Z. Bukowski, H.-H. Klauss, and A. Amato, "Superfluid density and superconducting gaps of $RbFe_2As_2$ as a function of hydrostatic pressure," Phys. Rev. B **86**, 174516 (2012).

[86] F. F. Tafti, J. P. Clancy, M. Lapointe-Major, C. Collignon, S. Faucher, J. A. Sears, A. Juneau-Fecteau, N. Doiron-Leyraud, A. F. Wang, X.-G. Luo, X. H. Chen, S. Desgreniers, Y.-J. Kim, and L. Taillefer, "Sudden reversal in the pressure dependence of $T_c$ in the iron-based superconductor $CsFe_2As_2$: A possible link between inelastic scattering and pairing symmetry," Phys. Rev. B **89**, 134502 (2014).

# Acknowledgments

I would like to thank everyone who contributed to this work.

First, I thank Hilbert von Löhneysen for giving me the opportunity to work at the Institut für Festkörperphysik (IFP), for advising my doctoral research, and for his support. I thank Jörg Schmalian for giving his opinion on this work and for discussions about iron-based superconductors.

Special thanks goes to Kai Grube for advising my doctoral research day-to-day, for providing training and assistance with all things technical and scientific, and for maintaining a superb technical and social environment to work in.

I thank Thomas Wolf, Doris Ernst, and Peter Adelmann for growing and providing single crystals on demand. I thank Peter Schweiss and also Michael Merz for sharing four-circle x-ray refinement data. I thank Rolf Heid and Hiroaki Ikeda (formerly Kyoto University, now Ritsumeikan University) for calculations of and discussions about the band structure of $KFe_2As_2$, $RbFe_2As_2$, and $CsFe_2As_2$. Special thanks goes to Hiroaki Ikeda for plots of the Fermi surfaces and for calculations of the band-resolved density of states.

I thank Diego Zocco for training in the operation of a dilution refrigerator and for discussions. I thank Roland Schäfer for technical advice on the operation of a dilution refrigerator and for support with the automation of experiment control.

I thank Stephen Julian (University of Toronto), Graeme Luke (McMaster University), Robert Hill (University of Waterloo), Steffen Backes and Daniel Guterding (Frankfurt), Luca de'Medici (ESRF, Grenoble), Frederic Hardy, Anna Böhmer, and Christoph Meingast for discussions.

I thank the workshops for their excellent service.

I thank all members of the IFP, including my fellow doctoral researchers Sebastian Zaum, Philipp Burger, Sven Krannich, Anna Böhmer, Alexander Herbig, Michael Maschek, Andreas Kapuvari for the nice work environment.

Finally and foremost, I thank my wife for her support.